Porphyrin on Metal Surfaces: A Density Functional study

Author: Paolo Poli

Supervisor: Prof. Mats Persson

Surface Science Research Centre
Department of Chemistry

Thesis submitted in accordance with the requirements of the University of Liverpool for the degree of Doctor in Philosophy

June 2018

Contents

List of Tables

Abstract

In this thesis various aspects of porphyrin adsorption on metal surfaces were studied using Density Functional Theory (DFT) calculations. The studies were motivated by recent experiments and include self-assembly of adsorbed porphyrins, CO bonding to the metal centres of the porphyrins and the associated anharmonicity of the internal stretch mode and on-surface porphine dimerisation. This reaction is a precursor for the oligomerisation of Porphines into various nano structures such as nano wires and tapes with a potential interest for the development of nanotechnologies and molecular devices.

Chapter 1 gives a brief introduction to porphyrin and surface science. The experimental methods such as reflection absorption infrared spectroscopy, Sum Frequency Generation (SFG) and Scanning Tunnelling Microscopy (STM), which are central to the thesis, are discussed shortly in Chapter 2. Chapter 3 gives a brief background of the theory behind the DFT calculations with results presented in Chapters 4 - 6. Finally, concluding remarks and a future outlook are presented in Chapter 7.

Chapter 4 presents results for the adsorption energies and structures of isolated and adsorbed Tetra Phenyl Porphyrin (TPP) with three different metal centres, Ru, Co and Zn, on a Cu(110) surface. These results include also a study of the bonding of CO to these isolated and adsorbed complexes. Their electronic structures are analysed using calculated projected and partial density of states. The calculated STM images compared favourably with the observed images. The adsorption on the Cu(110) surface is found to have a significant effect on their geometric structures but also on the CO bonding.

The analysis of the CO bonding to the porphyrins continues in Chapter 5 with a study of the anharmonicity of the internal stretch mode based of DFT calculations of potential energy curves for the internal stretch of CO in various bonding situations. This study was motivated by the relatively large value of this anharmonicity observed by SFG for CO bonded to Ru-TPP adsorbed on a Cu(110) surface. Furthermore, some attention was paid concerning the possibility to use the anharmonicity to estimate important quantities such as the dissociation energy.

Chapter 6 presents the results of reaction thermodynamics calculations of dimer formation of physisorbed porphine monomers on the Au(111) surface through C-C coupling. This study is motivated by recent observations by STM of this reaction under ultra high vacuum conditions carried out at University of Liverpool and University of Graz. In particular, a puzzling observation is the different occurrences of various bonding motifs at different surface temperatures. These calculations include also free energy contributions from translational and rotational motions of the reac-

tants and products. The large entropy of the hydrogen gas under ultra high vacuum conditions is found to be a strong thermodynamic driving force for the dimerisation reaction. The calculated STM images helped the assignment of the observed STM images to different bonding motifs. The reaction free energy calculations were able to rationalise the different occurrences of the most observed dimer bonding motifs.

Acknowledgement

First of all I want to thank my supervisor Prof. **Mats Persson** for giving me the opportunity of doing this PhD, and his patience in answering all my questions concerning my projects, and his help to make my research more interesting by giving me some important clues.

I am very grateful to Dr. **Heike Arnolds** and Dr. **Takuma Omiya** for the important internal collaboration that arose in my first part of my PhD and their important suggestions about how to focus my calculations in the best way possible. I am also very grateful to Dr.**Wit Bareld**, Dr.**Fiona McBride** and Prof. **Rasmita Raval** for the important internal collaboration in the second part of my PhD. Finally, I want to thank Prof.**Yousoo Kim** in Riken and Prof. **Leonhard Grill** in University of Graz, for the external experimental collaboration.

Many thanks to all the people in Surface Science Research Centre. Specifically, I would like to thank **Alina** for the chats during my PhD and for sharing a lot of chocolate with me. **Emile** for the long discussions about physics and chemistry during lunch time and the funny moments. Finally, **Ioritz**, **Jose**, **Luca**, **Stefano**, for making my demonstrating less hard and more comfortable, Thanks to **Tiago** for his cooking suggestions and **Marcel** for the chess matches during the coffee break.

Furthermore, thanks to **Ivan**, **Jyoti**, **Tommaso** for introducing me to the University and the Department at the first days of my PhD studies.

Finally I want to thank my landlord **Keith** that gave me the possibility to live in a comfortable place and showed me some beautiful places in Liverpool with explanations of historical details, and especially for the chats about football.

Publications

Desorption of CO from individual ruthenium porphyrin molecules on a copper surface via an inelastic tunnelling process Takuma Omiya, Paolo Poli, Heike Arnolds, Rasmita Raval, Mats Persson and Yousoo Kim. *Chemical Communications* **53**, 6148-6151 (2017)

Abbrevations

ASE	Atomic Simulation Environment
BZ	Brillouin Zone
DFT	Density functional theory
DOS	Density of States
GGA	Generalised Gradient Approximation
HOMO	Highest Occupied Molecular Orbital
LEED	Low Energy Electron Diffraction
LUMO	Lowest Unoccupied Molecular Orbital
MTPP	Metal Tetra Phenyl Porphyrin
P	Porphine
P2	Porphine Dimer.
PAW	Projected Augmented Wave
PBE	Perdew-Burke-Enzerhof
PDOS	Projected Density of States
PEC	Potential Energy Curve
PES	Potential Energy Surface
RAIRS	Reflection Absorption Infrared Spectroscopy
SFG	Sum Frequency Generation
STM	Scanning Tunnelling Microscopy
STS	Scanning Tunnelling Spectroscopy
UHV	Ultra High Vacuum

Chapter 1

Introduction

This chapter presents a brief introduction to the central topics of the thesis such as the field of surface science, porphyrin molecules and density functional theory (DFT) calculations.

1.1 Surface Science: A Brief Introduction

It is difficult to give a precise date of the birth of surface science, but the discovery of the platinum-surface-catalysed reaction of water from hydrogen and oxygen molecules by Dobereiner [1] already in 1823 was one of the first landmarks of Surface Science. However, the first technologically important surface reactions appeared in the period of 1860-1912, with processes such as the Deacon, Mond, Ostwald processes [1].

For a deeper understanding of surface reactions and processes, the scientist waited until 1964, when the ultra-high vacuum (UHV) technology became available to carry out experiments under well-defined conditions. Under these conditions, it was possible to characterise surfaces and investigate surfaces phenomena using experiments based on electron, photon, atom and ion beam scattering. A most important development was the invention of the scanning tunnelling microscopy (STM) by Binnig and Rohrer [2]. The STM made possible to investigate single adsorbed atoms and molecules [3] instead of ensembles and also paved the way for the emergence of nano science and technology. An example of successful application of STM was the first determination of the geometrical structure of the Si(7x7) surface in 1983 [4], whereas earlier experimental techniques failed with this structure determination.

Some other important surface experimental techniques include ultraviolet photo electron spectroscopy and x-ray core-hole spectroscopy where the photoelectric effect is used for an understanding of the energy bonding between two atoms or molecules,

Auger electron spectroscopy (AES) [5], [6] and sum frequency generation (SFG) based on pulsed laser beams in the visible and the infrared where the non-linear response of the material generate another beam at a frequency equal to the sum of the frequencies of the infrared beam and the visible beam [7]. So there is a multitude of experimental techniques in Surface Science that can be used to characterise and investigate processes and phenomena at surfaces. Some examples of phenomena are given below.

One important phenomenon is *thermionic emission* [8], [9]. where electrons are emitted from a heated surface. *Crystal growth* [10], [11] is very important and proceeds through the diffusion of atoms or molecules on surfaces and their interactions. *Heterogeneous catalysis* [12], [13], [14] is probably the most studied topic in surface science due to its paramount importance for the society. The mechanisms behind the catalytic activity of surfaces are investigated by many different experimental techniques. The final are to be brought up here is *semiconductor interfaces* [15], [16], [17]. Many semiconducting devices depend crucially upon phenomena that occur at a surface or interface, such as junction between p-type and n-type semi-conductor, a junction between a metal oxide and a semiconductor and the Schottky barrier between a metal in contact with a semiconductor. This short list of areas shows that Surface Science is not just important for fundamental studies but also for the development of new technologies.

1.2 Porphyrins: A Brief Introduction

Before discussing the importance of porphyrin molecules, we begin by a short discussion of the structures of the two examples of porphyrin molecules – porphine and the tetraphenyl porphyrin – studied in the thesis. These structures are shown in Figs. 1.1 and 1.2. The porphine is the simplest example of a porphyrin molecule with the generic structure consisting of a macrocycle of four pyrrole groups, whereas the TPP has four tetra phenyl groups attached to the macrocycle. The two inner H atoms can also readily be replaced by a metal atom by bonding to the N atoms of the pyrrole groups. The ability of the porphyrin molecules to have such metal centres and to be functionalised by side groups makes this class of molecules [18], [19] to be among the most interesting organic molecules in nature.

The importance of porphyrin molecules and their physical and chemical proprieties was first realised through the studies in the field of medicine [20], through the study carried out by scientist such as Küster and Fischer, and the discovered of the importance of porphyrin to transport important molecules such as CO_2 and O_2 in the body [21], [22], [23].

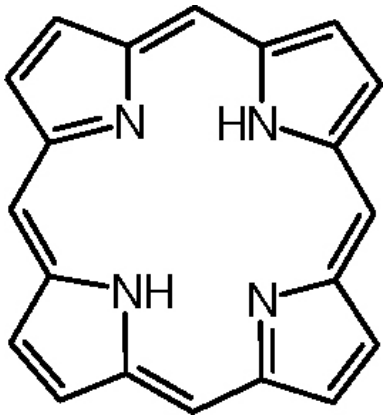

Figure 1.1: Structure of base porphine, the simplest porphyrin.

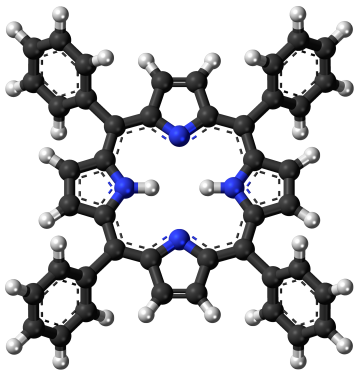

Figure 1.2: Structure of tetraphenyl porphyrin.

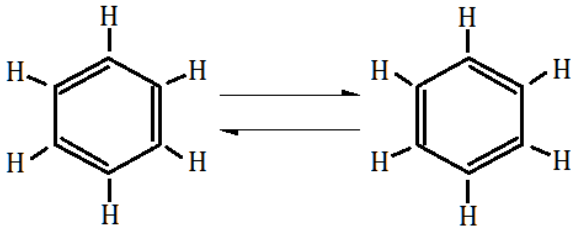

Figure 1.3: Resonance effect between the two possible arrangements of alternating single and double C-C bonds of benzene.

Another example is the important role played by porphyrin in photosynthesis [24] . The discovery that porphyrin was present in chlorophyll took a long time. Chlorophyll was already identified and named by Pelletier and Caventou [20] in 1818. The atomic structure of chlorophyll was not elucidated until 150 years later by Fischer, Orth and Woodward [20] in 1960. They showed that chlorophyll are defined by the presence of a porphyrin molecule consisting of four pyrrole rings linked to a magnesium atom at its centre.

After 150 years of research on porphyrins and their physical, chemical and biological properties one is now also interested using this molecule in nano science and nano technologies for the development of molecular devices.

1.2.1 Aromatic bonding

Aromatic molecules are planar and cyclic organic molecules which has a strong stability with respect to other molecular configurations. Porphine turns out to be an aromatic molecule as will be shown below.

There are two conditions for a molecule to be aromatic. The first condition is that molecule has to be cyclic and flat with the relevant C valence orbitals forming sp^2 hybrids and π orbitals. These hybridised orbitals form σ and π bonds,respectively. The second condition is the Huckel rule that the number of π electron pairs has to be odd. In a molecular orbital description of the π bonding, this condition for the electron count corresponds to a closed shell structure and thus an enhanced stability. This closed shell structure and the delocalisation of the π electrons results also in all C-C bond lengths being equal. The most well-known aromatic molecule is the benzene molecule which has a six membered ring of C atoms with six π electrons and equal C-C bond lengths of 1.40 Å. In a valence bond picture, the aromaticity of the benzene molecule is viewed as a resonance between the two possible arrangements of

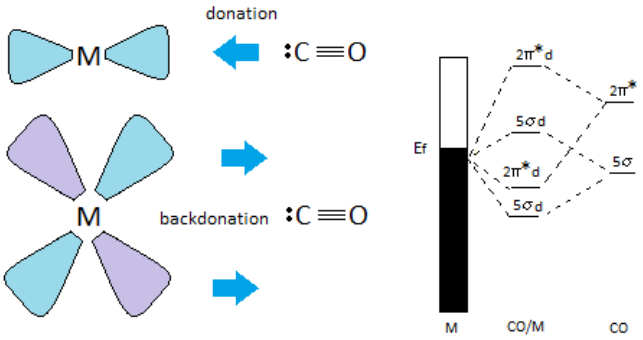

Figure 1.4: Blyholder model of CO metal bonding and orbital mixing.

alternating single and double C-C bonds as illustrated in Fig. 1.3

As shown in Fig. 1.1, porphine is a planar molecule with 20 C atoms in a cycle. There will also be electrons contributing to the π manifold from the N atoms. Each N atoms has two σ bonds with C atoms but each imine N atom has a lone pair and contributes with one electron whereas each amine N atom has a single bond with an H atom and contribute with two electrons. So in total there are 26 electrons in the π manifold of orbitals, which corresponds to an odd number of electron pairs. Thus, the porphine molecule satisfies the two conditions for an aromatic molecule.

1.3 Blyholder model of CO-metal bonding

Chapters 4 and 5 present computational studies of the bonding of CO on metallated tetraphenyl-porphyrin (MTPP) molecules for various metal centres and includes also a study of their adsorption energy, and the internal CO stretch frequency. A classic and successful model for describing CO bonding in various metal carbonyls and for adsorption on metal surfaces is the Blyholder model [25, 26].

The CO molecule is bonded by a single σ bond and a double π bond. The σ bond arises from the occupation of the 5σ orbital which is formed by a bonding combination of the sp_z hybrid orbital of the C atom and the p_z orbital of the O atom. The π bonds arise from the occupied, two-fold degenerate, 1π orbitals which are formed by the bonding combinations of the p_x and p_y orbitals of the C and O atoms. Due to the higher electronegativity of the O atom than the C atom, the highest occupied orbital is the 5σ orbital with dominant weight on the C atom. The lowest unoccupied orbitals are the two-fold, degenerate $2\pi^\star$ orbitals which are formed by the anti-bonding combination of p_x and p_y orbitals of the C and O atoms.

A dative bond between a CO molecule and a metal can now be formed by the

mixing of 5σ orbital with unoccupied metal orbitals resulting in an electron donation into these metal states. This donation is compensated by an electron back-donation to the $2\pi^\star$ orbitals obtained by a mixing of these orbitals with occupied metal states. This picture is illustrated in 1.4. The back donation into CO $2\pi*$ anti-bonding orbital weakens the CO bond resulting in an elongation of the bond. In the case of the bonding with a transition metal atom as in the case of MTPP, the 5σ orbital mixes with d_z orbitals, whereas $2\pi^\star$ mixes with $d_{xz/yz}$ orbitals.

1.4 Crystal field theory and d orbitals splitting

Crystal field theory is used for the elucidation of bonding in transition metal (TM) ion complexes. This theory only takes into account the electrostatic interaction between the ligands and the TM ion. The ligands are represented by point charges and the corresponding electrostatic (crystal) field interacts with the orbital charge densities of the five d orbitals. This crystal field will then result in a energy splitting of the degenerate d orbitals of the TM ion. The nature of this splitting and the resulting energy ordering depends on the different spatial orientations of the d orbitals and the symmetry of the coordination of the ligands as illustrated below.

1.4.1 An octahedral complex

In the octhaedral coordination of the TM ion with six ligands 1.5, the crystal field splits the five-fold degenerate d level into a two-fold degenerate level and a three-fold degenerate level with symmetry characters e_g and t_{2g}, respectively. The electrostatic interaction increases the average value of the energies of the d orbitals with respect to their energy of the isolated transition metal ion. The lobes of the d_{z^2} and $d_{x^2-y^2}$ orbitals of the e_g level has a stronger electrostatic interaction with the point charges than the lobes of the d_{xy}, d_{xz} and d_{yz} orbitals of the t_{2g} level so that the e_g level is higher in energy than the t_{2g} level.

1.4.2 A tetrahedral complex

In the tetrahedral coordination of the TM ion with four ligands, the crystal field splits the five-fold degenerate d level in the same manner as for the octahedral coordination into a two-fold degenerate e_g level and a three-fold degenerate t_{2g} level as shown in Fig. 1.5. However, the energy ordering of these two levels are reversed for a tetrahedral complex as compared to an octahedral complex due to the lobes of the t_{2g} orbitals in this case are closer to the point charges of the ligands than the lobes of the e_g orbitals.

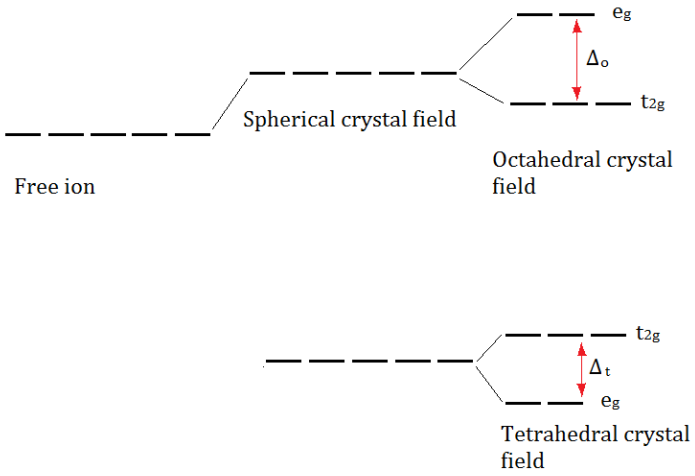

Figure 1.5: Energy levels of an octahedral and a tetrahedral transition metal ion complex.

1.4.3 A square planar complex

The square planar coordination of the TM ion is the most relevant here in the case of MTTP. The crystal field splits the five-fold degenerate d energy level into a single two-fold degenerate energy level of the d_{xz} and d_{yz} orbitals and three non-degenerate energy levels of the remaining d orbitals. The d_{xz} and d_{yz} orbitals has the weakest interaction with the ligands due to their nodal plane is in the molecular plane and has the lowest energy level, whereas the remaining d orbitals have no nodes at the molecular plan and will have higher energies in the order shown in Fig.1.6.

1.5 DFT calculations

Density Functional Theory (DFT) is used in this thesis to investigate the geometric and electronic structure of adsorbed porphyrin molecules. The advantage of DFT is that the electron density is the basic variable instead of the many-electron wave function. This makes it possible to develop efficient and approximate computational methods for solving the many-electron problem for large systems with useful accuracy.

Despite the first idea about using the electron density as basic variable in determining the electronic structure appeared already in the 1930s with the Thomas-Fermi model [27], we had to wait until the 1960s before this idea was set on a firm footing and was viable by the development of density functional theory (DFT) by Kohn and Hohenberg [28]. Together with Sham, Kohn also developed the local density approximation which was widely used in solid state physics. However, it took another 30

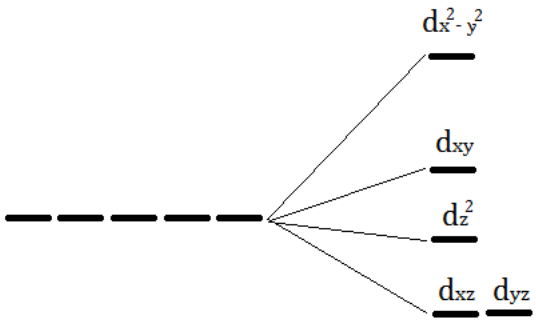

Figure 1.6: Energy levels of a planar square transition metal ion complex.

years before DFT attracted interest from the chemistry community through the development of the generalized gradient approximation. Two of the examples where DFT calculations have given important results are the following:

Ammonia synthesis by Heterogeneous Catalysis is a very important process for nitrogen fixation. In spite of this reaction is very simple as given by

$$N_2 + 3H_2 \rightarrow 2NH_3 \,, \tag{1.1}$$

high temperature (400 °C) and high pressure (100 atm) are necessary to run the reaction in presence of metals such as iron (Fe) and ruthenium (Ru) that act as catalysts. Despite this reaction being discovered almost 100 years ago by Haber, the reaction mechanisms are just beginning to be unraveled.

An example of how DFT calculations can contribute to a solution of this problem was given by Honkala and coworkers [29]. They showed that the net chemical reaction, Eq. (1.1) proceeds via at least 12 distinct steps on a Ruthenium catalyst and that the rates of these steps depend strongly on the local coordination of the metal atoms to the reactants. The challenge was to predict the relative stability of many different local coordination of surface atoms on a Ru nanoparticle in a way that allowed them to predict the detailed shape of the nanoparticles as a function of particle size. This prediction gave an idea about the relation between the diameter of the nano particle considered and the number of highly desirable reactive sites for breaking the N_2 bond on the nanoparticle. From the results of these studies, they were able to develop a kinetic model that describes how the individual reaction rates for many different kinds of metal atoms on the nanoparticle's surfaces couple together to define the overall reaction rate under realistic reaction conditions. Applying this kinetic model at the experiments running under the industrial conditions, Honkala and co-worker obtained a

stunning agreement with the experimental results, avoiding using any values derived from experimental data.

Embrittlement of Metals by Trace Impurities is an example where tiny amounts of an element can change the physical and chemical properties of the host. If an important metal such as copper is mixed with a tiny quantity of another element it loses some of its important properties such as its ductility. This phenomena is really surprising, in view of that these effects are observed if the used trace element is not soluble in copper such as bismuth. The DFT calculations of bulk mixing of copper and bismuth by Schweinfest, Paxton and Finnis [30] showed that the formation energy of a grain boundary decreased in the presence of bismuth. Furthermore, the associated embrittlement was not a grain boundary electronic effect but was causes by the atomic size of the bismuth atom.

1.6 Research objectives

The main objectives and topics of this thesis are listed below.

1.6.1 Self assembly of porphyrins on metal surfaces

The self-assembly of porphyrin molecules on metal surfaces [31], [32], [33], [34], is an emerging area of research. This assembly is an interesting process since it can help us to change the porphyrin geometry and its function by the interaction of the molecules with the surface and the surrounding molecules. In Chapter 4, we study using DFT calculations the geometric structure and electronic structure of isolated TPP molecules with the three different metal centres Ru, Co and Zn and adsorbed on a copper surface. One aim of this study is to investigate how the rotation and tilting of the phenyl groups of these TPP molecules change upon adsorption and self-assembly on this metal surface. The ability to control the orientation of the phenyl rings could be of potential interest in the development of nanotechnology such as memory storage, nano transistors and molecular machines. [35], [36], [37], [38].

1.6.2 Interaction of inorganic molecules with porphyrins

The interaction of inorganic molecules with porphyrins is a key process in some life processes in nature such as oxygen transport in humans. This process is enabled by the coordination of an O_2 molecule to the metal centre of a porphyrin molecule. Furthermore, the stronger bond formed by the CO molecule to this metal centre is the underlying cause for CO poisoning. In Chapters 4 and 5, we study using DFT calculations the interaction of CO with an isolated and adsorbed TPP molecule for the

three different metal centres Ru, Co and Zn [39], [21], [40]. This study includes the calculation of geometric structures, CO adsorption energies, electronic structure and the potential energy curve for the internal CO stretch. This study is motivated by recent vibrational spectroscopy of the CO molecule adsorbed on these porphyrin molecules and the aim is to find out whether the observed anomalous value for the anharmonicity of the internal CO stretch is due to an unusual bonding.

1.6.3 On surface porphyrin oligomerisation

The formation of nano structures of adsorbed porphyrin molecules such as nano tapes and wires by oligomerisation is another area that has attracted a lot of interest [18, 32]. This kind of nano structures has the capacity to control the conductance [41], and to create junctions for semiconductors and memory storage on the nanoscale which could be useful for the development of the next generation of computers [42]. One widely used metod to form oligomers from adsorbed porphyrin monomers is based on on-surface Ullman coupling [43], [44]. The disadvantage of this coupling is the involvement of halogen atoms which pollutes the surface. In Chapter 6, we study the dimerisation of porphyrin molecules adsorbed on an inert gold surface by C-C coupling with the only waste product being hydrogen which desorbs from the surface. This dimerisation reaction is the intial step of the oligomerisation of the adsorbed porphyrin molecules. This study is motivated by recent STM experiments of this reaction and the aim is to rationalise the observed occurrences of different dimer bonding motifs at different surface temperatures from the DFT calculations of the reaction thermodynamics.

Chapter 2

Experimental methods

In this chapter, the main experimental surface techniques that are behind the projects in this thesis are discussed. Particular emphasis is given to scanning tunnelling microscopy and vibrational spectroscopy. The first section discusses mainly the theory behind imaging by the scanning tunnelling microscope and how the images can be calculated using the Tersoff-Hamann approximation. STM images of adsorbed molecules were calculated and compared with experiments in Chapters 4 and 6. The experimental results that are discussed in Chapters 4 and 5 were based primarily on vibrational spectroscopy of fundamental vibrational modes and their overtones using sum frequency generation but also using reflection absorption infrared spectroscopy. These two spectroscopies are discussed in the following two sections. This discussion includes also a description of the harmonic approximation of vibrational modes.

2.1 Scanning tunnelling microscopy

Since the invention of Scanning tunnelling microscopy [45], [46],[2],[47] (STM), physicists have a new tool to investigate and manipulate the atomic world. This invention has permitted the researchers to image adsorbed atoms and molecules on surfaces at the atomic scale. This capability is based on the quantum effect of tunnelling of electrons between the tip and the sample. To understand how tunnelling in the STM works, we will first consider an one-dimensional model of the STM junction as shown in Fig. 2.1. The vacuum region between the tip and the sample gives rise to a potential barrier between the electrons confined in the tip and the sample, respectively.

In this model, the wave function $\phi(z)$ of the electron with an energy E satisfies the time-independent Schrödinger equation,

$$-\frac{\hbar^2}{2m_e}\frac{\partial^2\phi(z)}{\partial z^2} + U(z)\phi(z) = E\phi_n(z) \tag{2.1}$$

where $U(z)$ is the potential of the electron at position z and m_e is the electron mass. In the tip and and the sample regions, where $E > U(z) = 0$, the solutions are a superposition of travelling waves, $\exp(\pm ikz)$ with the wave vector k,

$$k = \frac{\sqrt{2m_e E}}{\hbar} \tag{2.2}$$

whereas in the vacuum region, where $E < U(z) = U_0$, the solution will be a superposition of evanescent waves, $\exp(\pm\kappa z)$, where

$$\kappa = \frac{\sqrt{2m_e(U_0 - E)}}{\hbar} \ . \tag{2.3}$$

The resulting form of the wave function for an incident wave from $z < 0$ is shown in Fig. 2.1. In the case of deep tunnelling the solution in the vacuum region is dominated by the exponentially decaying solution, $\exp(-\kappa z)$, and the probability to cross the barrier, that is the tunnelling probability, is then essentially given by,

$$P = \exp(-2\kappa d) \tag{2.4}$$

where d is the barrier width. Thus there is a strong exponential dependence on the square root of barrier height, $U_0 - E$, through κ and the barrier width. For a typical barrier height of about 4.5 eV corresponding to the work function, the tunnelling probability decreases with about a factor 10 for an increase of d of 1 Å. This strong exponential dependence on the barrier width is the underlying reason behind the atomic resolution of the STM.

Finally, in order to get the tunnelling current from the tunnelling probability at a bias V, one needs to integrate over current of incident electrons that are allowed to cross the barrier by ending up in an unoccupied state times the tunnelling probability. In the next section, we outline how this can be done in the full three-dimensional case when introducing the Tersoff-Hamann approximation [48] used in this thesis for calculating STM images.

2.1.1 The Tersoff-Hamann Approximation

Tersoff and Hamann TH [48] showed that under certain assumptions the differential tunnelling conductance is simply proportional to the local density of states (LDOS) of the sample wave functions at the tip apex as,

$$\frac{dI}{dV}(V) \propto \rho(\vec{r}_t, \epsilon_F + eV) \tag{2.5}$$

where $\frac{dI}{dV}(V)$ is the differential tunnelling conductance at a sample bias V and the LDOS is defined as,

$$\rho(\vec{r}_t, \epsilon_F + eV) = \sum_s |\phi_s(\vec{r}_t)|^2 \delta(\epsilon - \epsilon_s) \ . \tag{2.6}$$

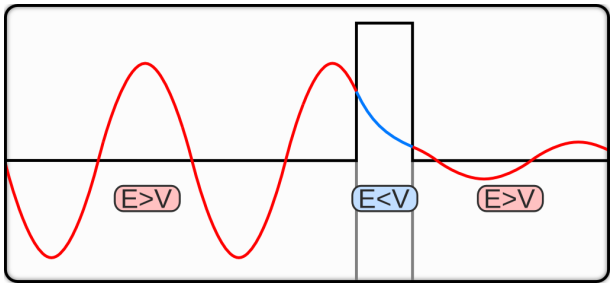

Figure 2.1: One-dimensional model of tunnelling in an STM junction. The solution of the time-independent Schrödinger through the indicated potential barrier equation is shown.

Here $\phi_s(\vec{r})$ is a sample, one-electron wave function with energy ϵ_s and $\vec{r}_t$ is the position of the tip apex. Note that his result does not give an absolute value for the differential tunnelling conductance.

The TH approximations is based on two key assumptions: Bardeen's expression [49]for the tunnelling matrix element and an s-wave approximation of the tails of the tip wave functions in the vacuum region. From the Fermi golden rule, the tunnelling rate between a tip state t and a sample state s is given by,

$$w_{st} = \frac{2\pi}{\hbar}|M_{st}|^2\delta(\epsilon_s - \epsilon_t) \tag{2.7}$$

where ϵ_s and ϵ_s are the energies of s and t, respectively. Bardeen showed that the tunnelling matrix element can be expressed as,

$$M_{st} = \frac{\hbar^2}{2m}\int_S (\phi_s(\vec{r})\nabla\phi_t(\vec{r}) - \phi_t(\vec{r})\nabla\phi_s(\vec{r}))\cdot d\vec{S}\,, \tag{2.8}$$

Here S is a dividing surface in the vacuum region between the tip and the sample and $\phi_s(\vec{r})$ is a sample wave function. Assuming that the tip wave function $\phi_t(\vec{r})$ is an s-wave function on S with a centre at the tip apex $\vec{r}_t$ and using Green's theorem for the surface integral, one obtains that Bardeen's tunnelling matrix element reduces to a simple separable form,

$$M_{st} = C_t\phi_s(\vec{r}_t) \tag{2.9}$$

where C_t is a constant determined by the tip wave function. The tunnelling current is now obtained from summing up the tunnelling rates and taking into account the Fermi statistics of the sample and tip as,

$$I = \frac{4\pi e}{\hbar}\sum_{st}[f(\epsilon_t - eV) - f(\epsilon_s)]|M_{st}|^2\delta(\epsilon_s - \epsilon_t) \tag{2.10}$$

$$= \frac{4\pi e}{\hbar}\int_\infty^\infty d\epsilon[f(\epsilon - eV) - f(\epsilon)]\sum_{st}|M_{st}|^2\delta(\epsilon - \epsilon_t)\delta(\epsilon - \epsilon_s) \tag{2.11}$$

where the sum is over sample s and tip t states, $f(\epsilon)$ is the Fermi-Dirac distribution for the sample and V is the sample bias. The differential conductance at zero temperature is now obtained by differentiating I with respect to V in Eq. (2.11) and one obtains,

$$\frac{dI}{dV}(V) = \frac{4\pi e}{\hbar}|M_{st}|^2\delta(\epsilon_F + eV - \epsilon_t)\delta(\epsilon_F + eV - \epsilon_s) \tag{2.12}$$

Thanks to the separable form of the matrix element M_{st} in Eq. (2.9), one now obtains the Tersoff-Hamann result in Eq. (2.6) from Eq. (2.9).

Finally, the calculation of the $\rho(\vec{r}_t, \epsilon)$ is challenging since it depends on the tail of the sample wave functions in the vacuum region, which contribute negligible to the total energy in the DFT calculations. This problem is alleviated by extrapolating these wave functions far way into the vacuum region where the KS potential is constant based on their analytical behaviour in this region. In the slab representation of the sample in a super cell, the KS one-electron wave function can be labelled by a lateral wave vector $\vec{K}$ in the surface Brillouin zone and is extrapolated from the matching plane $z = z_m$ into the vacuum region as (atomic units),

$$\phi_{\mu;\vec{K}}(\vec{r}) = \sum_{\vec{G}} c_{\mu;\vec{K}+\vec{G}}(z_m) \exp\left(-\sqrt{2(\Phi - \epsilon_{\mu;\vec{K}}) + (\vec{K}+\vec{G})^2}(z - z_m) + i(\vec{K}+\vec{G})\cdot\vec{R}\right), z > z_m \tag{2.13}$$

where Φ is the work function of the sample, $\vec{R}$ and $\vec{G}$ are the lateral position vectors ($\vec{r} = \vec{R} + z\hat{z}$) and reciprocal lattice vectors, respectively, $c_{\mu;\vec{k}+\vec{G}}(z_m)$ are the lateral plane wave coefficients at $z = z_m$ and $\epsilon_{\mu;\vec{K}}$ is referenced with respect to the sample Fermi level ϵ_{F}.

2.2 Infrared absorption spectroscopy

Infrared spectroscopy [50], [51],[52] is used to investigate the vibrational energies of a molecular system and to identify the system from the finger print of vibrational energies. A molecular complex such as a gas-phase molecular compound is irradiated by an infrared beam at different frequencies (a typical range is 1300-4000 cm^{-1}). The vibrational modes couple to the IR photons through the dynamic dipole moment and adsorb photons when the IR frequency matches the frequency of a vibrational mode. On metal surfaces, due to the metallic screening the IR beam does not penetrate into the bulk and is almost totally reflected, and the technique, reflection absorption infrared spectroscopy (RAIRS), becomes surface sensitive. Furthermore, the dynamic dipole moment is perpendicular to the surface.

2.2.1 Vibrations in the harmonic approximation

A starting point to describe the nature of the vibrations of a system is the harmonic approximation. Here we begin by discussing the vibrations of an one-dimensional system in the harmonic approximation and end by showing the results for a multi-dimensional system corresponding to a collection of atoms.

In the harmonic approximation for the motion of a particle in one-dimensional potential $V(x)$, only terms up to second order are kept in the Taylor expansion of $V(x)$ around the equilibrium position x_0:

$$V_{\mathrm{harm}}(x) = V(x_0) + \frac{dV}{dx}|_{x=x_0}(x - x_0) + \frac{d^2V}{dx^2}|_{x=x_0}\frac{(x - x_0)^2}{2} \tag{2.14}$$

Since the force is zero at x_0, the second term in this expansion is zero. The force from this harmonic potential is then linear in the displacement from the equilibrium position,

$$F(x) = -\frac{dV}{dx} = -k(x - x_0). \tag{2.15}$$

where

$$k = \frac{1}{2}\frac{d^2V}{dx^2}|_{x=x_0} \tag{2.16}$$

is the force constant. The equation of motion for the displacement $u = x - x_0$ is then by Newton's second law given by,

$$m\frac{d^2}{dt^2}u = -ku \tag{2.17}$$

where the m is the mass of the particle. The solutions of this equation correspond to an harmonic vibrational motion,

$$u(t) = A\cos(2\pi\nu t + \phi) \tag{2.18}$$

with a frequency ν given by,

$$\nu = \frac{1}{2\pi}\sqrt{\frac{k}{m}} \tag{2.19}$$

or alternatively given by the trivial eigen-value problem,

$$\frac{d^2V}{dx^2}|_{x=x_0}u = (2\pi\nu)^2 mu\ . \tag{2.20}$$

Now we turn to the multi-dimensional problem of a system of M atoms. The displacement of an atom I from its equilibrium position is here denoted by $\vec{u}_I$. In the harmonic approximation, the PES, V, is only expanded to second order in $\vec{u}_I$ and one obtains that Eq. (2.21) generalises to a generalised eigen-value problem in $3M$ dimensions for the different vibrational modes i and frequencies ν_i,

$$\sum_{I'=1}^{M}\sum_{\alpha'=1}^{3}\left(H_{I\alpha;I'\alpha'} - (2\pi\nu_i)^2 M_{I\alpha;I'\alpha'}\right)u_{i;I'\alpha'} = 0 \tag{2.21}$$

where α is a Cartesian index. The force constant matrix $H_{I\alpha;I'\alpha'}$ is now given by the second partial derivatives of V with respect the positions of the atoms at the equilibrium configuration as

$$H_{I\alpha;I'\alpha'} = \frac{\partial^2 V}{\partial R_{I\alpha} \partial R_{I'\alpha'}} \tag{2.22}$$

and $M_{I\alpha;I'\alpha'}$ is the mass matrix defined as,

$$M_{I\alpha;I'\alpha'} = M_I \delta_{II'} \delta_{\alpha\alpha'} \ , \tag{2.23}$$

where M_I is the mass of atom I.

Finally, in IR spectroscopy of vibrations at metal surfaces, the absolute intensity $I_{i,abs}$ of a vibrational mode i is determined by the change of the perpendicular dipole moment μ with the amplitude of the mode and,

$$I_{i,abs} \propto | \sum_{I'=1}^{M} \sum_{\alpha'=1}^{3} \frac{\partial \mu}{\partial u_{I\alpha}} u_{i;I\alpha} |^2 \ . \tag{2.24}$$

In this thesis, we are not just considering the fundamental vibrational modes but also the overtones. In IR spectroscopy, they will appear either be electrical or mechanical anharmonicity but they are typically very weak. Electrical anharmonicity arises from non-linear terms in the expansion of the dipole moment with respect to the amplitude of the vibrational modes. Mechanical anharmonicity corresponds to higher order terms in the displacements than quadratic in the PES.

2.3 Sum frequency generation

Since the advent of pulsed lasers in the picosecond down to the femtosecond regime with the concomitant high intensity of the pulses, it is possible to probe the non-linear optical response of the material. In contrast, traditional IR spectroscopy probes the linear response. The polarization, $\vec{P}$, response of the material to an external electric field can be expanded in powers of the electric field, [53], [54] $\vec{E}$ as,

$$P = \epsilon_0 \left(\chi^{(1)} E + \chi^{(2)} E^2 + \chi^{(3)} E^3 \ ... \right) \tag{2.25}$$

where ϵ_0 is the vacuum permittivity, $\chi^{(i)}$ is the ith order nonlinear susceptibility (tensor), and the space-time coordinates and the Cartesian indices have been suppressed. In Sum Frequency Generation (SFG), the sample is irradiated by two pulsed beams, one in the visible range of frequency and one in the IR range [7], [55], [56]. The electric field of the sum frequency beam is then proportional to the second-order term of the polarisation,

$$P^2(\omega + \omega') = \chi^2 E_{\mathrm{VIS}}(\omega) E_{IR}(\omega') \ , \tag{2.26}$$

where E_{VIS} and E_{IR} are the electric fields of the visible and infrared beams, respectively.

The surface sensitivity of SFG arises from the breaking of inversion symmetry at the surface. This sensitivity can be understood from the following argument that the second order susceptibility is zero for an inversion symmetric material. Since the electric fields and the polarisation are vectors, they change their sign under inversion, whereas the second order susceptibility is invariant for an inversion-symmetric material and from Eq. (2.26) one obtains under inversion,

$$-P^{(2)}(\omega+\omega') = \chi^{(2)}(-E_{VIS}(\omega))(-E_{IR}(\omega')) \tag{2.27}$$

However, Eqns. (2.26) and (2.27) can only be fulfilled if $\chi^{(2)} = 0$. Thus SFG is forbidden in a bulk material possessing inversion symmetry but is permitted at the surface of this material where the inversion symmetry is broken.

The second order polarisation given by Eq. 2.25 radiates an electric field at the sum of the frequencies of the IR and visible photons. The sources of the radiated sum frequency field are the vibrational and, possibly, electronic transitions of the adsorbed molecules and the surface itself, described by their respective susceptibilities:

$$\chi^{(2)} = \chi^{(2)}_{\mathrm{res}} + \chi^{(2)}_{\mathrm{NR}} \tag{2.28}$$

The resonant part of the susceptibility, $\chi^{(2)}_{\mathrm{res}}$ and the SFG beam intensity is greatly enhanced when the infrared field has a frequency corresponding to that of a molecular vibrational mode. In contrast to RAIRS, the intensity of the vibrational modes is not determined by the perpendicular dipole moment, which makes it possible to observe vibrational modes that are not dipole active. Furthermore, the high intensity of the pulsed, broad band beam makes it possible to populate vibrationally excited states and to probe vibrational overtones.

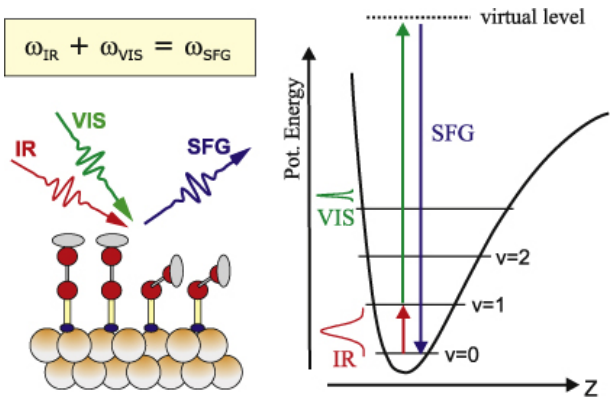

Figure 2.2: Schematic representation of femtosecond broadband SFG. The left panel shows the beam geometry in a reflection experiment. The right panel shows the interaction of the vibrational modes with a broad-spectrum IR pulse. [57]

Chapter 3

Theory and methodology

3.1 Introduction

In this chapter some of the key mathematical methods and theorems behind the development of electronic structure calculations based on density functional theory (DFT) are discussed. In the first part are discussed some early attempts of attacking the quantum many body problem of interacting electrons and nuclei and their limits. Next DFT is introduced to show how some of these limits can be circumvented. The fundamental principles and theorems of DFT are outlined in Section 3.5. In the Section 3.6, some details of the PBE and optB86b-vdW functionals used in thesis are presented. Section 3.7 shows some methods that are used in this thesis to solve the Kohn-Sham equations of DFT.

3.2 The quantum many-body problem

The quantum many-body problem [58], [59], [60], [61] for a system of N electrons in the presence of M nuclei amounts to the solution of the time-independent Schrödinger Equation 3.1.

$$\hat{H}\Psi(x_1, ..., x_N, \vec{R}_1, ..., \vec{R}_M) = E\Psi(x_1, ..., x_N, \vec{R}_1, ..., \vec{R}_M) \tag{3.1}$$

where $\Psi(x_1, ..., x_N, \vec{R}_1, ..., \vec{R}_M)$ is the wave function of the many-body system, $x_i = (\vec{r}_i, s_i)$ is the spatial and spin coordinates, $\vec{r}_i$ and s_i, respectively, of electron i and $\vec{R}_I$ is the spatial coordinates of nuclei I. This wave function has to be anti-symmetric in the electron coordinates. The Hamiltionian, $\hat{H}$, is determined by the kinetic energies of the electrons and the nuclei and the Coulomb interaction energies among electrons

and nuclei as,

$$\hat{H} = -\frac{\hbar^2}{2m_e}\sum_{i=1}^{N}\nabla_i^2 - \sum_{i=1}^{N}\sum_{I=1}^{M}\frac{Z_I e^2}{|\vec{r}_i - \vec{R}_I|} + \frac{1}{2}\sum_{i=1}^{N}\sum_{j\neq i}^{N}\frac{e^2}{|\vec{r}_i - \vec{r}_j|} \tag{3.2}$$

$$-\frac{\hbar^2}{2M_I}\sum_{I}^{M}\nabla_I^2 + \frac{1}{2}e^2\sum_{I=1}^{M}\sum_{J\neq I}^{M}\frac{Z_I Z_J}{|\vec{R}_I - \vec{R}_J|}$$

where m_e is the electron mass and M_I and $Z_I e$ is the mass and charge of nuclei I, respectively.

A most important simplification of this problem is provided by the Born-Oppenheimer approximation, which is based on the the fact that the motion of the nuclei is much slower than the electronic motions, so that one can first solve for the ground-state wave function ψ_0 and energy E_0 of the many-electron system for fixed nuclear positions,

$$\hat{H}_{el}\Psi_0(x_1, ..., x_N; \vec{R}_1, ..., \vec{R}_M) = E_0(\vec{R}_1, ..., \vec{R}_M)\Psi_0(x_1, ..., x_N; \vec{R}_1, ..., \vec{R}_M) \tag{3.3}$$

Here $\hat{H}_{el}$ is the many-electron Hamiltonian and lacks the kinetic energy term of the nuclei,

$$\hat{H}_{el} = -\frac{\hbar^2}{2m_e}\sum_{i}^{N}\nabla_i^2 - \sum_{i=1}^{N}\sum_{I=1}^{N}\frac{Z_I e^2}{|\vec{r}_i - \vec{R}_I|} + \frac{1}{2}\sum_{i=1}^{N}\sum_{j\neq i}^{N}\frac{e^2}{|\vec{r}_i - \vec{r}_j|} + \frac{1}{2}e^2\sum_{I=1}^{M}\sum_{J\neq I}^{M}\frac{Z_I Z_J}{|\vec{R}_I - \vec{R}_J|}\,. \tag{3.4}$$

The ground-state energy $E_0(\vec{R}_1, ..., \vec{R}_M)$ now acts as a potential energy for the nuclear motion.

However, Eq.(3.3) is only analytically solvable in the trivial case of an hydrogen atom due to the large number variables otherwise. To give an idea about the number of variables needed, we can consider the case of CO_2 as an example. The number of electrons of CO_2 dioxide is 22, which means that the number of variables is 66. Thus approximate and numerical methods are needed to solve Eq.(3.3).

3.3 The variational principle

A most important method to find the ground state wave function ψ_0 and energy E_0 of the many-electron Hamiltonian, Eq.(3.3), is provided by the variational principle which turns this eigen-value problem into a minimization problem. This principle is based on the fact that the expectation value of a normalized, trial wave function ψ_{trial} with respect to an Hamiltonian is always larger or equal to the corresponding expectation value of the ground state wave function,

$$E_{\text{trial}} = \langle\Psi_{\text{trial}}|\,\hat{H}\,|\Psi_{\text{trial}}\rangle \geq \langle\Psi_0|\,\hat{H}\,|\Psi_0\rangle = E_0 \tag{3.5}$$

In particular, the expectation value is only equal to E_0 when the trial wave function is equal to the ground-state wave function. In constructing the trial wave function of a many-electron system, it has to be anti-symmetric.

3.4 The Hartree-Fock approximation

Hartree-Fock approximation, [61] amounts to finding the non-interacting, many-electron wavefunction Φ that minimises $\langle\Phi|\,\hat{H}_{el}\,|\Phi\rangle$. The corresponding trial wavefunction for an N electron system is then given by a Slater determinant,

$$\Phi(x_1,...,x_N) = \frac{1}{\sqrt{N!}}\begin{vmatrix} \chi_1(x_1) & \chi_2(x_1) & \dots & \chi_N(x_1) \\ \chi_1(x_2) & \chi_2(x_2) & \dots & \chi_N(x_2) \\ \dots & \dots & \dots & \dots \\ \chi_1(x_N) & \chi_2(x_N) & \dots & \chi_N(x_N) \end{vmatrix} \tag{3.6}$$

where the ortho-normal, one-electron wave function $\chi_i(x)$ in spin-restricted Hartree-Fock is a product of a spatial orbital $\phi_i(\vec{r})$ and a spin function, $\sigma_i(s)$. Using, the variational principle, Eq. (3.5). we can now find the best Φ function by minimizing the expectation value of the hamiltonian by varying ϕ_i.

The expectation value of $\hat{H}_{el}$ with respect to Φ is given by,

$$E(\phi_1,...,\phi_N) = \langle\Phi|\,\hat{H}\,|\Phi\rangle = \sum_i^N \langle i|\,\hat{H}\,|i\rangle + \frac{1}{2}\sum_i^N\sum_j^N \langle ii|\,|jj\rangle - \langle ij|\,|ji\rangle \tag{3.7}$$

where (in atomic units)

$$\langle i|\,\hat{H}\,|i\rangle = \int \phi_i^*(\vec{r})[-\frac{1}{2}\nabla^2 - \sum_I^M \frac{Z_I}{|\vec{r}-\vec{R}_I|}]\phi_i(\vec{r})d\vec{r} \tag{3.8}$$

gives the contribution from the kinetic energy and the electron-nucleus attraction for spin-orbital i and

$$\langle ii|\,|jj\rangle = \int\int |\phi_i(\vec{r}_1)|^2 \frac{1}{|\vec{r}_1-\vec{r}_2|}|\phi_j(\vec{r}_2)|^2 d\vec{r}_1 d\vec{r}_2 \tag{3.9}$$

and

$$\langle ij|\,|ji\rangle = \int\int \phi_i(\vec{r}_1)\phi_j^*(\vec{r}_1)\frac{1}{|\vec{r}_1-\vec{r}_2|}\phi_j(\vec{r}_2)\phi_i^*(\vec{r}_2)d\vec{r}_1 d\vec{r}_2 \tag{3.10}$$

are the terms representing the Coulomb and exchange integrals respectively. The minimisation of $E(\phi_1,...,\phi_N)$ in Eq.(3.16) with respect to the spatial orbitals ϕ_i has to take into account the constraint that the spin orbitals have to be orthonormal. This constraint can be imposed by using Lagrange multipliers ϵ_i and ϕ_i are then determined by the Hartree-Fock equations,

$$\hat{f}\phi_i(\vec{r}) = \epsilon_i\phi_i(\vec{r}) \tag{3.11}$$

where

$$\hat{f} = -\frac{1}{2}\nabla_i^2 - \sum_{I=1}^{M} \frac{Z_I}{|\vec{r} - \vec{R}_I|} + \hat{V}_{HF} \ . \tag{3.12}$$

Here the first two terms correspond to the kinetic energy and the potential energy due to the electron-nuclei Coulomb attraction. The third term in Eq.(3.12) is the Hartree-Fock potential operator which has two terms,

$$\hat{V}_{HF}\phi_i(\vec{r}) = \sum_{j=1}^{N} (\hat{j}_j\phi_i(\vec{r}) - \hat{k}_j\phi_i(\vec{r})) \ . \tag{3.13}$$

where $\hat{j_j}$ and $\hat{k_j}$ are the local Coulomb and non-local exchange potential operators as obtained from Eqns. 3.9 and 3.10 as,

$$\hat{j}_j\phi_i(\vec{r}) = \int \frac{|\phi_j(\vec{r}')|^2}{|\vec{r} - \vec{r}'|} d\vec{r}' \phi_i(\vec{r}) \tag{3.14}$$

and

$$\hat{k}_j\phi_i(\vec{r}) = \int \frac{\phi_i(\vec{r}')\phi_j^*(\vec{r})}{|\vec{r}' - \vec{r}|} d\vec{r}' \phi_j(\vec{r}) \ . \tag{3.15}$$

The $\hat{j}_j$ represents the potential that an electron in an orbital $\phi_i(\vec{r})$ experiences due to the charge distribution of another electron in an orbital $\phi_j(\vec{r})$. In contrast, $\hat{k}_j\phi_i(\vec{r})$ leads to an exchange of the electron between the two orbitals if they have the same spin. The occurence of the exchange is due to the antisymmetry of the Slater determinant. The Hartree-Fock energy is now given in terms of the eigen-functions and -energies of $\hat{f}$ as,

$$E_{\text{HF}} = \sum_{i}^{N} \epsilon_i + \frac{1}{2} \sum_{i}^{N} \sum_{j}^{N} \langle ii| \, |ii\rangle - \langle ij| \, |ji\rangle \ . \tag{3.16}$$

Note that the Slater determinant of the eigen-functions is an eigen-state of the Hartree-Fock Hamiltonian given by,

$$\hat{H}_{\text{HF}} = \sum_{i} \hat{f}_i \ , \tag{3.17}$$

but the eigen-energy given by,

$$E_{\text{HF}}^{(0)} = \sum_{i} \epsilon_i \ , \tag{3.18}$$

differ from E_{HF}.

3.5 Density functional theory

3.5.1 Thomas-Fermi theory

The first approximation for the solution of the many-electron problem was suggested by Thomas and Fermi in the late twenties [27],[62] and is a precursor to density functional theory. The idea was to describe the many-electron system using a function of

only three space variables, namely the electron density. In the Thomas-Fermi approximation, the kinetic energy is approximated by using the kinetic energy density for an homogeneous electron gas and the electron-electron Coulomb interaction energy is approximated by the Coulomb energy of the electron density. The total energy is then a functional of the electron density and is given by

$$E_{TF}[\rho(\vec{r})] = \frac{3}{10}(3\pi^2)^{\frac{2}{3}} \int \rho^{\frac{5}{3}}(\vec{r})d\vec{r} - Z\int \frac{\rho(\vec{r})d\vec{r}}{r} + \frac{1}{2}\int\int \frac{\rho(\vec{r_1})\rho(\vec{r_2})}{r_{\vec{12}}} d\vec{r_1}d\vec{r_2} \quad (3.19)$$

The ground-state density and energy is then obtained by miminimising $E_{TF}[\rho(\vec{r})]$ under the constraint that the total number of electrons is constant. However, this simple approximation for the kinetic energy is not able to describe chemical bonding but, as indicated in the next Sections, this problem was solved by Kohn and Sham within DFT by their much more accurate approximation of the kinetic energy.

3.5.2 The Hohenberg-Kohn Theorems

An important development of solving the many-electron problem was carried out by, Hohenberg and Kohn in 1964 [28] who showed that the ground state wavefunction and energy is determined by the electron density. This development was based on the following two theorems.

Theorem 1 (First Hohenberg-Kohn theorem) *For any system of interacting particles in an external potential $V_{\rm ext}(\vec{r})$, the potential $V_{\rm ext}(\vec{r})$ is determined uniquely, except for a constant, by the ground state electron density $\rho(\vec{r})$.*

Theorem 2 (Second Hohenberg-Kohn theorem) *A universal functional for the energy $E[\rho(\vec{r})]$ in terms of the electron density $\rho(\vec{r})$ can be defined, valid for any external potential $V_{ext}(\vec{r})$. For any particular $V_{ext}(\vec{r})$, the exact ground state energy of the system is the global minimum value of this functional, and the density $\rho(\vec{r})$ that minimizes the functional is the exact ground state density $\rho_0(\vec{r})$*

In order to prove the first theorem, we have to consider two external potentials $V_{\rm ext}(\vec{r})$ and $V'_{\rm ext}(\vec{r})$ which differ by more than a constant. The corresponding Hamiltonians, are given by $\hat{H} = \hat{T} + \hat{V_{ee}} + \hat{V}_{ext}$ and $\hat{H}' = \hat{T} + \hat{V}_{ee} + \hat{V}'_{\rm ext}$, where $\hat{T}$ is the kinetic energy operator and $\hat{V_{ee}}$ is the electron-electron repulsion. We can now prove this theorem by showing that the two ground states $\langle\Psi_0|$ and $\langle\Psi'_0|$ and energies E_0 and E'_0 of $\hat{H}$ and $\hat{H}'$, respectively, cannot have the same electron density. First, we obtain from the variational principle, Eq. 3.5 that

$$E_0 < \left\langle\psi'\right| \hat{H} \left|\psi'\right\rangle = \left\langle\psi'\right| \hat{H}' \left|\psi'\right\rangle - \left\langle\psi'\right| \hat{H} - \hat{H}' \left|\psi'\right\rangle \ , \quad (3.20)$$

which simplifies to,

$$E_0 < E_0' + \left\langle \psi' \right| \hat{V}_{ext} - \hat{V}'_{ext} \left| \psi' \right\rangle \tag{3.21}$$

Assuming that the two ground states have the same electron density $\rho(\vec{r})$ one obtains

$$E_0 < E_0' + \int \rho(\vec{r})(V_{\text{ext}}(\vec{r}) - V'_{\text{ext}}(\vec{r}))d\vec{r} \tag{3.22}$$

Now by interchanging the unprimed with the primed quantities, one obtains also that

$$E_0' < E_0 - \int \rho(\vec{r})(V_{\text{ext}} - V'_{\text{ext}})d\vec{r} \tag{3.23}$$

By adding these two equations, one obtains the contradictory result that $E_0 + E_0' < E_0' + E_0$. Thus, the ground-state electron densities have to be different, which proves the theorem.

In order to prove the second theorem, we assume that for any $\rho(\vec{r})$ there exists a $V_{\text{ext}}(\vec{r})$ so that $\rho(\vec{r})$ is the ground state electron density of the corresponding Hamiltonian. According to the first theorem, this potential is determined up to constant and the corresponding groundstate will be unique. Thus we can define an universal functional as,

$$F[\rho] = \langle \Psi | \hat{T} + \hat{V}_{ee} | \Psi \rangle \tag{3.24}$$

where $\langle \Psi |$ is the ground state wavefunction that generates $\rho(\vec{r})$. Furthermore, we can define the energy functional for any system as defined by an external potential $V'_{\text{ext}}(\vec{r})$ as,

$$E'[\rho] = F[\rho] + \int \rho(\vec{r}) V'_{\text{ext}}(\vec{r}) d\vec{r} \tag{3.25}$$

According to the variational principle,

$$E'[\rho] = \langle \Psi | \hat{H}' | \Psi \rangle \geq \left\langle \Psi' \right| \hat{H}' \left| \Psi' \right\rangle = E_0' \tag{3.26}$$

Thus, the minimum value of this energy functional is equal to the ground state energy E_0' of $\hat{H}'$ and the density that minimises $E'[\rho]$ is equal to the ground state electron density.

3.5.3 The Kohn-Sham equations

The Hohenberg-Kohn theorems show that it is sufficent to consider the electron density as the basic variable and that the ground state energy of a many-electron system can obtained by minimising an energy functional of the electron density. In order to proceed one needs to find an approximation of the universal functional $F[\rho]$ defined in Eq. 3.30. In order to do that Kohn and Sham made the following decomposition of this functional [63],

$$F[\rho] = T_0[\rho] + U[\rho] + E_{\text{XC}}[\rho] \tag{3.27}$$

Here $T_0[\rho]$ is the kinetic energy of a fictious non-interacting many-electron system with electron density $\rho(\vec{r})$, $J[\rho]$ is the Coulomb energy of the electron density,

$$J[\rho] = \int\int \frac{\rho(\vec{r}_1)\rho(\vec{r}_2)}{|\vec{r}_1 - \vec{r}_2|} d\vec{r}_1 d\vec{r}_2 \tag{3.28}$$

and the rest term $E_{\mathrm{XC}}[\rho]$ is called the exchange-correlation energy. The wave function of the non-interacting electron system has the same form as for the trial wave function in Hartree-Fock in Eq. 3.30. The electron density and the kinetic energy of this system is then simply given by,

$$\rho(\vec{r}) = \sum_{i=1}^{N} |\phi_i(\vec{r})|^2 \tag{3.29}$$

and

$$T_0 = -\frac{1}{2} \sum_{i=1}^{N} \langle \phi_i | \nabla^2 | \phi_i \rangle \ , \tag{3.30}$$

respectively. As in Hartree-Fock, the energy functional is now minimized with respect to variations of the orbitals $\phi_i(\vec{r})$ under the constraint the orbitals are orthonormalised. The orbitals then satisfies the Kohn-Sham equations,

$$\hat{f}^{KS}\phi_i = \epsilon_i \phi_i \tag{3.31}$$

where

$$\hat{f}^{KS} = -\frac{1}{2}\nabla^2 + V_{\mathrm{KS}}(\vec{r}) \ . \tag{3.32}$$

The Kohn-Sham potential $V_{\mathrm{KS}}(\vec{r})$ is now determined by the functional derivatives of $U[\rho]$, $J[\rho]$ and $E_{\mathrm{XC}}[\rho]$, and the electron-nuclei interaction (the external potential) as,

$$V_{\mathrm{KS}}(\vec{r}) = \int \frac{\rho(\vec{r}')}{|\vec{r} - \vec{r}'|} d\vec{r}' + V_{XC}(\vec{r}) - \sum_{I=1}^{M} \frac{Z_I}{|\vec{r} - \vec{R}_I|} \ . \tag{3.33}$$

where

$$V_{XC}(\vec{r}; \rho) = \frac{\delta E_{\mathrm{XC}}[\rho]}{\delta \rho(\vec{r})} \ . \tag{3.34}$$

In contrast to the Hartree-Fock potential in Eq. (3.30), the Kohn-Sham potential is a local potential and depends only on the orbitals through the electron density, which makes it more simpler to solve the Kohn-Sham equations than the Hartree-Fock equations,.

The different energy terms to the total energy,

$$E = T_0[\rho] + U[\rho] + E_{\mathrm{XC}}[\rho] - \int \sum_{I=1}^{M} \frac{Z_I \rho(\vec{r})}{|\vec{r} - \vec{R}_I|} d\vec{r} \tag{3.35}$$

can now obtained by finding the N lowest solutions (including spin degeneracy) and energies of the Kohn-Sham equations. The kinetic energy is obtained from Kohn-Sham energies and the electron density, Eq. 3.30, as,

$$T_0 = \sum_i \epsilon_i - \int V_{\mathrm{KS}}(\vec{r}, \rho)\rho(\vec{r})d\vec{r} \tag{3.36}$$

whereas the remaining terms are obtained directly from the electron density.

3.5.4 Hellmann-Feynman Forces

The optimisation of the geometric structure of a system by minimising the energy, is most efficiently done by using the forces on the nuclei. The force $\vec{F}_I$ on an ion I is given by,

$$\vec{F}_I = -\frac{\partial E}{\partial \vec{R}_I} \tag{3.37}$$

Hellmann and Feynman [59], showed that these forces can be obtained directly from the electron density and it is not necessary to calculate the forces from the calculated total energies. In DFT, this fact can be demonstrated directly in the following manner. Using Eq. 3.35 for the energy functional, one obtains

$$\vec{F}_I = -\int [\frac{\delta F}{\delta \rho(\vec{r})} + V_{\mathrm{ext}}(\vec{r})]\frac{\partial \rho}{\partial \vec{R}_I}(\vec{r})d\vec{r} - \int \frac{\partial V_{\mathrm{ext}}}{\partial \vec{R}_I}(\vec{r})]\rho(\vec{r})d\vec{r}\,. \tag{3.38}$$

The first integral is now zero since the functional derative of the energy functional is a constant over space for the ground state density and the number of electrons is constant when varying $\vec{R}_I$. Thus, the forces are given by the second term as,

$$\vec{F}_I = -\int \frac{\partial V_{\mathrm{ext}}}{\partial \vec{R}_I}(\vec{r})\rho(\vec{r})d\vec{r}. \tag{3.39}$$

Note there will also be a contribution from the Coulomb repulsion between the nuclei.

3.6 Exchange and correlation in DFT approximations

In this section, the origin of the exchange-correlations functionals, PBE and optB86b-vdw, used in this thesis is discussed.

3.6.1 The homogeneous electron gas

Many exchange-correlation functionals such as the semi-local functionals used in this thesis are based on the homogeneous electron gas which is often refered to as jellium. In this model, the ion-cores are smeared out to a positive homogenous background and is characterized by single parameter the electron density ρ. For this system, the

Kohn-Sham wavefunctions are simply plane waves. The exchange part of E_{XC}, as defined by the second term in Eq. (3.30), but now based on the KS wave functions, can be evaluated analytically for plane waves as first done by Fermi [59]. The resulting exchange energy per electron is given by (atomic units),

$$\varepsilon_{\mathrm{X}}[\rho] = -\frac{3}{4}(\frac{3}{\pi})^{\frac{1}{3}}\rho^{\frac{1}{3}} = -\frac{3}{4}(\frac{9}{4\pi^2})\frac{1}{r_s}$$

where r_s is the average inter-electronic distance. The remaining part of E_{XC}, the correlation energy E_{C} cannot be evaluated analytically but has been calculated accurately by Ceperley and Alder using a quantum Monte Carlo method [64], [65]. The resulting correlation energy per electron is well represented by,

$$\varepsilon_{\mathrm{C}}[\rho] = \begin{cases} A\ln r_s + B + Cr_s\ln r_s + Dr_s, r \leq r_s \\ \frac{\gamma}{(1+\beta_1\sqrt{r_s}+\beta_2 r_s)}, r > r_s \end{cases} \tag{3.40}$$

Here $r_s = (\frac{3}{4}\pi\rho)^{\frac{1}{3}}$, whereas the parameters calculate have the values of A=0.0311, B=-0.048 C=0.002, D=-0.016 with $\gamma = -0.1423$, $\beta_1 = 1.0529$ and $\beta_2 = 0.3334$ for the spin-unpolarized case [60].

3.6.2 Local density approximation

The local density approximation (LDA) was one of the first successful approximations of the exchange-correlation energy and is based on the exchange-correlation energy for the homogeneous electron gas. The idea behind this approximation is to consider an inhomogeneous many-electron system as locally homogeneous, and therefore to use the homogeneous energy functional only locally. The exchange-correlation energy is then approximated by the volume integral of the electron density times the exchange-correlation energy per electron for the homogeneous electron gas at this electron density as,

$$E_{\mathrm{XC}}^{\mathrm{LDA}}[\rho] = \int \rho(\vec{r})\varepsilon_{\mathrm{xc}}[\rho(\vec{r})]d\vec{r} \tag{3.41}$$

The success of the LDA can in part be understood from the expression of the exchange-correlation energy in terms of the exchange-correlation hole density $\rho_{\mathrm{xc}}(\vec{r},\vec{r}')$ which essentially gives the deviation of the electron density from the average electron density at a position $\vec{r}'$ for an electron at $\vec{r}$ [60]. The presence of an electron at $\vec{r}$ will reduce the probability of finding an another electron at $\vec{r'}$ in the vicinity of $\vec{r}$ due to exchange and correlation. Since one electron is singled out this hole density satifies the important sum rule,

$$\int \rho_{\mathrm{xc}}(\vec{r},\vec{r}')d\vec{r}' = -1 \tag{3.42}$$

The exchange-correlation energy is then given by the Coulomb interaction of the electron density with the exchange-correlation hole density as,

$$E_{\mathrm{XC}}[\rho] = \frac{1}{2}\int\int \frac{\rho(\vec{r})\rho_{\mathrm{xc}}(\vec{r},\vec{r}')}{|\vec{r}-\vec{r}'|}d\vec{r}'d\vec{r}' \ . \tag{3.43}$$

This expression shows that it is only the spherical average of the hole density that is important and also that it is important that any approximation for the hole density satisfies the hole sum rule in Eq. [60]. The LDA for exchange-correlation energy in Eq.(3.41) amounts to approximating exchange hole density $\rho_{\mathrm{xc}}(\vec{r},\vec{r}')$ with the one for the homogeneous electron gas, $\rho_{\mathrm{xc}}^{\mathrm{hom}}(|\vec{r}-\vec{r}'|,\rho(\vec{r}))$, at the local electron density, which satisfies the hole sum-rule and is spherically symmetric.

The LDA is a very succesful approximation for many systems of interest, in particular for systems where the electronic density is relative uniform such as metals or semiconductors but even for some molecular complexes. Another problem is the exponential decay of the exchange-correlation potential rather than the $\frac{-e}{r}$ decay.

3.6.3 Generalised gradient approximation GGA

The exchange energy in generalised gradient approximation (GGA) [66], [67] has the form:

$$E_{\mathrm{X}}^{\mathrm{GGA}}[n] = \int d^3r \epsilon_{\mathrm{X}}^{\mathrm{hom}}(\rho(\vec{r}))F_{\mathrm{X}}(s(\vec{r})) \tag{3.44}$$

The factor F_{X} is the exchange enhancement factor, which tells how much exchange is enhanced over its LDA value due to the inhomogeus electron density as described by the dimensionless function $s(\vec{r})$ defined as,

$$s(\vec{r}) = \frac{|\nabla\rho(\vec{r})|}{2k_F\rho(\vec{r})} \tag{3.45}$$

This function takes into account of the inhomogeneous electron density through it gradient. The functional form of $F_{\mathrm{X}}(s(\vec{r}))$ is restricted by some physical conditions but is not unique and has led to many different parametrisations and different versions of the GGA functionals such as Perdew-Burke-Ernzerhofer (PBE) [66] and Becke's B88 functional [68]. The correlation part of the exchange-correlation energy is handled in a similar manner.

3.6.4 The Van der Waals density functional

The Van der Waals interaction is due to electron-electron correlations and is important to include for large systems such as porphyrin molecules adsorbed on metal surfaces. In this thesis, we have used the optB86b-VdW version of the Van der Waals density

functional introduced by Kl′imes, et al.,[69]. This functional has the following form,

$$E_{\mathrm{XC}}^{\mathrm{optB86b-vdw}}[\rho] = E_{\mathrm{X}}^{\mathrm{optB86b}}[\rho] + E_{\mathrm{C}}^{\mathrm{LDA}}[\rho] + E_{\mathrm{c}}^{\mathrm{nl}}[\rho] \, . \tag{3.46}$$

The first term is the exchange part, which is described by the Becke86 exchange functional [60] and is a generalised gradient functional. The second term accounts for local correlations and is described by the LDA, whereas the third term accounts for non-local correlations associated with the van der Waals interactions. The functional form of this latter term is given by [60],

$$E_c^{nl}[\rho] = \frac{1}{2} \int d^3r d^3r' \rho(\vec{r}) \phi(\vec{r}, \vec{r}') \rho(\vec{r}') \tag{3.47}$$

where $\phi(\vec{r}, \vec{r}')$ is a non-local kernel.

3.7 Calculational methods

This section outlines how the Kohn-Sham (KS) equations, Eq. (3.30), can be solved.

3.7.1 The self-consistency problem

As shown in Section 3.6, the KS potential depends on the electron density which in turn is determined by the KS orbitals that solves the KS equations. This self-consistency problem can be solved by an iterative method as outlined below.

1. Define an initial electron density, for instance by a superposition of atomic densities, and use that as a trial electron density
2. Solve the KS equations, where the KS potential is obtained from the trial electron density, to find the KS orbitals and energies
3. Calculate the electron density from the Kohn-Sham orbitals from step 2
4. Compare the calculated electron density with the trial electron density. If the difference between the energies with the calculated density and the trial density is below a certain tolerance then the calculated electron density is choosen as the ground-state electron density and can be used to compute the total energy. If the two calculated energies differ with more than the tolerance, the trial electron density is updated from the calculated electron density and the process restarts from step 2.

3.7.2 Plane wave basis set

In this thesis the KS equations are solved for a given KS potential using a plane wave basis set. As outlined here, this turns the KS equations into an eigen-value problem for a matrix. The use of a plane wave basis set requires that the system can be be represented by a super cell with periodic boundary conditions.

As shown in Section 3.6, the KS equations have the form,

$$[-\frac{1}{2}\nabla^2 + V(\vec{r})]\psi_i(\vec{r}) = \epsilon_i\psi_i(\vec{r}) \tag{3.48}$$

Since we have periodic boundary conditions, the KS potential is periodic,

$$V(\vec{r}) = V(\vec{r} + \vec{R}) \; . \tag{3.49}$$

Here $\vec{R}$ is a lattice vector:

$$\vec{R} = n_1\vec{a_1} + n_2\vec{a_2} + n_3\vec{a_3} \tag{3.50}$$

where n_1, n_2 and n_3 are integers, From Bloch's theorem [70], the solutions of the KS equations, Eq. 3.49, have the following form,

$$\psi_{\vec{k}}(\vec{r}) = e^{i\vec{k}\cdot\vec{r}}u_{\vec{k}}(\vec{r}) \tag{3.51}$$

where $\vec{k}$ is a wave vector and $u_{\vec{k}}(\vec{r})$ is periodic

$$u_{\vec{k}}(\vec{r} + \vec{R}) = u_{\vec{k}}(\vec{r}) \tag{3.52}$$

Any periodic function such as $u(\vec{r})$ can be expanded in terms of plane waves as,

$$u(\vec{r}) = \sum_{\vec{G}} c_{\vec{k}}(\vec{G})e^{i\vec{G}\cdot\vec{r}} \tag{3.53}$$

where $\vec{G}$ are reciprocal lattice vectors defined as

$$\vec{G} = \sum_i m_i\vec{b_i} \tag{3.54}$$

where m_i, are integers, i = 1,2 and 3, and b_i are basis vectors of the reciprocal lattice determined by the condition $\vec{a}_i \cdot \vec{b}_j = 2\pi\delta_{ij}$. The full wave function is now given by,

$$\psi_{\vec{k}}(\vec{r}) = \sum_G c_k(\vec{G})e^{i(\vec{k}+\vec{G})\cdot\vec{r}} \tag{3.55}$$

The periodic KS potential can also be expanded in plane waves as,

$$V(\vec{r}) = \sum_G V(\vec{G})e^{i(\vec{G}\cdot\vec{r})}. \tag{3.56}$$

Inserting both Eqns. (3.55) and (3.56) in Eq. (3.48), the KS equations turn into the following eigen-value problem for each k-point in the first Brillouin zone,

$$\sum_{m'} H_{mm'}(\vec{k}) c_{\vec{k}}(\vec{G}_{m'}) = \epsilon(\vec{k}) c_{\vec{k}}(\vec{G}_m) \tag{3.57}$$

where the Hamiltonian matrix is given by,

$$H_{mm'}(\vec{k}) = \frac{|\vec{k} + \vec{G}_m|^2}{2} \delta_{mm'} + V(\vec{G_m} - \vec{G_{m'}}) \tag{3.58}$$

This matrix equation is made finite by truncating the plane wave basis set by introducing a plane wave energy cut-off,

$$\frac{|\vec{k} + \vec{G}|^2}{2} < E_{\text{cut}} \ . \tag{3.59}$$

The diagonalisation of the Hamiltonian matrix gives a set of eigenvalues $\epsilon_n(\vec{k})$ that are the KS energies of the n:th band with the eigenvectors $\vec{c}_{n,\vec{k}}$. From these eigenvectors, the KS orbitals are then determined. The accuraccy of the solutions can then be systematically improved by increasing E_{cut}. Finally, one has to sample the k points in the Brilluoin zone.

3.7.3 Pseudopotentials

Since the interactions between core electrons of different atoms are very weak, their wave functions can be well approximated to be frozen. This approximation means that only the valence electrons have to be treated explicitly. However, a major problem when using a plane wave basis set to represent the valence wave functions is their rapid oscillations in the core region due to their large kinetic energy in this region. To represent these solutions, one needs a very large plane-wave cut off corresponding to an unmanagable large number of plane waves. This problem can be handled by the psuedopotential method.

In this approach one introduces atomic pseudopotentials. It turns out that it is possible to find a pseudopotential for an atom such it gives rise to the same energies for the valence electrons and low-energy scattering properties as for the real potential but the corresponding pseudo wave function are smooth in the core region. The absence of rapid oscillations in the pseudo wave functions allows now for a rather low plane-wave cut off.

Chapter 4

Adsorption of RuTPP and CO-MTPP on Cu(110)

4.1 Introduction

In this Chapter, we present the results on the DFT calculations of the geometric and electronic structures of the RuTPP [71] and CO-RuTPP [50] complexes both in the gas-phase and adsorbed on the Cu(110) surface. The two main objectives of this study were (1) to find the adsorption geometry of the adsorbed CO-RuTPP complex in order to carry out the study of the observed anharmonicity of the internal CO stretch mode in Chapter 5; (2) to elucidate the mechanism behind the observed desorption of CO from an adsorbed CO-RuTPP molecule on the Cu(110) surface via an inelastic electron tunnelling process. The adsorption and self-assembly of porphyrins on metal surfaces is a widely studied topic because of their great interest in heterogeneous catalysis [72], [73], [74], gas sensors [37], light harvesting [24], , molecular switches [75] and field effect transistors [76]. A switch from a planar geometry to a saddle-shaped conformation of CoTBrPP on Cu(111) was observed at a temperature of 100 K [77]. Conformational changes of adsorbed porphyrin molecules have also been observed for other systems such in the reaction between between 2HTPP and Ni atoms on a TiO_2(110) surface [78]. Another example of self-assembly is the formation of ordered structure of adsorbed CoTPP molecules on Cu(111) and on Ag(111) with a preferred orientation.

For a comparison we have also performed calculations for the metalloporphyrins with Co and Zn metal centres and have also investigated the coverage dependence. DFT calculations of CO adsorption on Cu(110) [79], [26], [80] have been carried out previously but not with a density functional which includes van der Waals interactions as done here. We also make a comparison of calculated and observed STM images of the adsorbed CO-RuTPP and RuTPP. A comparison between scanning tunnelling

spectra of these molecule with calculated partial and local density of states is also attempted.

4.2 Computational details

The periodic DFT calculations of the geometric and electronic structure of the isolated gas-phase MTPP and when adsorbed on the Cu(110) surface for M=Ru, Co and Zn were carried out using the Vienna Ab initio Simulation Package (VASP)(version 5.3) , [81], [82]. The valence electron-core interactions were handled by the projector-augmented wave (PAW) method [83], [84]. The van der Waals interactions were included using optB86b-vdW version of the van der Waals exchange-correlation functional. The key input parameters of the calculations are essentially the same as used for similar systems such as CoTPP adsorption on Cu(110) [31] and Acrolein on Pt(111)[85].

The plane wave energy-cut off was set to 400 eV . The size of the super cell for the isolated molecule was 25x25x25 Å^3 and the Brillouin zone was sampled by the Γ point. One low and two high coverage structures, which were studied in the experiments, were considered for the adsorption of MTPP on Cu(110). The low coverage structure corresponds to a p(6x8) structure, while the two high coverage structures A^{δ} and A^{γ} are given in the standard matrix notation [86] by the matrices,

$$\begin{pmatrix} 2 & 4 \\ -7 & -2 \end{pmatrix} \tag{4.1}$$

and

$$\begin{pmatrix} 2 & 4 \\ -6 & -2 \end{pmatrix}, \tag{4.2}$$

respectively. These latter two structures had to be represented in skewed super cell. Due to the large super-cells for all these adsorbate structures, a k-point mesh of 2x2x1 was sufficient in the calculations. A four layer slab was used to represent the Cu surface. The vacuum region was 16.65 Å. The equilibrium geometries of all systems were obtained by structural relaxations of all atoms except in the case of the adsorbate structures where the Cu atoms in the two bottom layers of the slab were kept fixed until the forces were less than 0.01 eV Å^{-1}. The two bottom layer atoms were fixed at the value of 3.634 Å of the bulk lattice constant [31]. Finally, the STM images were simulated using the Tersoff-Hamann method [48] for each coverage of RuTPP/Cu(110).

4.3 Isolated MTPP

The geometric and electronic structure of an isolated MTPP, where M=Ru, Co or Zn, are investigated in this section with particular emphasis on the orientations of the phenyl rings.

4.3.1 Geometric structure

For all calculated equilibrium structures of MTPP, corresponding to M=Ru, Co and Zn, the starting geometry in the structural optimization was a nearly planar molecule with the M atom in the centre of the N atoms. Due to strong steric hindrance, the molecule becomes non-planar during the geometric optimization with a large twist of the phenyl rings (Fig. 4.1. The geometry of the phenyl rings are here characterized by a tilt angle and a twist angle which are defined in a similar manner as in Ref. [31]. The tilt angle Φ is defined as the angle between the direction along the bond between the C atom (C_m) in the macro cycle and the C atom (C_p) in the phenyl ring and the direction from the metal atom to the C_m atom. Note that here Φ is defined as 180° minus the tilt angle in Ref. [31]. As shown by Table 4.2, there are essentially no tilting of the phenyl rings and $\Phi \approx 0^\circ$ for all MTPP molecules. The twist angle Θ is defined here as the angle between the surface normals of the macro cycle and the phenyl ring and with the range $-90^\circ < \Theta \leq 90^\circ$. Since $\Phi = 0^\circ$, a positive and a negative Θ correspond to a clockwise and counter clockwise rotation around the macro cycle-phenyl axis, respectively.

4.3.2 Electronic structure

The electronic structure of the MTPP were characterized by the calculated partial DOS of the d partial waves around the metal centre, which are shown in Figs 4.2, 4.3 and 4.4 for M = Ru, Co and Zn, respectively. These PDOS show that d_σ^2 and d_π are partially occupied for Ru, whereas only d_σ is partially occupied for Co and all d states are fully occupied for Zn. These occupations are consistent with the calculated spin magnetic moments of RuTPP and CoTPP are $2\mu_B$, and $1\mu_B$, respectively, whereas ZnTPP was found to be non-magnetic. They also show that Ru, Co and Zn has essentially $(d_{x^2-y^2})^2(d_\pi)^3(d_{z^2})^1$, $(d_{x^2-y^2})^2(d_\pi)^4(d_{z^2})^1$ and $(d_{x^2-y^2})^2(d_\pi)^4(d_{z^2})^2(d_{xy})^2$ electronic configurations, respectively. The energy ordering of the d orbital levels cannot simply be reconciled with the ordering obtained by crystal field theory for a square planar tradition's metal ion complex (see, Section 1.4.3. For example, the $d_{x^2-y^2}$ energy levels tend to be about the same energy or lower as for the d_π orbitals. The

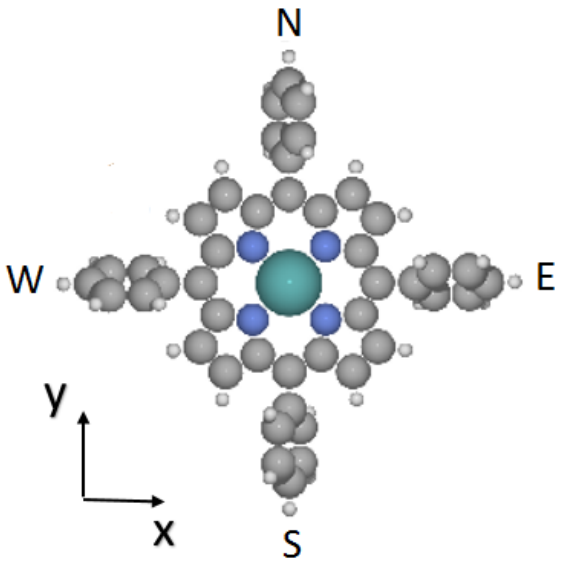

Figure 4.1: Calculated equilibrium structure of the isolated RuTPP. The short hand notation W(est), E(ast), N(orth), S(outh) refer to the different phenyl rings of the molecule. The coordinate axes which are used to define the different d orbitals are also indicated.

splitting of the d orbitals are instead governed by the covalent interactions with the ligands.

Finally, there have been some earlier DFT calculations of CoTPP and ZnTPP [87] but only for RuP [88] and not RuTTP. Our calculated bonding distances d(Co-N) = 1.965 Å, and d(Zn-N) = 2.045 Å between the metal atom and N atoms are in close agreement with the calculated ones, d(Co-N) = 1.97 Å, and d(Zn-N) = 2.05 Å by Liao and Scheiner [87]. The calulated d(Ru-N) = 2.024 Å is consistent with the calculated one d(Ru-N) = 2.06 Å for RuP. In addition, their calculated orbital energy levels for Rup, CoTPP and ZnTPP are consistent with our calculated partial density of states for Ru-, CO-, and Zn-TPP. Our calculated electronic configurations for these molecules agree with their results for Rup, CoTPP and ZnTPP.

4.4 Isolated CO-MTPP

4.4.1 Geometric structure and CO-adsorption energy

The optimized structures of CO-RuTPP and CO-CoTPP show different bonding geometries of CO on the metal centre. In both cases, the C atom is bonded to the metal centre and CO is oriented perpendicular to the molecular plane of RuTPP but tilted by an angle of 32° with respect to the surface normal of the molecular plane of CoTPP.

Molecule	Angle	W	E	N	S
RuTPP	Θ	-68	-67	70	69
	Φ	0	0	0	-1
CoTPP	Θ	-68	-68	70	69
	Φ	0	0	0	-1
ZnTPP	Θ	-59	-54	55	57
	Φ	1	-0	-3	3

Table 4.1: Calculated twist angles Θ and tilt angles Φ of the phenyl rings for the isolated molecule. The short hand notation W(est), E(ast), N(orth), S(outh) refer to the different phenyl rings of the MTPP molecule as indicated in Fig. 4.1

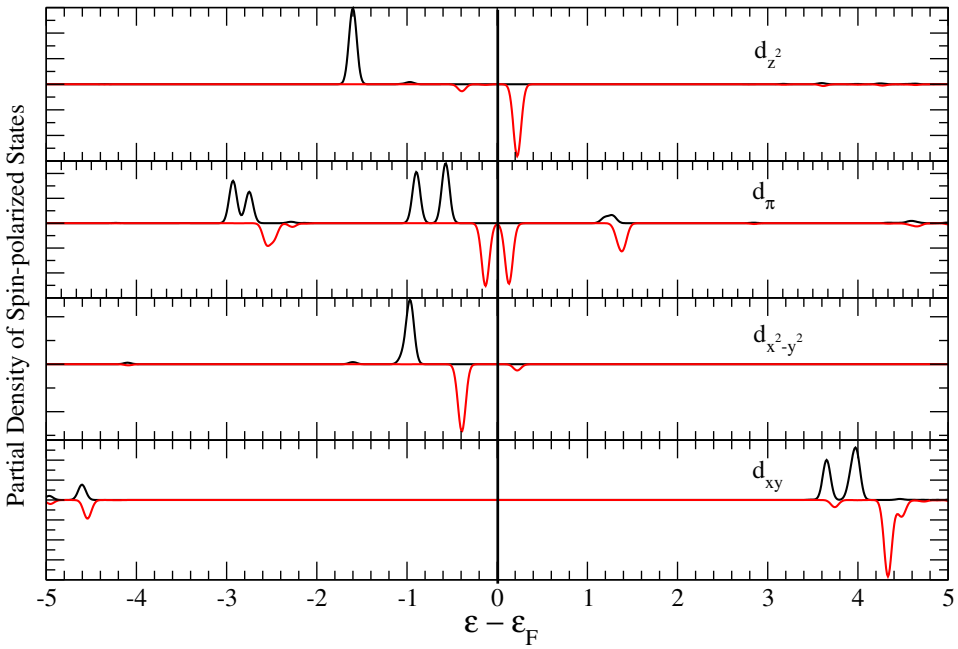

Figure 4.2: Partial DOS of isolated RuTPP molecule for different Ru d partial waves and for majority (black lines) and minority (red lines) spin. The orientation of the Cartesian axes are defined in Fig. 4.1. ($d_\pi = d_{xz} + d_{yz}$).

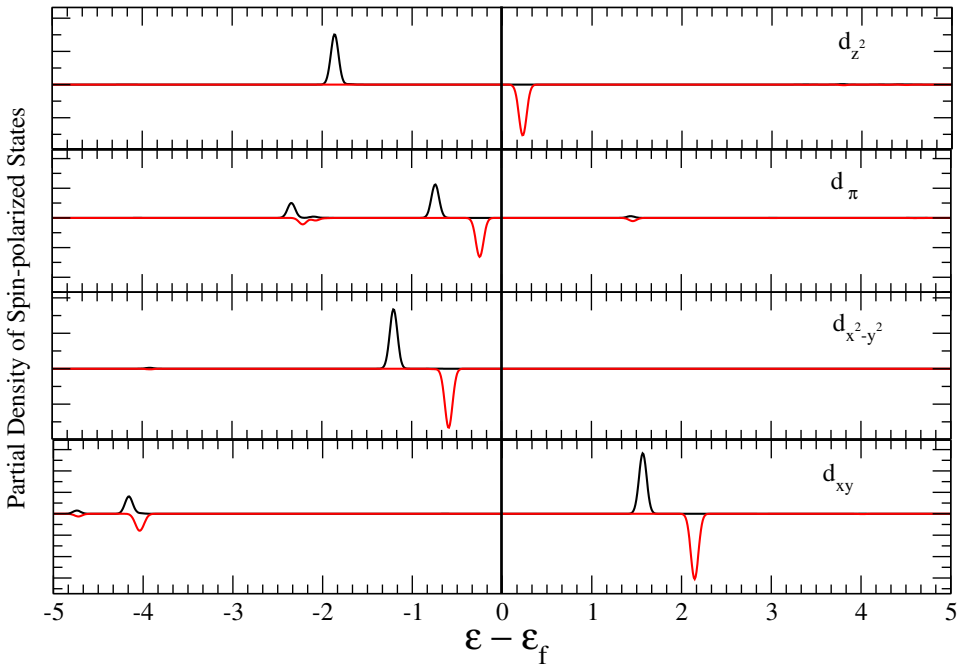

Figure 4.3: Partial DOS of isolated CoTPP molecule for different Co d partial waves and for majority (black lines) and minority (red lines) spin. The orientation of the Cartesian axes are defined in Fig. 4.1. ($d_\pi = d_{xz} + d_{yz}$).

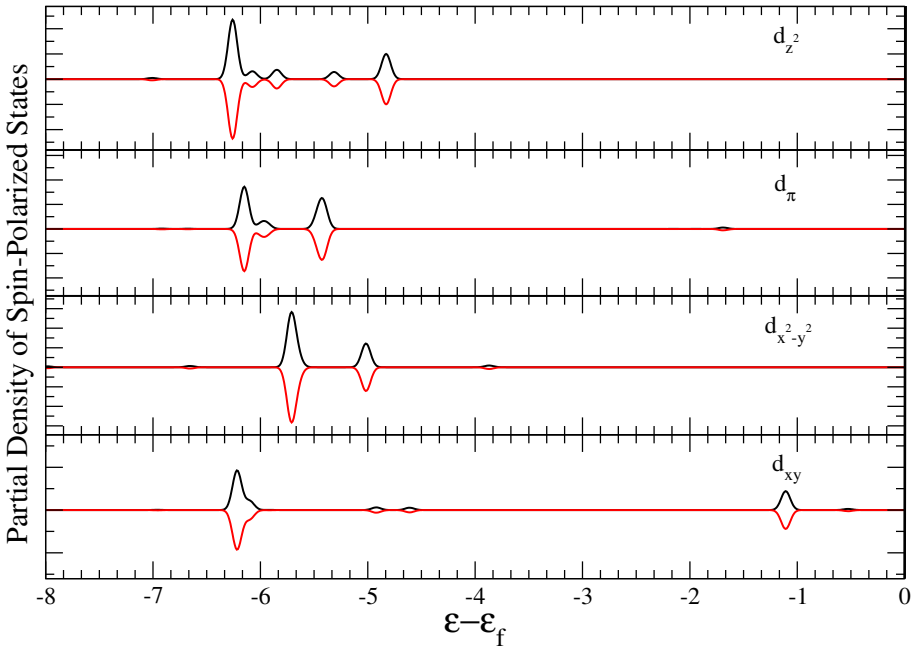

Figure 4.4: Partial DOS of isolated ZnTPP molecule for different Zn d partial waves and for majority (black lines) and minority (red lines) spin. The orientation of the Cartesian axes are defined in Fig. 4.1. ($d_\pi = d_{xz} + d_{yz}$).

The calculated C-O distances are 1.175 Å and 1.162 Å for CO-RuTPP and CO-CoTPP, respectively are larger than the distance of 1.143 Å for the isolated CO molecule. The calculated C-M distances for M = Ru and M = Co are quite similar and are given by 1.180 Å and 1.183 Å,respectively. As shown in Table 4.2, the bonding of CO to MTPP has only a minor effect on the twist angles Θ and the molecule is still planar ($\Phi \approx 0°$). Note that in the case of ZnTPP, no stable adsorption geometry of CO was identified, which is probably due to the closed d shell of the Zn atom.

The adsorption energy $E_{\rm ad}$ of CO on MTPP for M=Ru and Co were calculated as,

$$E_{\rm ad} = E_{\rm MTPP} + E_{\rm CO} - E_{\rm CO-MTPP}\ . \tag{4.3}$$

Molecule	Angle	W	E	N	S
CO-RuTPP	Θ	-61	-58	59	60
	Φ	3	0	-1	4
CO-CoTPP	Θ	-68	-68	61	69
	Φ	0	1	0	0

Table 4.2: Calculated twist angles Θ and tilt angles Φ of the phenyl rings for the isolated molecule. The short hand notation W(est), E(ast), N(orth), S(outh) refer to the different phenyl rings of the CO-MTPP molecule as indicated in Fig. 4.7(a)

A most interesting result from the calculated values is the much stronger bonding of CO on RuTPP than on CoTPP: E_{ad} = 2.87 eV and E_{ad}= 0.85 eV for CO adsorption on RuTPP and CoTPP, respectively.

4.4.2 Electronic structure: Frontier orbitals

The electronic structure of CO adsorbed on RuTPP and CoTPP was investigated by calculating the projected DOS on the frontier orbitals of the isolated CO molecule. These projected DOS are shown in Figs 4.5 and 4.6 for CO-RuTPP and CO-CoTPP, respectively. Here, the energy levels of CO-MTPP and the isolated CO molecule are referenced with respect to the common vacuum level.

The behaviour of the projected density of states are in agreement with the Blyholder [25] model of CO bonding to a metal. There is an electron donation from the 5σ orbital of the CO molecule to the metal centre from the appearance of states above the Fermi level from the mixing of this orbital with the d_σ states of the metal. The two-fold, degenerate $2\pi^\star$ orbitals of the CO molecule mixes with the d_π states of the metal atom and shifts down in energy with a net electron back donation into the $2\pi^\star$ orbital from the metal atom.

The stronger bonding of CO on RuTPP than on CoTPP is consistent with its stronger mixing of the $2\pi^\star$ and 5σ orbitals with the Ru d states than for the Co d states, which results in a larger splitting in the bonding and anti-bonding combination of the frontier orbitals with the Ru d states than for the Co d states.

Finally, the spin-moment of RuTPP was quenched by the bonding of CO, whereas CoTPP kept its spin moment of $1\mu_B$.

4.5 Adsorption of MTPP on Cu(110)

The DFT calculations of the adsorption of RuTPP on Cu(110) were carried out for three different coverages which include the low coverage p(6x8) structure in order to mimic an isolated RuTPP over Cu(110) and the two high coverage A^δ 4.1 and A^γ 4.2 structures. In the case of the adsorption of CoTPP and ZnTPP on Cu(110), the calculations were only carried out for the high-coverage, A^γ structure.

4.5.1 Adsorption geometries

The calculated equilibrium structures of the RuTPP molecule in the low and high coverage structures on Cu(110) show that the adsorption gives rise to a buckling of the macro cycle and a tilt of the phenyl rings and a change of their orientations with respect to the isolated molecule. Here we assumed the molecule is adsorbed in the same

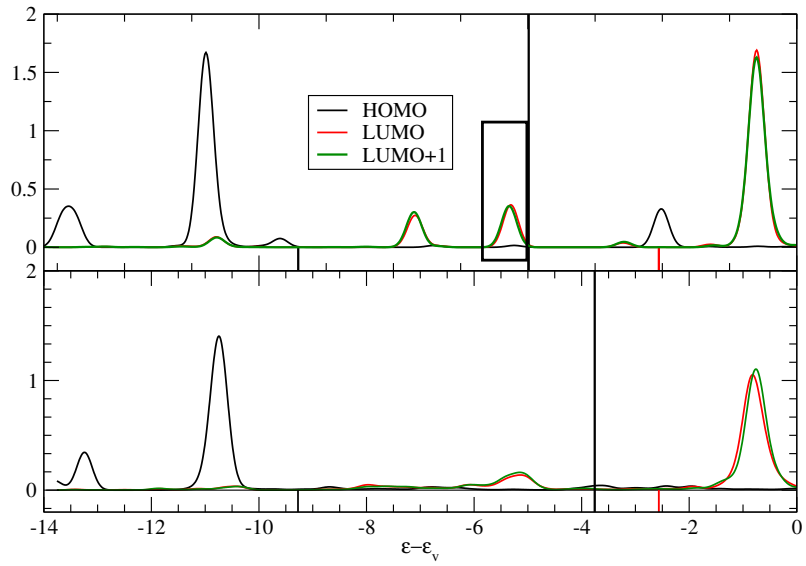

Figure 4.5: Calculated projected density of states of CO-RuTPP (upper panel) and CO-RuTPP/Cu(110) (lower panel) onto frontier orbitals of the isolated CO molecule. The highest occupied molecular orbital (HOMO) of the CO molecule is the 5σ orbital, while the lowest unoccupied orbital (LUMO and LUMO+1) are the two-fold, degenerate 2π* orbitals. The energies of these frontier orbitals are indicated by the vertical bars. The vacuum level of the isolated CO molecule is aligned with the vacuum level of the isolated MTPP molecule. The states was broadened by a Gaussian function with a FWHM of 0.2 eV

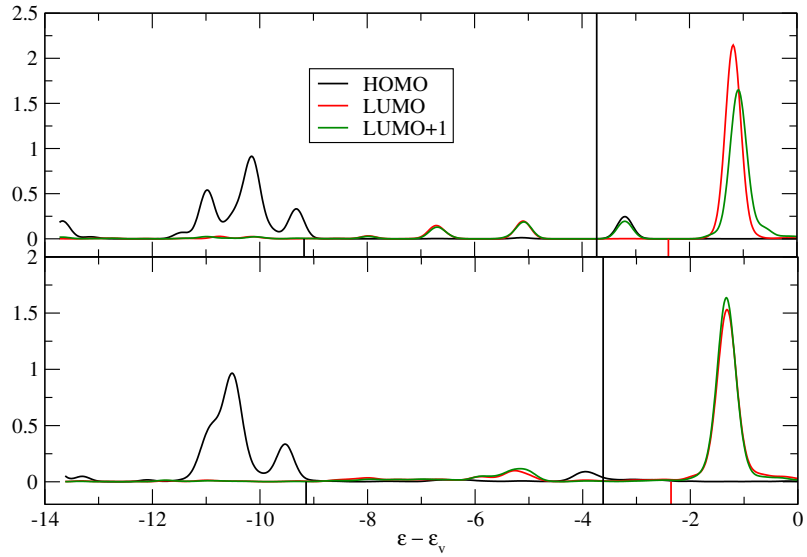

Figure 4.6: Calculated projected density of states of CO-CoTPP (upper panel) and CO-CoTPP/Cu(110) (lower panel) onto frontier orbitals of the isolated CO molecule. The highest occupied molecular orbital (HOMO) of the CO molecule is the 5σ orbital, while the lowest unoccupied orbital (LUMO and LUMO+1) are the two-fold, degenerate 2π* orbitals. The energies of these frontier orbitals are indicated by the vertical bars. The vacuum level of the isolated CO molecule is aligned with the vacuum level of the isolated MTPP molecule. The states was broadened by a Gaussian function with a FWHM of 0.2 eV

adsorption site and orientation as for CoTPP: the short bridge adsorption site with the two molecular axis oriented along the $\langle 001 \rangle$ and $\langle 110 \rangle$ directions of the Cu(110). This adsorption geometry is confirmed by the observed STM images (See, Section 6.4.6. The geometry of the phenyl rings are described by the tilt angle Φ and the twist angle Θ, defined as in Sec. 4.3.1 for the isolated MTPP. These angles are shown in Table 4.3. There is a sizeable tilt of the phenyl rings of $\Phi \approx 15 - 25^{\circ}$ of the adsorbed RuTPP compared to the isolated RuTPP. This tilt increases at the higher coverages. There is also a change in the twist angles upon adsorption. The tilting and twisting of the phenyl groups are very similar for all adsorbed MTPP molecules in the Aγ structure.

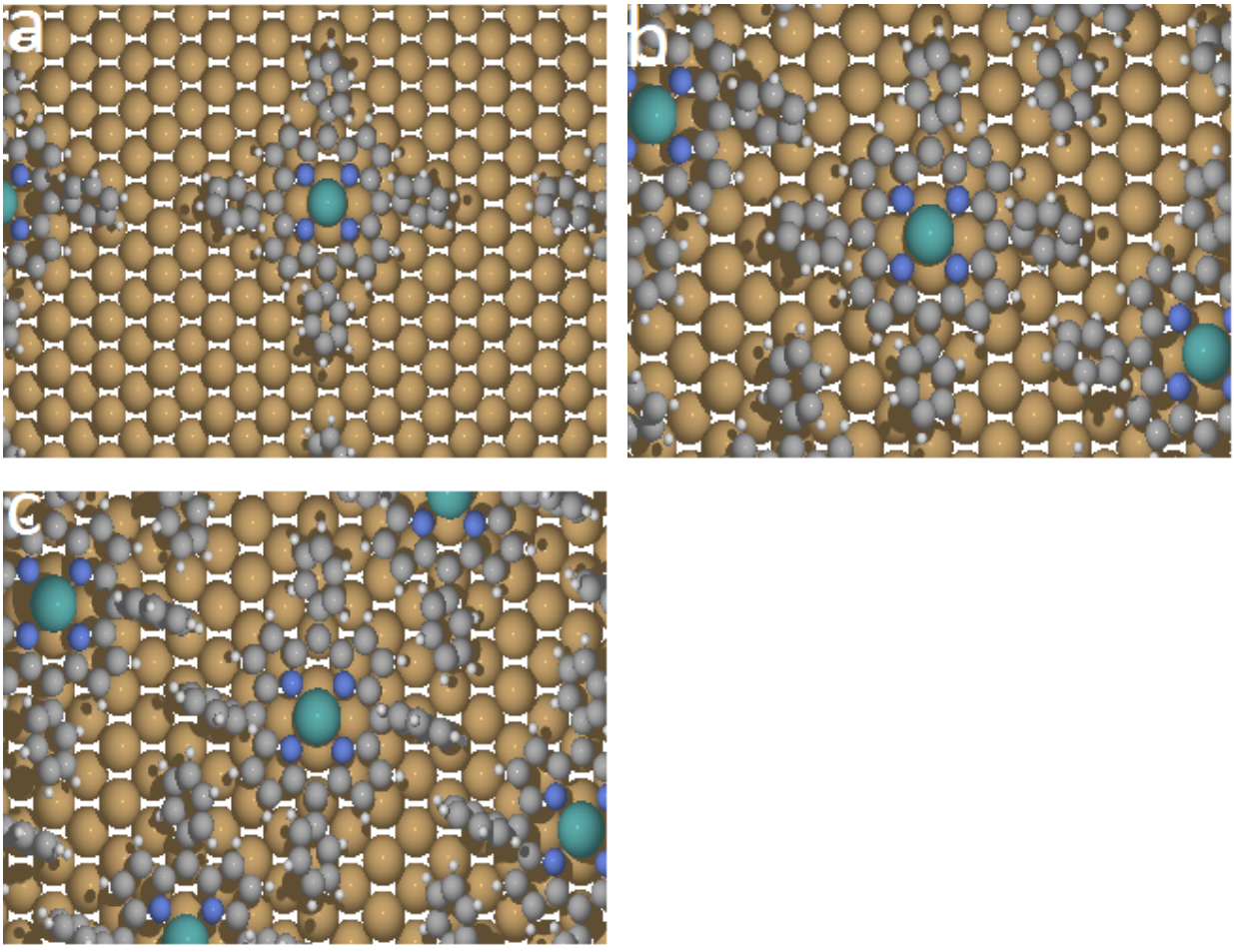

Figure 4.7: Top views of calculated (a) low coverage structure (p(6×8), high coverage structures (b) A^{δ} and (c) A^{γ} of RuTPP on Cu(110).

Structure	Angle	W	E	N	S
		RuTPP(ad)			
p(6×8)	Θ	-53	-56	52	48
	Φ	22	25	18	16
A^{δ}	Θ	-53	-56	49	44
	Φ	23	25	17	14
A^{γ}	Θ	-82	-89	53	54
	Φ	36	36	21	23
		CO-RuTPP(ad)			
A^{γ}	Θ	-81	-86	53	53
	Φ	34	35	19	20
		CoTPP(ad)			
A^{γ}	Θ	-87	-88(88)	61	61
	Φ	37(36)	37(35)	27(26)	28(28)
		CO-CoTPP(ad)			
A^{γ}	Θ	-85	-88	54	54
	Φ	37	36	22	24
		ZnTPP(ad)			
A^{γ}	Θ	-82	-84	54	50
	Φ	35	38	22	21

Table 4.3: Same as in Table 4.2 but for the adsorbed MTPP and CO-MTPP molecules. The values in the parentheses refer to the calculated values in Ref. [31].

Structure	E_{ad} (eV)	$d_{\mathrm{M-Cu}}$ (Å)
RuTPP/Cu(110)		
p(6x8)	7.57	2.50
A^{δ}	7.56	2.465
A^{γ}	7.52	2.48
CO-RuTPP/Cu(110)		
A^{γ}	6.20	2.60
CoTPP/Cu(110)		
A^{γ}	6.61	2.49
CO-CoTPP/Cu(110)		
A^{γ}	6.62	2.53
ZnTPP/Cu(110)		
A^{γ}	5.93	2.51

Table 4.4: Calculated adsorption energies and structural parameters of the MTPP molecules adsorbed on Cu(110). E_{ad} is the adsorption energy of MTPP and CO-MTPP on Cu(110). $d_{\mathrm{M-Cu}}$ is the distance between the the metal core atom and the nearest neighbouring Cu atom.

4.5.2 Adsorption energies

The adsorption energy E_{ad} of MTPP on Cu(110) was calculated for the three different coverages of RuTPP but also for the high coverage structure A^{γ} for M=Co and Zn. Here this energy is defined as,

$$E_{\mathrm{ad}} = E_{\mathrm{MTPP(g)}} + E_{\mathrm{Cu(110)}} - E_{\mathrm{MTPP/Cu(110)}} \, . \tag{4.4}$$

The resulting energies are shown in Table 4.4. The coverage dependence of E_{ad} for RuTPP is weak and the increase of E_{ad} with increasing coverage suggests that there is a weak repulsive interaction between the adsorbed molecules. Furthermore, the calculated E_{ad} for the A^{γ} structure shows that the RuTPP has the strongest interaction with Cu(110) followed by CoTPP and ZnTPP. Note that the relative large magnitudes of E_{ad} are caused by the large contribution from the van der Waals interaction to the molecule-surface interactions for these large molecules.

4.5.3 Electronic structure

As for the isolated MTPP, the electronic structure of the adsorbed MTPP were characterized by the calculated partial DOS of the d partial waves around the metal centre, which are shown in Figs 4.8, 4.9 and 4.10 for M = Ru, Co and Zn, respectively. Since

System	E_{ad} (eV)
CO-RuTPP	2.88
CO-RuTPP/Cu(110)	1.54
CO-CoTPP	0.77
CO-CoTPP/Cu(110)	0.85

Table 4.5: Adsorption energies E_{ad} of CO adsorbed on MTPP and on MTPP/Cu(110)

the spin moments of RuTPP and CoTPP are found to be quenched upon adsorption, the partial DOS are not spin-polarised upon adsorption.

There is a significant broadening and shifts of the d_σ states in the case of the RuTTP upon adsorption due to the interaction with the Cu states but less so for CoTPP. The d_π states of RuTPP and CoTPP show also a broadening upon adsorption but less than for d_σ states. The d_δ (d_{xy} and $d_{x^2-y^2}$) are the least influenced upon adsorption. In the case of the adsorbed ZnTPP, the occupied d states broaden and shift down in energy due to the interaction with the Cu substrate states.

4.6 CO adsorption on MTPP/Cu(110)

The adsorption of CO on RuTPP/Cu(110) and CoTPP/Cu(110) will now be discussed with an emphasis of the effects of the metal centre on the geometric structure, adsorption energies and electronic structure.

4.6.1 Geometric structure

The optimization of the geometric structure of CO for the CO-MTPP/Cu(110) started from different positions and orientations of CO on the metal centre. As for the isolated ZnTPP, CO did not bond to the metal centre of the adsorbed ZnTPP. In the case of CO-RuTPP/Cu(110), only a unique equilibrium position was found, the carbon atom is bonded on-top of the ruthenium Ru atom in a perpendicular orientation of CO with respect to the molecular plane. In the case of CO-CoTPP/Cu(110), two different equilibrium positions of CO were found on top of the Co atom, one where CO was oriented as for CO-RuTPP/Cu(110) and second where CO is tilted with about 21° with respect to the surface normal. The tilted configuration is slightly lower in energy than the perpendicular orientation and was then selected as the optimized configuration. The interatomic C-O distances for the adsorbed complexes were the same as for the isolated ones. Upon adsorption of CO on the adsorbed complexes, the perpendicular M-Cu distances increased by 0.11 and 0.04 Å for M=Ru and Co, respectively. The

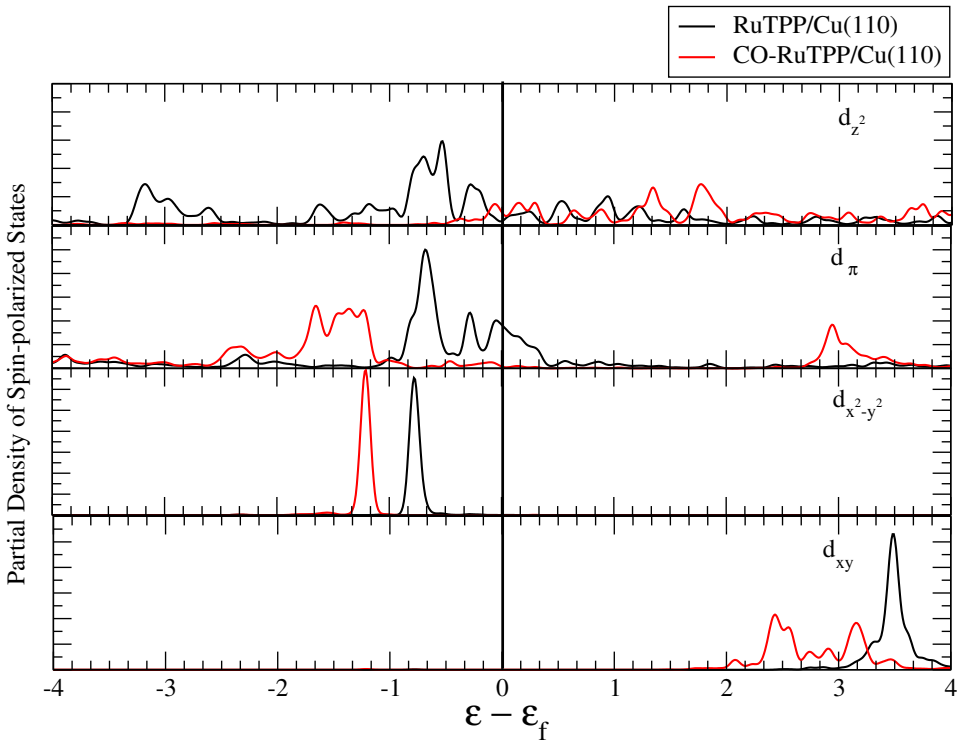

Figure 4.8: Partial DOS of an adsorbed RuTPP and CO-RuTPP molecule for different Ru d partial waves with ($d_\pi = d_{xz} + d_{yz}$). The orientation of the Cartesian axes are defined in Fig. 4.1.

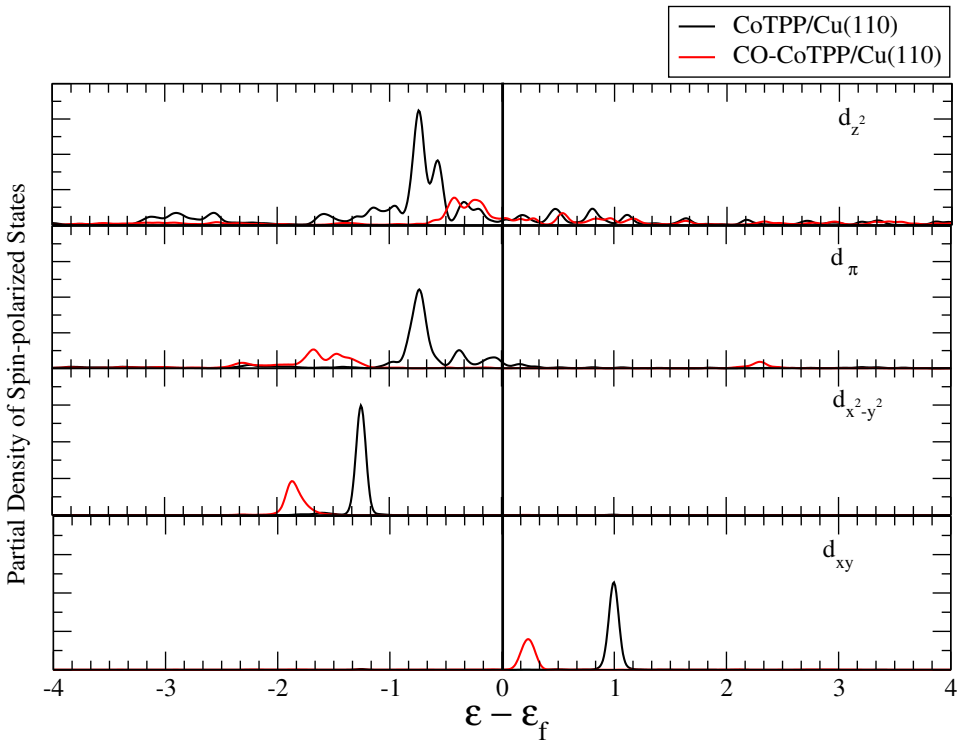

Figure 4.9: Partial DOS of an adsorbed CoTPP and CO-CoTPP molecule for different Co d partial waves with ($d_\pi = d_{xz} + d_{yz}$). The orientation of the Cartesian axes are defined in Fig. 4.1.

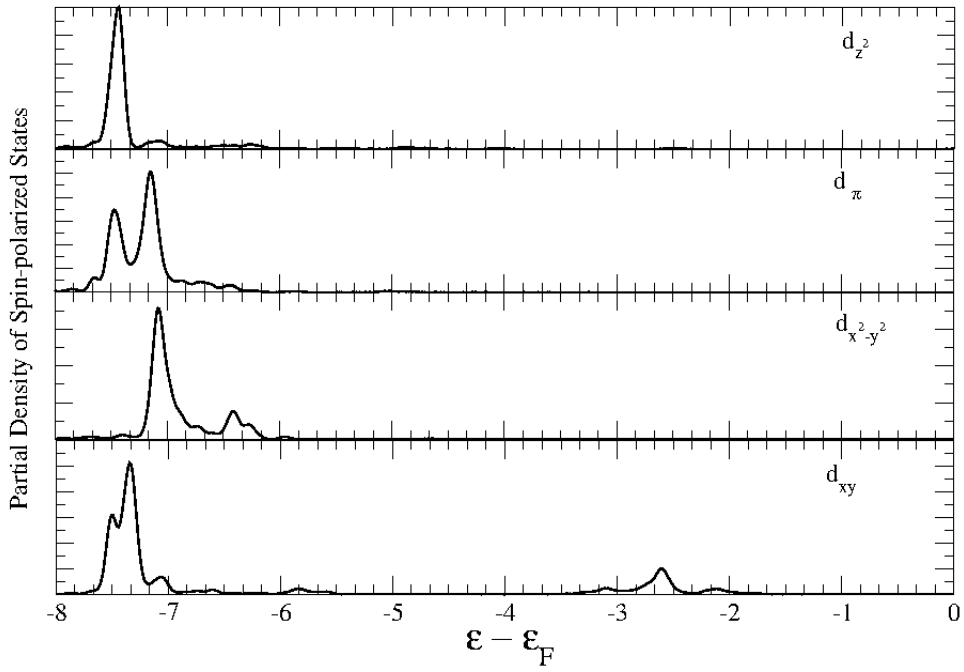

Figure 4.10: Partial DOS of an adsorbed ZnTPP molecule for different Zn d partial waves with ($d_\pi = d_{xz} + d_{yz}$). The orientation of the Cartesian axes are defined in Fig. 4.1.

relatively large decrease of this distance for M=Ru suggests a weakening of the M-Cu bonding.

4.6.2 Adsorption energies

As for the adsorption energy for MTPP on Cu(110), the adsorption energy E_{ad} of CO on MTPP/Cu(110) was defined in a similar manner as in Eq. 4.3,

$$E_{\mathrm{ad}} = E_{\mathrm{MTPP/Cu(110)}} + E_{\mathrm{CO}} - E_{\mathrm{CO-MTPP/Cu(110)}} \,. \tag{4.5}$$

The calculated E_{ad} are shown in Table 4.5. The adsorption energy of CO on the adsorbed RuTPP is substantially smaller than on the isolated RuTPP and is reduced by about 1.3 eV whereas in the case of adsorbed CoTPP, E_{ad} increases by about 0.1 eV compared to the isolated CoTPP. Since E_{ad} = 1.14 eV for CO on the bare surface [89], E_{ad} is sufficiently large for CO on RuTPP so that CO is preferentially adsorbed on the adsorbed RuTPP, whereas E_{ad} for CO on the adsorbed CoTPP is too small for preferential adsorption on the adsorbed CoTPP. The adsorption energy of the CO-RuTPP complex decreases with about 1.3 eV compared to E_{ad} of the RuTPP complex showing that the CO adsorption on the adsorbed RuTPP decreases the molecule-surface bonding strength (see Table 4.5). In contrast, the difference between E_{ad} of CO-CoTPP and CoTPP is very small, only about 0.01 eV, which does not suggest any effect on the bonding of CoTPP on the surface upon adsorption of CO.

4.6.3 Electronic structure: Frontier orbitals

As for the isolated CO-MTPP molecule, the electronic structure of the adsorption of CO on MTPP/Cu(110) was investigated using the projected DOS on the frontier orbitals of the isolated CO molecule but also the partial DOS of the metal centre d partial waves. The projected DOS for M=Ru and M=Co are shown in Figs 4.5 and 4.6, respectively, and the partial DOS are shown in Figs 4.8 and 4.9, respectively,

In the calculated projected DOS for isolated and adsorbed CO-MTPP, there are minor shifts and broadenings of the major peaks due to the 5σ and the $2\pi^*$ orbitals upon adsorption of RuTPP and CoTPP. The most notable differences between the projected DOS of CO-MTPP and adsorbed CO-MTPP is the disappearance of one unoccupied minor peak due to 5σ and one occupied minor peak due to $2\pi^*$.

The change in the calculated partial DOS upon adsorption of CO on MTPP/Cu(110) show that the d_σ states shifts up in energy due to the interaction with the 5σ states and becomes partially occupied whereas the d_π states shifts down in energy due to the interaction with $2\pi^*$ states. The behaviour is in accordance with the Blyholder model. There is also downward shifts of the d_δ states but these are not simply due to a mixing

with the $2\pi^*$ states at least for the $d_{x^2-y^2}$ states since no $2\pi^*$ peak appear around 3 eV as for the d_π states.

4.6.4 STM images

The calculated structures of the adsorbed RuTPP at the different coverages and of CO-RuTPP are corroborated by a comparison between calculated and experimental STM images. These topographical images were calculated at a sample bias of 0.5 eV and an average tip height of 10.7 Å and are shown in Fig. 4.12. The recorded topographical, STM images of the adsorbed RuTPP and CO-RuTPP are shown in Fig. 4.13. Note that the underlying Cu surface lattice was identified by using adsorbed CO molecules, which adsorb in the top site, as markers. This identification enables the determination of the adsorption site of the RuTPP molecules to be the short bridge site.

The calculated images of adsorbed RuTPP have quite different appearances with coverage but a common and characteristic feature is the protrusions from the phenyl rings. In the case of the adsorbed CO-RuTPP, the CO molecule show up as a strong protrusion in the centre of the molecule, which should make it possible to distinguish between adsorbed RuTPP and CO-RuTPP.

At the lowest calculated coverage, p(6x8), (Fig. 4.12) the calculated STM image shows four protrusions or lobes from the phenyl groups with the lobes along <001> direction being somewhat brighter than the lobes along the <110> direction but also a strong protrusion in the centre. The four lobes are clearly observed in the experiments for the isolated molecule (Fig. 4.13(a)) and are also oriented in the same way with respect to the underlying Cu lattice but with no strong protrusion in the centre of the molecule. In the high coverage structures, the strong protrusion in the centre disappears and there are only protrusions from the phenyl groups which appear differently in the two different high-coverage structures due to the different twists and tilts of the phenyl groups and also the different relative arrangement of the phenyl groups of neighbouring molecules. At the highest coverage corresponding to the A^γ structure, the protrusions line up in agreement with the observed STM image in Fig. 4.13(a). Some of the molecules in the observed image show a protrusion in the centre of the molecule which then corresponds to CO-RuTPP molecules.

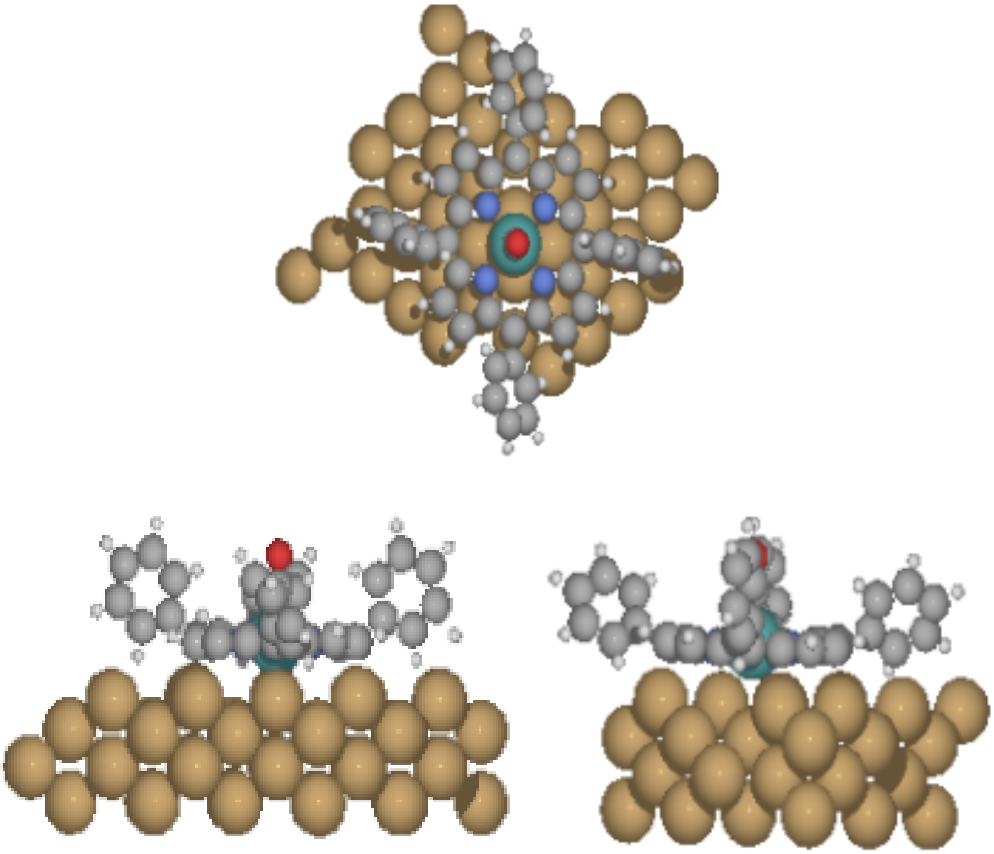

Figure 4.11: Top and side views of calculated structure of CO-RuTPP/Cu(110).

4.7 Comparison with STS data of adsorbed RuTPP and CO-RuTPP

Here we attempt to use our calculated partial DOS of the adsorbed RuTPP and CO-RuTPP on Cu(110) to relate adsorbate-induced states with observed peaks in spectra recorded by scanning tunnelling spectroscopy (STS). This study has been published as a part of a study of CO desorption from adsorbed CO-RuTPP induced by inelastic electron tunnelling [90]. Note that the interpretation of STS in terms of one-electron DOS is challenging, because in STS the electrons are either removed or added to the system, which in principle cannot be reproduced accurately by the calculated Kohn-Sham states.

Figure 4.14 shows STS spectra from the centre of RuTPP and CO-RuTPP after subtracting the reference signal from a bare Cu(110) surface. Due to the strongly nonlinear dependence of signal at high bias voltages, a reliable difference spectrum could only be obtained in the bias range of -1.3 to +0.9 V. The spectrum of RuTPP exhibits an increase in the differential tunnelling conductance, $\frac{dI}{dV}$, at a negative sample bias V. A

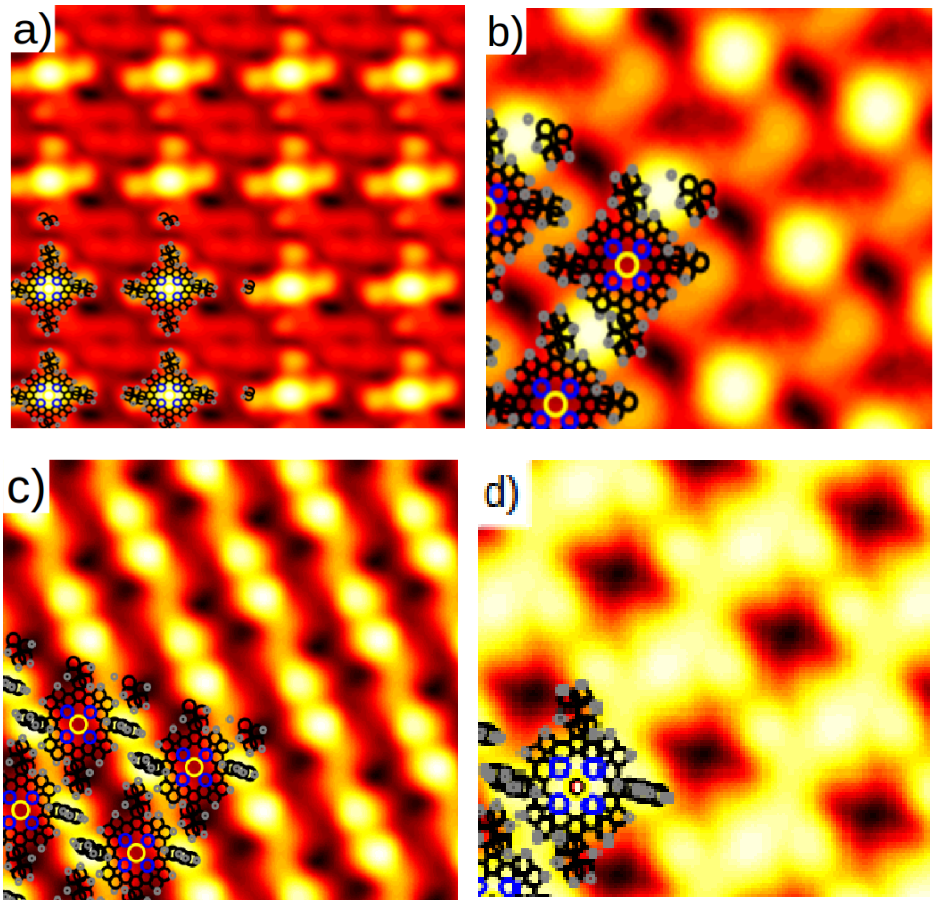

Figure 4.12: Calculated, topographical STM images of RuTPP/Cu(110) in the (a) the p(6x8), (b) A^{δ} and (c) A^{γ} structures and of (d) CO-RuTPP/Cu(110) in the A^{γ} structure. The sample bias is 0.5 V except 1.0 V in (d) and the average heights from the outermost Cu surface plane are (a) 10.8 Å, (b) 10.6 Å, (c) 10.7 Å, (d) 10.8 Å.

distinct peak at around V = -1.1 V was observed from both RuTPP (peak a') and CO-RuTPP (peak a). Such peaks that are derived from adsorbate-induced occupied states have been widely observed for metalloporphyrins on metal surfaces [**14**], for example, the STS spectrum of CoTPP on Cu(110) reveals a peak at V = -0.72 V, which was assigned to the highest occupied molecular orbital (HOMO) of adsorbed CoTPP [**14**]. The peak at V = - 1.1 V was assigned to the HOMO of RuTPP and note that it is not shifted by subsequent CO adsorption. The most prominent peak introduced by the CO adsorption is the peak at around the Fermi level, ϵ_F, (peak c), but there also seems to be a more pronounced shoulder at V = 0.8 V (peak b) than that of adsorbed RuTPP.

In our attempt to link the observed peaks in the STS spectra to adsorbate- induced electronic states, we have used our calculated PDOS of RuTPP/Cu(110) with and without adsorbed CO shown in Fig 4.2 but have also used the calculated PDOS of

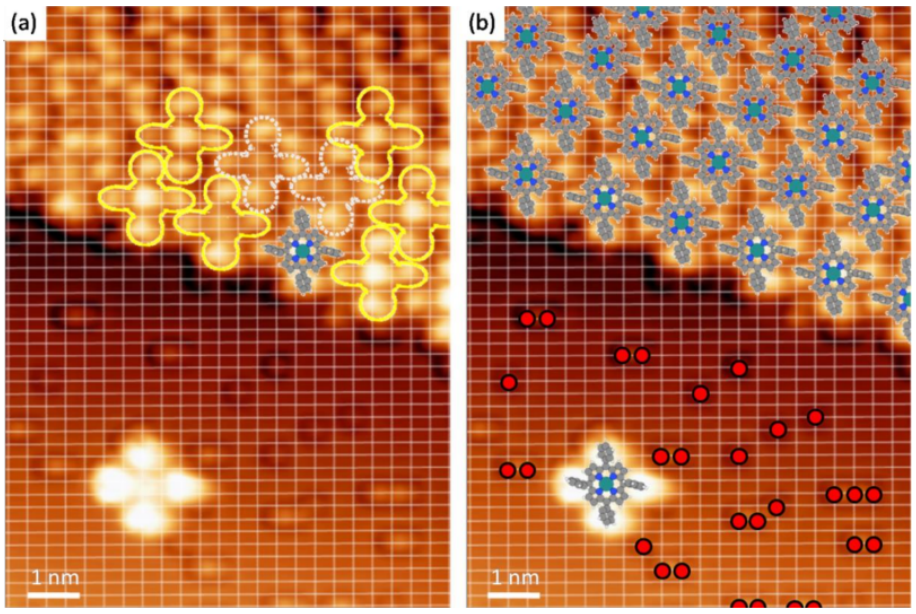

Figure 4.13: (a) Experimental, topographical STM images of RuTPP and CO-RuTPP on Cu(110), The underlying Cu lattice (white lines) were determined by using CO molecules, which are adsorbed in a top site, as markers. The STM images were recorded at University of Liverpool by Omiya and coworkers [86]. V = 0.5 V and I_t=0.5 nA at T = 4.7 K.

p_z character around all C atoms shown in Fig. 4.15, corresponding essentially to Cπ states. In addition, we have also calculated the local density of states (LDOS) at the position of the tip apex and are shown in Fig. 4.16.

As discussed in Sections 4.4.2 and 4.6.3, the changes in the PDOS upon CO adsorption, relate to the formation of a π bond of the unoccupied CO $2\pi^*$ with Ru d_π (forming bonding and anti bonding states) and a σ bond of the occupied CO 5 σ with Ru d_σ. As a result the d_σ and d_π states in the energy region below the Fermi level, ϵ_F shift up and down in energy, respectively, whereas the downward shift of the d_δ state in this region is not simply due to mixing with CO states. This latter state is not expected to contribute to the LDOS at the tip apex due to its high azimuthal angular momentum ($|m_l|$ = 2) as demonstrated by the calculated LDOS in Fig. 4.16). The behaviour of the double peak around -1 V in the STS upon CO adsorption is not easily reconciled by the behaviour of the corresponding peaks in the PDOS of d_π character. However, the CO-induced peak in the STS around ϵ_F can be reconciled with the calculated PDOS of d_σ and Cπ, and LDOS in Fig. 4.16.

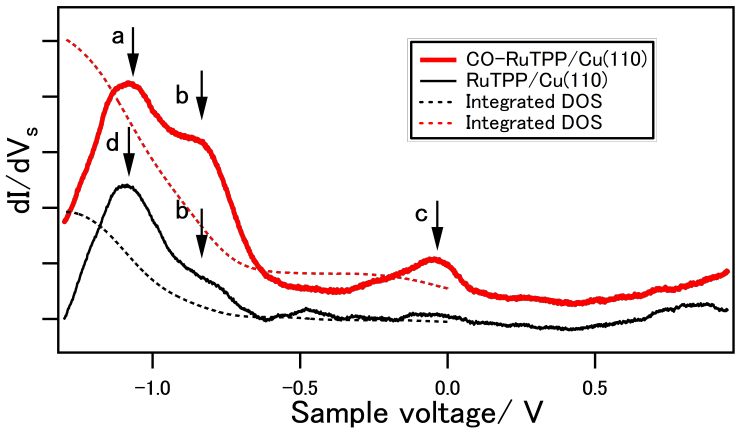

Figure 4.14: Scanning tunnelling spectra of CO-RuTPP (red lines) and RuTPP (black lines) adsorbed on a Cu(110) surface. The spectrum of the bare Cu(110) is subtracted to emphasis the change in $\frac{dI}{dV}$. Dotted lines show the integrated STS signal from the Fermi level. Major peaks are labelled (a-c). This figure corresponds to Fig. 2(a) in ref. [86].

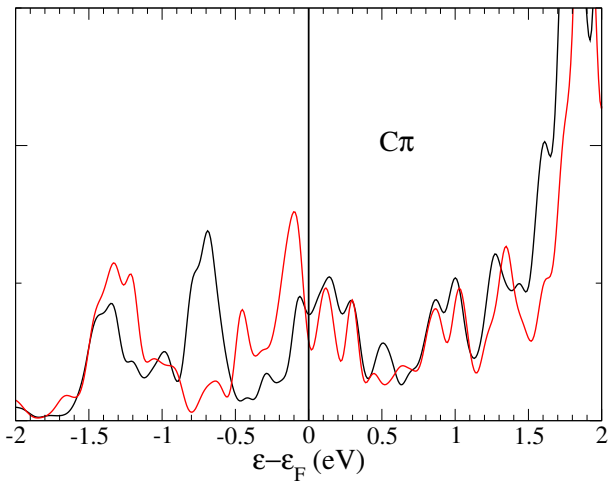

Figure 4.15: Calculated partial DOS of p_z character around all C atoms (Cπ) of RuTPP (black line) and CO-RuTPP (red line) adsorbed on Cu(110).

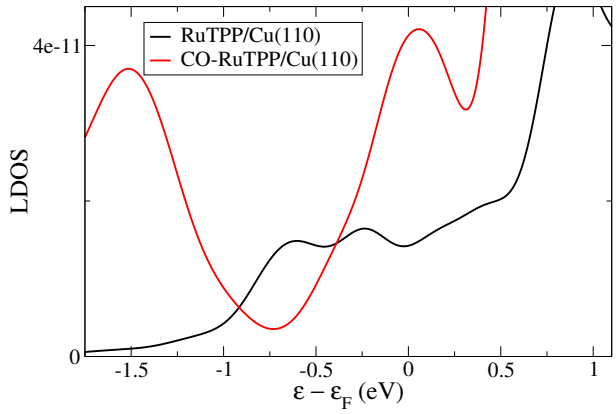

Figure 4.16: Calculated local density of states (LDOS) at 9.15 Å above the Cu surface layer at the centre of RuTPP (black line) and CO-RuTPP (red line) adsorbed on Cu(110).

4.8 Summary

In this Chapter, we have presented results from density functional theory (DFT) calculations of the adsorption of some metalloporphyrins MTPP (M = Ru, Co and Zn) in the gas-phase and adsorbed on Cu(110) for some different coverages and also the coordination of CO on these metalloporphyrins. The emphasis has been on the adsorption of porphyrins with a Ru metal centre.

In the gas-phase, the macro cycle is planar but the phenyl rings of MTPP and CO-MTPP are twisted due to steric constraints. Upon adsorption in the experimentally determined short bridge site the phenyl rings tilt away from the surface.

The CO molecule bonds with the C atom to the Ru and Co metal centres but not to the Zn metal centre due to its closed d shell. The CO molecule is bonded perpendicular to the macro cycle of RuTPP but slightly tilted on CoTPP. The CO adsorption energy 2.9 eV is very large on RuTPP compared to its value of 0.8 eV on CoTPP. This energy is reduced with almost 50 % when RuTPP is adsorbed, whereas it changes only slightly when CoTPP is adsorbed. The CO adsorption energy on the bare surface is in between its values for CoTPP and RuTPP, which explains why CO adsorbs readily on the adsorbed RuTPP but not on CoTPP. This large difference between the CO adsorption energies for these two metal centres is not readily rationalized from an analysis of the calculated electronic structures based on partial density of states (PDOS). However, the PDOS show that the CO bonding to the metal centres is in accordance with the Blyholder model.

The calculated STM images exhibit characteristic protrusions from the tilted phenyl groups and are in reasonable agreement with the observed images. The adsorbed CO-

MTPP and MTPP molecules are readily discriminated by a characteristic protrusion in the centre of the molecule from the adsorbed CO molecule. The observed scanning tunnelling spectra of the adsorbed RuTPP and CO-RuTPP molecules cannot be easily rationalized by the calculated electronic structure but a CO-induced peak in the observed spectrum can be reconciled with the calculated electronic structure.

Chapter 5

Anharmonicity of Carbon monoxide complexes

5.1 Introduction

In this chapter, we present a DFT study of the anharmonicity of the internal C-O stretch of CO in various CO complexes. This study is motivated by recent second harmonic frequency generation (SFG) experiments of the fundamental and overtone frequencies of CO and CO-RuTPP adsorbed on Cu(110) by the local experimental group headed by Arnolds [7]. The anharmonicity manifested itself by the first overtone frequency being smaller than the fundamental frequency. In particular, they found in their analysis of the observed vibrational frequencies using a Morse potential for the potential energy curve (PEC) a surprisingly large value for the anharmonicity of the C-O stretch of CO-RuTPP adsorbed on Cu(110) as compared to CO adsorbed on Cu(110) and also for other CO complexes studied by other groups. This observation raises the question about the origin of this large value for anharmonicity, for instance, whether it is due to an unusual bonding of CO on RuTPP adsorbed on Cu(110).

This question is addressed here by performing systematic calculations of the potential energy curves of the internal C-O stretch for CO-RuTPP in the gas phase and adsorbed on Cu(110). Our methodology is assessed by calculating the corresponding potential energy curve for CO in the gas phase and make a comparison with experimental data. In addition, we have also studied CO-CoTPP in the gas phase and adsorbed on Cu(110). The anharmonicity was determined by a Morse and a polynomial potential fit to the calculated potential energy curve and the result was compared to the anharmonicity parameter determined by a fit to vibrational frequencies of a Morse potential [91] to the observed frequencies of the fundamental and the first overtone of the C-O stretch mode.

In SFG, the overtones of the C-O stretch mode was probed by populating the vibrational modes by a broad band IR pump pulse followed by a probe beam in the visible. The overtones or hot band transitions then show up as resonances at the sum frequency of the probe beam and the overtone frequencies.

A characteristic SFG spectra of the CO stretch mode in CO-RuTPP adsorbed on Cu(110) is shown in Fig. 5.1. The first overtone shows up at a frequency of $\nu(1 \rightarrow 2)$ = 1926 cm^{-1} just below the fundamental frequency of $\nu(0 \rightarrow 1)$ = 1957 cm^{-1} and its intensity increases with the energy of the pump pulse. The peak at 1987 cm^{-1} corresponds to the fundamental C-O stretch mode of CO adsorbed on Cu(110). In order to extract the anharmonicity from the measured vibrational frequencies of the internal CO stretch of the adsorbed molecules it is necessary to work at sufficiently small coverages so that a localised two-phonon state is formed on a single molecule and the measured frequencies correspond to singleton frequencies [92]. At higher coverages, vibration coupling, such as the dipole-dipole coupling, between the vibrations start to localise this two-phonon state and gives rise a coverage-dependent dynamical shift of the overtone frequency towards the vibrational frequency of the fundamental mode. In addition, there will also be a coverage-dependent shift of the vibrational frequency of the fundamental from the dipole-dipole coupling but also a chemical shift from adsorbate-adsorbate interactions.

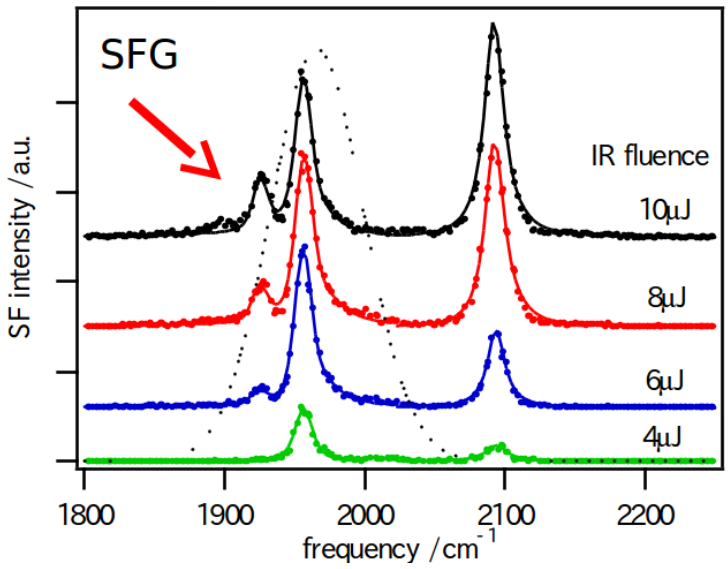

Figure 5.1: SFG spectra of the C-O stretch mode of CO-RuTPP/Cu(110). The figure is taken from T. Omiya thesis [86]

There have only been a few previous works on the calculations of the anharmonicity of the internal stretch mode of CO adsorbed on various metal surfaces [85, 93].

The paper by Dabo [93] studied the correlation between the calculated equilibrium distance and the harmonic frequency of the internal CO stretch and finds moderate deviations from Badger's rule. This rule assumes that the anharmonicity of the internal CO stretch mode is conserved upon adsorption (*i.e.* the corresponding PECs differ only by a linear term in the displacement), which was supported by their calculations for CO adsorbed on a Pt surface. The paper by Loffreda and coworkers [85] calculated the effect of the anharmonicity on the fundamental frequency of the internal stretch mode of CO adsorbed on Pt(111) for different surface coverages. These frequencies were obtained by fitting a Morse potential to the calculated PECs.

5.2 Computational details

The potential energy curves of the CO stretch in different CO complexes were obtained from periodic density functional theory calculations using the plane-wave code VASP, [81], [82]. The electron-ion core interactions were handled using the projector augmented wave (PAW) method [83], [84]. The exchange correlation effects were handled in most cases by using the optB86b-vdW approximation [69] which includes van der Waals interactions except in a few cases the PBE approximation [94] was used. A super cell with the size 10x10x10 Å^3 was used for the isolated CO and only the Γ-point in the BZ was sampled. For CO adsorbed on Cu(110), the surface unit cells of the super cell corresponded to p(1x2), p(2x4) and p(3x6) structures and the BZs were sampled by 12x12x1, 6x6x1 and 3x3x1 k-point grids, respectively, and the plane-wave cut-off was 400 eV. The Cu(110) slab included six Cu layers and a vacuum region of 19.6 Å, similar parameters chosen by Loffreda and Dabo [85], [93] Dipole corrections were included in the perpendicular direction. As suggested by experiments for CO adsorption on Cu(110) [26], the top adsorption site of was chosen in the calculations. The two bottom layers were frozen at the experimental value 3.634 Å for the bulk lattice distance of Cu the geometrical optimization. The super cells and the DFT parameters for the isolated CO-RuTPP and CO-CoTPP complexes and their A^γ structures on Cu(110) were kept the same as in chapter 4.

The potential energies curves were obtained by changing the carbon-oxygen inter-atomic distance with a step size of 0.01 Å. The range of inter-atomic distances of about 1.03 to 1.33 Å was chosen such that the maximum potential energy is about 0.8 eV above the potential energy at the equilibrium position. This values for the maximum potential energy was chosen to be larger the energy of about 0.625 eV of the first excited vibrational state ($n = 2$) obtained in the harmonic approximation from the calculated force constant. The parameters of the Morse and the quartic potential

parameters were obtained by a non-linear least square fit of these potentials to the calculated potential energy points using the python script optimize.curve_fit in the SciPy package [95].

The vibrational energies of the internal CO stretch and the CO molecule stretch were also calculated in the harmonic approximation. The dynamical matrix was also obtained by calculating the central differences of the forces obtained by making small symmetric displacements of 0.02 Å of the C, O and the coordinated metal atom in the C-O bond direction. This calculation was accomplished using the atomic simulation package (ASE) [96]. The effective charges of the C-O stretch were obtained from the slopes of the calculated dipole moments with respect to the C-O stretch coordinate.

5.3 C-O stretch potential energy curve

The calculated potential energy curve of the C-O stretch was calculated by keeping the centre-of-mass of the C and O atoms fixed. This approximation is based on the assumption that the CO-M stretch has a negligible vibrational energy compared to vibrational energy of the C-O stretch. This approximation has been tested by using the proper displacements C and O atoms when including the centre-of-mass motion and the motion of the coordinated metal atom M, which was done in the following manner.

An eigen-vector ξ_i of the C-O stretch mode was first obtained from the calculated dynamical matrix for the perpendicular motion of the C, O and M atoms, corresponding to atom indices i = C, O and M, respectively. The atomic displacements u_i of this mode as a function of the internal stretch coordinate r were then defined as,

$$u_i = (r - r_0)e_i, i = \mathrm{C, O \text{ and } M} \tag{5.1}$$

where r_0 is the equilibrium position and

$$e_i = \frac{m_i^{-1/2}\xi_i}{m_O^{-1/2}\xi_O - m_C^{-1/2}\xi_C}, i = \mathrm{C, O \text{ and } M} \tag{5.2}$$

where m_i is the mass of atom i. This definition ensures that $r = u_O - u_c$. From the kinetic energy of the stretch coordinate r, one obtains that the associated effective mass m_{eff} is given by,

$$m_{\mathrm{eff}} = \sum_i m_i e_i^2 \tag{5.3}$$

where m_i is the mass of atom i. Note that in the high frequency limit of the internal stretch mode, $\xi_O = \sqrt{m_c}$, $\xi_C = -\sqrt{m_O}$ and $\xi_M = 0$ which gives $e_O = m_c/(m_C + m_O)$,

$e_C = -m_O/(m_C + m_O)$ and $e_M = 0$ and the centre-of-mass is fixed and m_{eff} is equal to the reduced mass of C and O.

Another consideration when calculating the potential energy curve of the C-O stretch is the effect of adsorbate-adsorbate interactions and the associated coverage dependence of the potential energy curve for the ordered structures of adsorbed CO molecules. Here this curve was calculated for the in-phase stretching of the C-O bond corresponding to the Γ-point in the surface Brillouin zone. The calculated vibrational frequency of the fundamental mode can then be directly compared with measured energies in RAIRS and SFG.

5.4 Model potential description of anharmonicity

The anharmonicity of the internal CO stretch was studied by fitting a Morse potential $V_M(r)$ and a polynomial potential $V_Q(r)$, including quadratic, ternary and quartic terms, to the calculated potential energy curve (PEC). The Morse potential is a bit restrictive since the potential shape only depends on two parameters and the harmonic and anharmonic part cannot be varied independently. In contrast, the potential shape of the quartic potentials depends on three parameters and the harmonic and anharmonic parts of the potential can be separated. However, the Morse potential gives a physically transparent description of the whole potential energy curve with an analytical expression for the energy levels. There is no such analytical expression for the energy levels of $V_Q(r)$ but they are obtained here by leading order perturbation theory, which should be appropriate for the weak anharmonicity of the C-O stretch.

The Morse potential is given by [97], [91]

$$V_M(r) = V_0 + D_e(\exp(-2\alpha(r - r_0)) - 2\exp(-\alpha(r - r_0)) + 1)\ , \tag{5.4}$$

where r is the inter-atomic distance. The dissociation energy D_e and the repulsive exponent α determines the potential shape and r_0 and V_0 is the equilibrium position and energy, respectively. The analytical expression of the energy eigenvalues $E(n)$ of the different eigen-states n =1, 2, 3 with respect to the potential energy minimum of $V_M(r)$ is given by [91],

$$E(n) = h\nu_0(n + \frac{1}{2})\left(1 - \chi(n + \frac{1}{2})\right). \tag{5.5}$$

Here

$$\nu_0 = \frac{a}{2\pi}\sqrt{2D_e/\mu} \tag{5.6}$$

is the vibrational frequency of the Morse potential in the harmonic approximation, where μ is the reduced mass. The anharmonicity parameter, χ, is determined by the

ratio between the vibrational energy in the harmonic approximation and the dissociation energy as,

$$\chi = \frac{h\nu_0}{4D_e}. \tag{5.7}$$

The vibrational frequencies of the fundamental, ($0 \rightarrow 1$), and the overtones, ($n \neq 0 \rightarrow n+1$)), in the Morse potential are now according to Eq. 5.5 given by,

$$\nu_{n\rightarrow n+1} = \nu_0 \left(1 - 2\chi(n+1)\right). \tag{5.8}$$

Note that a characteristic feature of the Morse potential is the constancy of the red shift between consecutive vibrational energies, which is given by,

$$\Delta\Delta\nu = \nu_{n\rightarrow n+1} - \nu_{n-1\rightarrow n} = -2\chi\nu_0. \tag{5.9}$$

This expression can be used to determine the Morse potential parameters from the measured vibrational frequencies of the fundamental and the first overtone. The harmonic vibrational frequency is then given by

$$\nu_0 = 2\nu_{0\rightarrow 1} - \nu_{1\rightarrow 2} \tag{5.10}$$

and the anharmonicity parameter is given by,

$$\chi = \frac{(\nu_{0\rightarrow 1} - \nu_{1\rightarrow 2})}{2(2\nu_{0\rightarrow 1} - \nu_{1\rightarrow 2})} \tag{5.11}$$

The dissociation energy D_e is then obtained from Eqns. 5.7, 5.10, and 5.11 as,

$$D_e = h\frac{(2\nu_{0\rightarrow 1} - \nu_{1\rightarrow 2})^2}{2\nu_{0\rightarrow 1} - 2\nu_{1\rightarrow 2}}. \tag{5.12}$$

The Morse potential parameters for isolated CO and adsorbed on Cu(110) and CO-RuTPP adsorbed on Cu(110), as obtained from the measured vibrational frequencies are shown in table 5.4.

The anharmonicity of the potential energy curve has also been studied by a fit to a polynomial potential $V_Q(r)$ including harmonic and anharmonic terms up to the quartic terms in the displacement $r - r_0$ from the equilibrium position r_0. This potential, which henceforth is referred to as the quartic potential, has the form,

$$V_Q(r) = V_0 + \frac{k}{2}(r - r_0)^2 + k_3(r - r_0)^3 + k_4(r - r_0)^4, \tag{5.13}$$

where the potential shape is determined by the harmonic force constant k and the constant k_3, and k_4 of the cubic and quartic terms, respectively, and is the equilibrium energy, respectively. A Taylor expansion of the Morse potential gives the following constraint between the quadratic, cubic and quartic terms,

$$k_3 = \frac{6k_4k}{7}. \tag{5.14}$$

	χ (%)	$\bar{\nu}_0$ (cm^{-1})	D_e (eV)	Θ (ML)
CO[(a)]	0.61	2169.8	11.2	—
CO/Cu(110)[(b)]	0.63	2114	10.5	0.01
CO-RuTPP/Cu(110)[(c)]	0.76	1987	7.90	0.025

Table 5.1: Anharmonicity χ, harmonic vibrational frequencies $\bar{\nu}_0$, and dissociation energy D_e for the internal stretch of CO in various bonding situations as obtained from a fit of a Morse potential to the observed vibrational frequencies for the fundamental and the first overtone using Eqns. (5.10,5.11,5.12). The coverages Θ at which the measurements were taken are also indicated. Ref. [98] [(b)] Ref. [98] [(c)], Ref. [86] in the A^γ structure.

The eigen-energies of $V_Q(r)$ can be obtained using leading-order perturbation theory in the cubic and quartic terms as,

$$E(n) = V_0 + h\nu_0(n+\frac{1}{2}) + k_3^2 \sum_{m\neq n} \frac{|\langle n|(r-r_0)^3|m\rangle|^2}{(n-m)h\nu_0} + k_4\langle n|(r-r_0)^4|n\rangle, \qquad (5.15)$$

where $|n\rangle$ is an eigen-state of the harmonic part of the potential with eigen-energy $h\nu_0(n+\frac{1}{2})$ and $\nu_0 = \frac{1}{2\pi}\sqrt{\frac{k}{\mu}}$ is the harmonic frequency. The matrix elements of the cubic and quartic terms in Eq. (5.15) can be evaluated analytically and one obtains,

$$\sum_{m\neq n} \frac{|\langle n|(r-r_0)^3|m\rangle|^2}{(n-m)} = -30\left((n+\frac{1}{2})^2 + \frac{7}{60}\right)\delta r^6 \qquad (5.16)$$

$$\langle n|(r-r_0)^4|n\rangle = 6\left((n+\frac{1}{2})^2 + \frac{1}{4}\right)\delta r^4 \qquad (5.17)$$

where

$$\delta r^2 = \langle 0|(r-r_0)^2|1\rangle = \frac{\hbar}{4\pi\mu\nu_0}\,, \qquad (5.18)$$

is mean square vibrational displacement. Inserting these expressions in Eq. (5.15), one obtains a similar form $E(n)$ with respect to the potential energy minimum as for the Morse potential,

$$E(n) = h\nu_0\left(\varphi + (n+\frac{1}{2}) - \tilde{\chi}(n+\frac{1}{2})^2\right), \qquad (5.19)$$

where

$$\varphi = -\frac{7k_3^2 h\nu_0}{16k^3} + \frac{3k_4 h\nu_0}{8k^2} \qquad (5.20)$$

$$\tilde{\chi} = -\frac{15k_3^2 h\nu_0}{4k^3} + \frac{3k_4 h\nu_0}{2k^2} \qquad (5.21)$$

In particular, when the Morse condition in Eq(5.14) is fulfilled, $E(n)$ in Eq.(5.19) reduces to Morse vibrational energies in Eq.(5.5) with $\tilde{\chi} = \chi$ and $\varphi = 0$. Note that

Eq. (5.21) is a perturbative result which breaks down for large n. The vibrational frequencies are then given by,

$$\nu_{n\to n+1} = \nu_0 \left(1 - 2\tilde{\chi}(n+1)\right) \ , \tag{5.22}$$

which has the same linear dependence on n as for the Morse potential in Eq. (5.8). Thus $\tilde{\chi}$ is then an anharmonicity parameter that can be compared directly with χ obtained either by a fit from a Morse potential, Eq. (5.7) or a from experimental vibrational frequencies, Eq. (5.11).

The calculated potential energy curves (PEC) and the fitted Morse and quartic potential curves for the CO in various bonding situations are shown in Fig. 5.2. The corresponding Morse and quartic potential parameters and anharmonicity parameters are shown in table 5.3 and table 5.4, respectively.

5.5 Results and Discussion

5.5.1 CO in the gas-phase

A crucial test of the ability of DFT calculations to determine the anharmonicity of the internal CO stretch in various CO complexes is the isolated CO molecule. As shown in Fig. 5.2, the fits of the Morse and quartic potentials to the calculated PEC is excellent the error σ in the overall fit of the Morse potential to the calculated potential energy curves are very small both for PBE and optB86b-vdW (table 5.3 and 5.4). Furthermore, the calculated value of χ=0.65% is the same for both functionals and is in relatively good agreement with the value of 0.61% obtained from the observed vibrational frequencies in table 5.1. A similar good agreement is obtained between the harmonic vibrational energy and dissociation energy obtained from a fit of the calculated PEC to the Morse potential (5.3) and the corresponding experimental values obtained from vibrational frequencies (5.6). Note that values for D_e as obtained from this fit and the vibrational frequencies, actually underestimates somewhat the calculated and the measured dissociation energy of 11.9 and 11.4 eV [99], respectively, which shows that the overall potential shape deviates somewhat from a Morse potential. The fit of the quartic potential to the calculated PEC gives essentially the same error for the overall fit as for the Morse potential and the same values for the harmonic vibrational frequencies. However, the fact that $\tilde{\chi}$=0.71% is a bit larger than χ=0.65% is a shortcoming of the perturbative results for the vibrational frequencies. Thus, the DFT calculations of the anharmonicity give an encouraging agreement with experiments.

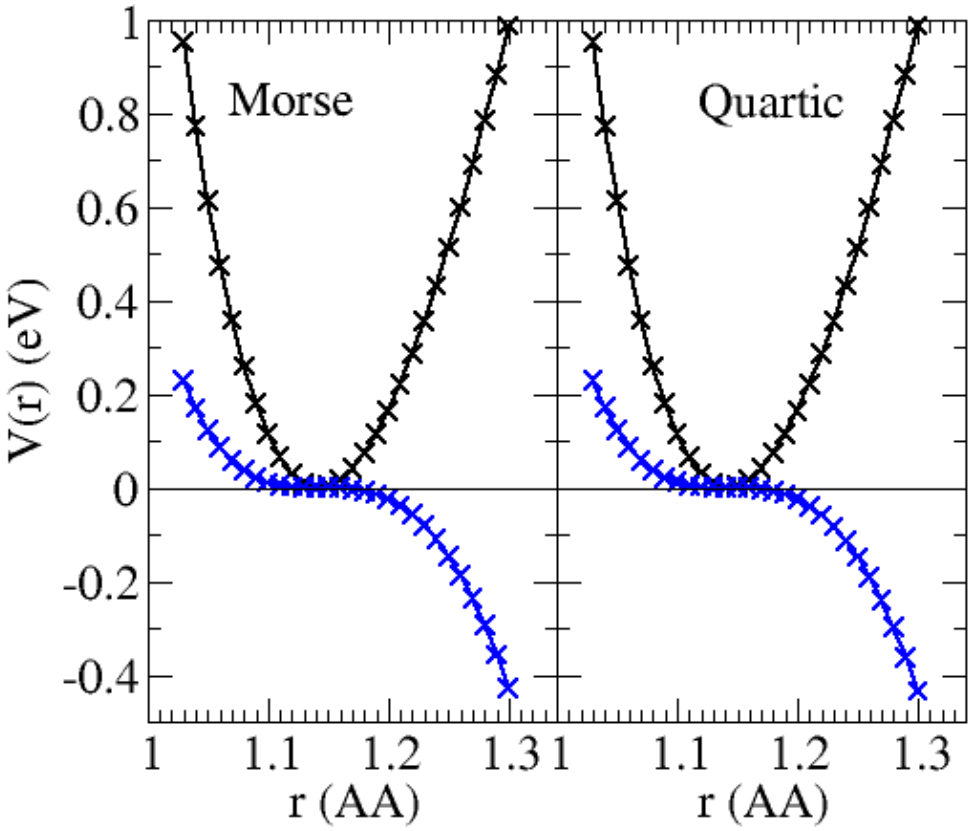

Figure 5.2: Calculated potential energy points (crosses) of the internal stretch mode of isolated CO and the corresponding fitted Morse and Quartic potential energy curves (lines) as a function of the C-O inter-atomic distance r. The anharmonic parts of the potential energy points (blue crosses) were obtained by subtracting the harmonic parts of the fitted model potentials from the calculated energy points and the anharmonic parts of the fitted model potentials are also shown (blue lines). The results were based on the optB86b-vdW functional.

5.5.2 CO-Cu(110)

In the case of the CO adsorption on the Cu(110) surface, we have studied three different ordered structures p(1x2), p(2x4) and p(3x6), corresponding to CO coverages of

1/2, 1/8 and 1/18 of a monolayer (ML), respectively. The adsorption site of the CO molecule was chosen to be on-top of a Cu atom as suggested by experiments [26].

As for the isolated CO molecule, essentially the same results for the anharmonic parts of the PECs were obtained for the PBE and optB86-vdW functionals for the p(1x2) structure but there are larger differences in the harmonic parts of the PECs as shown by the calculated harmonic frequencies in table 5.5. In contrast to the isolated CO molecule, the values for σ in tables 5.3 and tables 5.4 show that the quartic potential gives a a somewhat better fit to the PECs than the Morse potential. However, both potential fits give essentially the same values for the harmonic vibrational energies as for the CO molecule but $\tilde{\chi}$ is somewhat larger than χ as for the CO molecule.

Both the Morse and quartic potential fits give a significant decrease of χ and $\tilde{\chi}$ from the low- to the high-coverage structure. As shown by results from the quartic potential, the values for the quartic and cubic terms do not show any coverage dependence but the harmonic part show a substantial blue shift with increasing coverage. Thus the decrease of $\tilde{\chi}$ with coverage is not an effect of the difference in the anharmonicity of the PECs. This significant decrease is an effect of the large sensitivity of the anharmonicity of the vibrational frequencies to the root-mean-square amplitude δr. The increase of $h\nu_0$ by 2.2% and the corresponding decrease in δr^2 decreases $\tilde{\chi}$ by about 14% from the p(3x6) structure to the p(2x1) structure. Finally, we note from the quartic potential parameters that the anharmonic terms of the PEC are somewhat smaller by about 10% than for the isolated CO molecule. Thus the formation of CO chemisorption bond with the Cu(110) surface does not preserve the anharmonic part of the PEC as suggested by [93].

The origin of the blue shift of the calculated vibrational frequencies with increasing coverage is in large part due to the repulsive dipole-dipole interactions. The blue shift $\Delta\nu_0$ of the harmonic frequency by these interactions is given at the Γ point by,

$$(\nu_0 - \Delta\nu_0)^2 = \nu_0^2 - \frac{(e^*)^2 U}{4\pi^2 \mu}\,, \tag{5.23}$$

where ν_0 and $\nu_0 - \Delta\nu_0$ is the frequency with and without dipole interactions, respectively. The effective charge, $e^\star$, is the slope of the dipole moment with respect to $r - r_0$ of the C-O stretch and U is the dipole sum. The calculated effective charges are shown in table 5.2. The decrease of e^* for the adsorbed CO molecule compared to its calculated value -0.69e in the gas-phase is an effect of the partial occupation of the CO 2π* molecular orbitals [25]. The decrease of $|e^*|$ with increasing coverage is an effect of the screening by the adsorbed molecules [92]. The dipole sum U includes the image dipoles of the other molecules where we used the image plane distance of 0.93 Å with respect to the Cu surface suggested in Ref. [100]. The resulting frequency blue shifts

	e^* (e)	$\Delta\bar{\nu}_0$ (cm^{-1})	$\bar{\nu}_0 - \Delta\bar{\nu}_0$ (cm^{-1})
p(1x2)-CO/Cu(110)	-0.90	22.5	2034
p(2x4)-CO/Cu(110)	-1.26	6.2	2025
p(3x6)-CO/Cu(110)	-1.33	2.1	2023
CO-RuTPP/Cu(110)	-1.35	1.6	1922

Table 5.2: Calculated effective charges and blue shifts of the harmonic frequency due to dipole-dipole interactions. ν_0 and $\nu_0 - \Delta\nu_0$ is the frequency with and without dipole interactions, respectively.

from the dipole interactions are shown in table 5.2. These results show that the blue shift of the calculated vibrational frequencies with increasing coverage is dominated by the repulsive dipole-dipole interactions.

The downward shift of the calculated harmonic frequency of the CO stretch for the low coverage p(3x6) structure, where the dipole-dipole interactions are negligible, is consistent with the Badger relation [93],

$$\frac{d\nu_0}{dr} = -B \tag{5.24}$$

where B is badger slope. This relation is based on the assumption that the dominant effect of the adsorption is to introduce a constant force on the CO stretch. This assumption gives,

$$B = \frac{3|k_3^{\mathrm{CO}}|}{k^{\mathrm{CO}}}\nu_0^{\mathrm{CO}} \ , \tag{5.25}$$

where the superscript CO refers to the values for the CO molecule in the gas-phase. Using our calculated values for the CO molecule one obtains $\bar{B} = B/c = 7730$ cm^{-1}/Å. This relation gives a red shift of -93 cm^{-1} for the calculated increase of the equilibrium position by 0.012 Å upon adsorption of CO in the p(3x6) structure, which is close to the calculated value of -102 cm^{-1}.

Finally, in the case of the p(2x1) structure, we have also tested our approximation of keeping the centre-of-mass fixed when calculating the PEC by including the centre-of-mass motion and the motion of the coordinated Cu atom as described in Section 5.4. As shown in table 5.7, this correction changes marginally the internal stretch frequency suggesting that a fixed centre-of-mass position is a good approximation. This suggestion is proved by results of the fits shown in table 5.5. There are only minor changes in the anharmonic terms of the potential and the anharmonicity parameter when including the centre-of-mass motion and the motion of the coordinated Cu atom.

5.5.3 CO-MTPP and CO-MTPP/Cu(110)

Here we have studied the isolated CO-MTPP complex and the adsorbed complex on the Cu(110) surfaces in the A^{γ} structures with the central metal atoms M = Ru or Co. The geometric and the electronic structures of these complexes were studied extensively in chapter 4.

For all these complexes, we get significantly better fits to the calculated PECs using the quartic potential than for the Morse potential as shown by the values of σ in tables 5.3 and 5.4. However, the calculated harmonic vibrational frequencies show only small differences between the two fits. Except for CO-RuTPP, $\tilde{\chi}$ is slightly larger than for χ as for CO and CO-Cu(110). For the isolated and adsorbed CO-CoTPP complex, the calculated -158 and -159 cm^{-1} of the harmonic frequencies are close the values -147 and -162 cm^{-1} obtained from the Badger relation in Eq. (5.24). The corresponding shifts -240 and -247 cm^{-1} obtained from the Badger relation for the isolated and the adsorbed CO-RuTPP complexes overestimate substantially the corresponding calculated shift -181 and -208 cm^{-1} from the fit to the quartic potential. This overestimate might in part be due to the fact that the anharmonic terms of the isolated and the adsorbed CO-RuTPP complexes are substantially weakened by about 17-24 % whereas the weakening is less for the isolated and the adsorbed CO-CoTPP complexes. In both cases, the anharmonic terms of the PECs for CO stretch in the isolated complex do not change upon adsorption on the surface.

From the large red shifts of the harmonic frequencies of the C-O stretch frequencies of these complexes, one would expect a large increase of the anharmonicity parameter from the increase of the vibrational amplitudes δr but this increase is compensated by the weakening of the anharmonic part of the PECs. For example, keeping the anharmonic part of the isolated CO molecule for CO-RuTPP/Cu(110) would increase $\tilde{\chi}$ from 0.62% by about a factor of two to 1.3 %. Finally, the stronger anharmonic part of the PECc and the larger values of the anharmonicity parameter for the C-O stretch of the isolated and adsorbed CO-CoTPP complexes than for the corresponding CO-RuTPP complexes might be related to the tilting of the CO molecule in the CO-CoTPP complexes.

5.6 Comparison with Experiments

Here, we will focus on the comparison of our calculations with experiments for the anharmonicity of the vibrational frequencies for CO and CO-RuTPP on Cu(110).

In Fig. 5.3, we show the experimental data for C-O stretch frequencies for the fundamental and the hot band transitions as a function of coverage. The experimental

result that the fundamental frequency is essentially constant from a CO coverage of about 0.15 down to 0.01 ML is not supported by our calculations, which show a substantial shift with CO coverage due to the dipole-dipole interactions (table 5.5.2). The fundamental frequency has a blue shift of 6 cm^{-1} from the p(3x6) structure to the p(2x4) structure corresponding to an increase of coverage from 0.045 to 0.125 ML. Another puzzling observation is that the observed red shift of 53 cm^{-1} of the fundamental frequency upon adsorption is substantially closer to the corresponding calculated red shift of about 70 cm^{-1} (54 cm^{-1} for PBE) for the high-coverage p(2x1) structure than the corresponding value of 102 cm^{-1} for the low-coverage p(3x6) structure. The observed blue shifts of the hot-band transitions $1 \rightarrow 2$ and $2 \rightarrow 3$ with CO coverage is probably an effect of the increasing delocalization of the hot-band transitions with coverage. The low-coverage limit, $\Theta < 0.1$ ML should correspond to the singleton frequencies for these hot transitions. The corresponding measured frequency shifts $\Delta\Delta\bar{\nu}_n = \bar{\nu}_{n\rightarrow n+1} - \bar{\nu}_{n\rightarrow n-1}$ for n = 1 and 2 are in good agreement with the calculated ones as shown in table 5.6. Note that the difference between the experimental and calculated values of χ are slightly larger due to the underestimate of the harmonic vibrational frequency in the calculations.

The measured fundamental frequencies of the CO stretch of isolated CO-RuTPP and adsorbed CO-RuTPP on Cu(110), including hot band transitions for the adsorbed molecule, are shown in table 5.6. In the case of the adsorbed molecule, these frequencies were measured at sufficient low coverage so that they correspond to singleton frequencies. The magnitudes of the red shifts upon adsorption are in good agreement with the calculated red shifts for the isolated and adsorbed molecule but the results for the isolated molecule underestimates the measured red shift. Note that for the coverage used in the calculations the blue-shift from the dipole-dipole interactions are small so that the these result can be compared directly with the experimental data. The measured anharmonic frequency shifts and the corresponding anharmonicity parameters are underestimated by 20%. Thus the calculations cannot reproduce the trend of the anharmonicity of the vibrational frequencies between CO adsorbed on Cu(110) and on RuTPP/Cu(110).

5.7 Summary

The anomalous large value of anharmonicity of the internal stretch mode of CO adsorbed on RuTPP/Cu(110), as obtained from the SFG experiments of the fundamental

	χ (%)	$\bar{\nu}_0$ (cm^{-1})	r_0 (Å)	D_e (eV)	α (Å^{-1})	σ (meV)
			CO			
PBE	0.66±0.02	2126±0.02	1.144	10.1 ±0.02	2.38	0.14
optB86b-vdW	0.65±0.02	2127±0.2	1.143	10.1 ±0.03	2.38	0.17
			p(2x1)CO/Cu(110)			
PBE	0.58±0.03	2069±0.4	1.157	11.0±0.06	2.21	0.34
optB86b-vdW	0.59±0.04	2056±0.4	1.157	10.7±0.06	2.24	0.33
optB86b-vdW*	0.59±0.04	2062±0.5	1.157	10.9±0.06	2.22	0.35
			p(2x4)CO/Cu(110)			
optB86b-vdW	0.64±0.3	2031± 0.5	1.155	9.8±0.05	2.30	0.38
			p(3x6)CO/Cu(110)			
optB86b-vdW	0.66±0.04	2025±0.5	1.155	9.6 ±0.05	2.33	0.37
			CO-RuTPP			
optB86b-vdW	0.57±0.05	1953±0.7	1.175	10.7±0.1	2.12	0.63
			CO-RuTPP/Cu(110)			
optB86b-vdW	0.62±0.04	1924±0.6	1.175	9.6 ±0.07	2.21	0.5
			CO-CoTPP			
optB86b-vdW	0.70±0.03	1970±0.04	1.162	8.76 ±0.04	2.36	0.23
			CO-CoTPP/Cu(110)			
optB86b-vdW	0.71±0.2	1962±0.4	1.164	8.60 ±0.04	2.34	0.39

Table 5.3: Anharmonicity parameter χ, harmonic vibrational energy $hc\bar{\nu}_0$, equilibrium distances r_0 and dissociation energy D_e for the internal stretch of CO in various bonding situations as obtained from fits of Morse potentials to the calculated potential energy curves. Results are also given in few instances for both the optB86b-vdW and the PBE versions of the exchange-correlation energy functional as indicated. The error bars for the calculated values are the standard deviations in the non-linear square fit. The standard deviation in the fit of the Morse potential curve to the calculated potential energy curve (PEC) is given by σ.

	$\tilde{\chi}$ (%)	$\bar{\nu}_0$ (cm^{-1})	k_3 (eV/Å^3)	k_4 (eV/Å^4)	σ (meV)
			CO		
PBE	0.71	2127±0.6	-138±0.3	186±3	0.17
optB86b-vdW	0.71	2128±0.6	-138±0.3	185±3	0.18
			p(1x2)CO/Cu(110)		
PBE	0.58	2066±0.6	-123±0.2	173±3	0.16
optB86b-vdW	0.60	2053±0.6	-122±0.2	173±3	0.15
optB86b-vdW*	0.59	2059±0.6	-122±0.3	172±3	0.18
			p(2x4)CO/Cu(110)		
optB86b-vdW	0.68	2029±0.6	-123±0.3	172±3	0.18
			p(3x6)CO/Cu(110)		
optB86b-vdW	0.70	2024±0.6	-124±0.3	173±3	0.19
			CO-RuTPP		
optB86b-vdW	0.54	1947±0.6	-105±0.2	154±3	0.20
			CO-RuTPP/Cu(110)		
optB86b-vdW	0.62	1920±0.6	-106±0.2	152±3	0.21
			CO-CoTPP		
optB86b-vdW	0.75	1969±0.6	-119±0.3	166±3	0.22
			CO-CoTPP/Cu(110)		
optB86b-vdW	0.75	1960±0.7	-119±0.3	171±3	0.23

Table 5.4: Harmonic vibrational energy $hc\bar{\nu}_0$, cubic k_3 and quartic k_4 force constants and for the internal stretch of CO in various bonding situations as obtained from a fit to the polynomial potential $V_Q(r)$ to the calculated potential energy curve. The standard deviation in the fit of this potential to the calculated potential energy curve is given by σ. Results are also given in few instances for both the optB86b-vdW and the PBE versions of the exchange-correlation energy functional as indicated.

	$\bar{\nu}_{0-1}$ (cm^{-1})	$\Delta\bar{\nu}_{0-1}$	$\Delta\Delta\bar{\nu}$ (cm^{-1})
	CO		
PBE	2097 (2096)	0 (0)	-28 (-30)
optB86B-vdW	2100 (2098)	0 (0)	-28 (-30)
	p(2x1)CO/Cu(110)		
PBE	2045 (2042)	-52 (-54)	-24 (-24)
optB86B-vdW	2032 (2028)	-68 (-70)	-25 (-25)
	p(2x4)CO/Cu(110)		
optB86B-vdW	2005 (2002)	-95 (-96)	- 26 (-28)
	p(3x6)CO/Cu(110)		
optB86B-vdW	1999 (1996)	-101 (-102)	- 27 (-28)
	CO-RuTPP		
optB86b-vdW	1932 (1927)	-168 (-171)	-22 (-21)
	CO-RuTPP/Cu(110)		
optB86b-vdW	1900 (1896)	-200 (-202)	-24 (-24)
	CO-CoTPP		
optB86b-vdW	1942 (1939)	-158 (-159)	-27 (-29)
	CO-CoTPP/Cu(110)		
optB86b-vdW	1934 (1931)	-166 (-167)	-28 (-30)

Table 5.5: Calculated vibrational frequencies for the fundamental internal stretch of the CO molecule in various bonding situations and the constant frequency shifts $\Delta\Delta\bar{\nu} = \bar{\nu}_{n-n+1} - \bar{\nu}_{n-1-n}$ for the overtones. The values and the values within the parenthesis are based on the Morse and the Quartic potential, respectively. $\Delta\bar{\nu}_{0-1}$ is the shift of $\bar{\nu}_{0-1}$ from its gas-phase value. [(e)]Ref. [101][Ref. 265 in [86]]; [(e)]Ref. [86] in the A^{γ} structure.

	$\bar{\nu}_{0-1}$ (cm^{-1})	$\Delta\bar{\nu}_{0-1}$	$\Delta\Delta\bar{\nu}_1$ (cm^{-1})	$\Delta\Delta\bar{\nu}_2$ (cm^{-1})
CO[(a)]	2143.2	0	-26.6	-
CO/Cu(110)[(b)]	2090	-53	-26.5	-28.5
CO/Ru(001)[(c)(d)]	1990	-153	-29	-
CO-O/Ru(001)[(d)]	2069	-74	-29	-
CO-RuTPP[(e)]	1944	-199	-	-
CO-RuTPP/Cu(110) [(f)]	1957	-186	-30	-32

Table 5.6: Experimental vibrational frequencies $\bar{\nu}_{0-1}$ for the fundamental internal stretch of the CO molecule in various bonding situations and their frequency shifts $\Delta\Delta\bar{\nu}_1 = \Delta\bar{\nu}_{1-2} - \bar{\nu}_{0-1}$ and $\Delta\Delta\bar{\nu}_2 = \Delta\bar{\nu}_{2-3} - \bar{\nu}_{1-2}$ for the overtones. $\Delta\bar{\nu}_{0-1}$ is the shift of $\bar{\nu}_{0-1}$ from its gas-phase value. [(e)]Ref. [101]; [(e)]Ref. [86]

in the A^γ structure

	$\bar{\nu}_{\mathrm{I}}$ (cm^{-1})	$\bar{\nu}_{\mathrm{M}}$ (cm^{-1})
p(2x1)CO/Cu(110)	2047	417 (345)[(a)]
CO-RuTPP/Cu(110)	1927	508 (452)[(b)]

Table 5.7: Calculated harmonic vibrational frequencies ν_{I} and ν_{M} of the internal (I) and the external (M) CO stretch, respectively. The values within the parenthesis are the experimental values for the fundamental frequencies of M are taken from IR spectroscopy; [(a)] Ref. [86]; [(b)] Ref. [86]. Only the perpendicular motions of the C, O and the coordinated metal atom were included in the dynamical matrix.

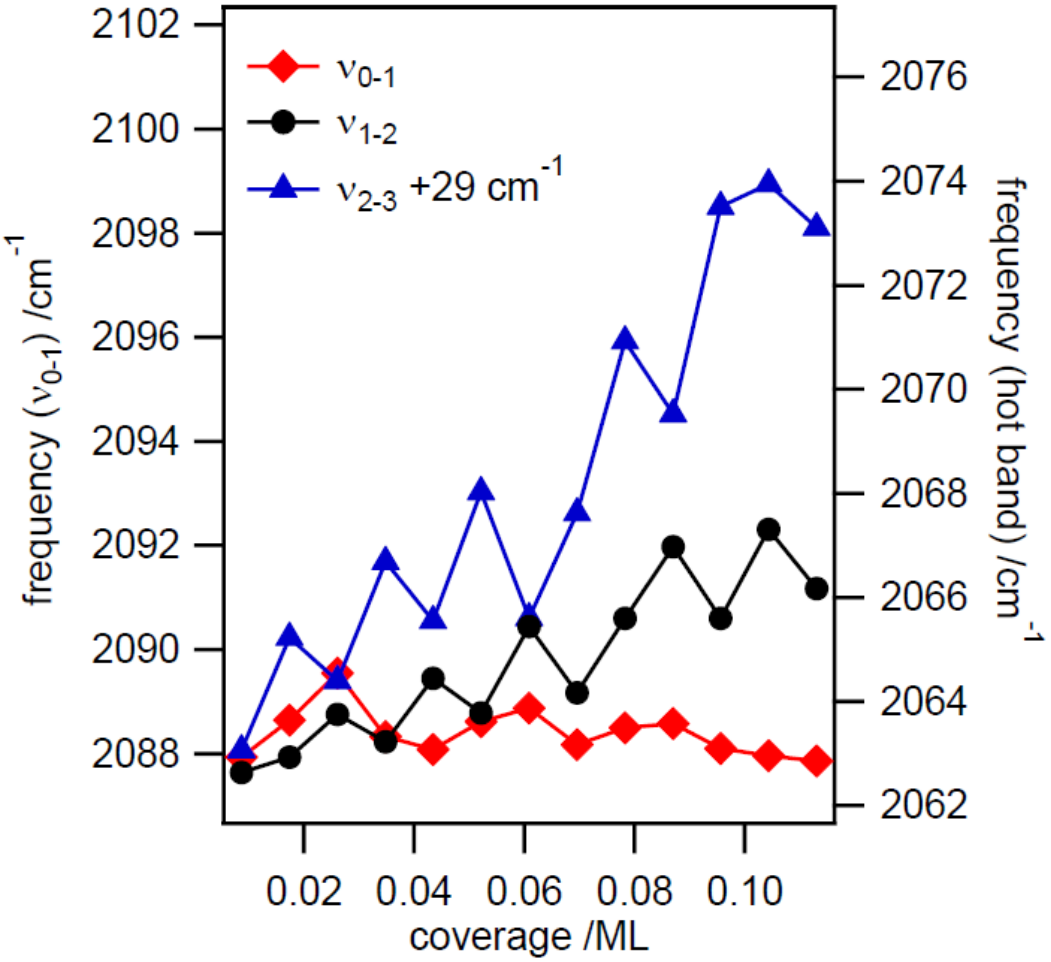

Figure 5.3: The frequency shifts of the fundamental, 0-1, and the hot band transitions 1-2 and 2-3 of the C-O stretch mode as a function of CO coverage. The frequency shifts were obtained from SFG experiments. The figure is taken from T. Omiya thesis [86]

and the first overtone frequencies by Arnolds and Omyia at University of Liverpool, raises some questions concerning the bonding of CO to the metal centre of the adsorbed RuTPP. This observation motivated us to carry out DFT calculations of this anharmonicity for CO in various bonding situations. The anharmonicity was calculated in two different ways from the calculated potential energy curve (PEC) by a fit of a Morse potential to the PEC and by leading order perturbation theory in the cubic and quartic terms of the PEC. These two methods gave very similar results. The Morse potential method is a bit restrictive since the harmonic and the anharmonic parts of the PEC cannot be fitted independently in contrast to the perturbative method. The perturbative method can account for the change of only the harmonic part of the PEC due to dipole-dipole interaction with CO coverage on the Cu(110) surface. In partic-

ular, the anharmonicity of the internal stretch mode increased in this case with decreasing vibrational frequency due to the increase of the vibrational amplitude. A good agreement between the observed and calculated anharmonicities of the internal stretch mode of the isolated and the adsorbed molecule on the Cu(110) surface was obtained. However, our calculations were not able to reproduce the observed anomalous value for CO adsorbed on RuTPP/Cu(110) and a similar value to the isolated and adsorbed CO was obtained.

Chapter 6

Homo-coupling of porphine on Au(111)

6.1 Introduction

In this Chapter, we present a DFT study of the on-surface formation of porphine dimers by C-C coupling from monomers on an Au(111) surface. This study is motivated by recent and unpublished STM experiments of this reaction by the experimental groups headed by Raval at the University of Liverpool and by Grill at University of Graz. In these experiments different oligomerization pathways and bonding motifs were investigated at different temperatures.

This oligomerization reaction is an example how nano structures can be created from covalent coupling at surfaces which has recently attracted a lot of attention [74, 102–104]. The first pioneering study of such a reaction was done by Grill and coworkers [102] who demonstrated that the topology of nanostructures could be precisely designed by controlling the chemical structure of halogenated porphyrin molecules. In this on-surface synthesis, the C-C bonds between the molecules were formed first by breaking the halogen-molecule bond resulting in a halogen contamination of the surface. Later it was demonstrated by In't Veld and coworkers [105] that it was possible to form C-C bonds between adsorbed molecules directly from C-H bonds where the H atoms desorbs from the surface without without contaminating the surface. Various nanostructures of porphyrin molecules on a Cu surface can also be formed in the presence of Cu adatoms resulting in C-Cu-C coupling[103, 104].

Based on their STM images, Grill group and Rasmita group were able to identify four different bonding motifs of the adsorbed dimers on Au(111). The two experiments were carried out with different deposition and annealing and cooling procedures, and the statistic concerning the formation of these structures resulted in some

differences between the two experiments. Using a range of temperatures between $250°$C and $400°$C in Graz, the single monomers were deposited at the different elevated surface temperatures and imaged at the low temperature, whereas in Liverpool using a range between $300°$C and $380°$C porphines were deposited at room temperature and annealed at the temperature taken in consideration, with an imaging at room temperature. These experiments raise the question to what extent these different product distributions are determined by thermodynamics or kinetics depending on the deposition and annealing conditions.

As a first step to resolve this question, we have studied the thermodynamics of the dimer formation by calculating the geometric structure and the relative stabilities of the adsorbed dimers, monomers and dehydrogenated intermediates [74]. The assignment of the different C-C bonding motifs of the dimers from the observed STM images is also investigated by a comparison with calculated STM images. In particular, the discrimination between single and double connected dimers is of interest. Since the adsorbed porphyrin monomers and dimers was found in our calculations to be physisorbed reflecting the relatively inert character of the Au(111) surface, we have also investigated the dimer formation in the gas phase.

6.2 Computational details

The periodic DFT calculations of the geometric structure and the total energies of the isolated and the adsorbed porphyrin monomers and dimers were carried out using the Vienna Ab initio Simulation Package (VASP), [81], [82], [106] version 5.3. The key input parameter were chosen to be essentially the same as the VASP calculations of porphyrin on a Cu surface [32].

Plane waves were used as a basis set with a kinetic energy cut-off of 400 eV. Valence electron-core interactions were included by using the projector-augmented wave method [83], [84]. The van der Waals interactions were described using optB86b-vdW version of the van der Waals exchange-correlation functional [107]. Spin-polarization was included in the dehydrogenation calculations. The isolated porphyrin monomer and dimers were represented in a super cell of 25x25x25 Å^3 and only the Γ point was kept in the k-point sampling of the Brillouin zone (BZ). In the calculations of the adsorption of P on Au(111), Au(111) was represented by a slab in a super cell with a (7x6) surface unit cell and 4 layer of Au and the height of the vacuum region was 30.4 Å. The BZ was sampled by a 2x2x1 k-point grid. Different surface unit cells were chosen for the dimers adsorbed on Au(111). For the case of single-connected dimer, the (9x6) surface unit cell and a (2x3x1) k-point sampling was used, whereas for the

cases of multiple-connected dimer, the surface unit cell was (11x6) and a 2x4x1 k-point sampling was used. The isolated molecules were geometrically optimized until the forces were less than 0.02 eV. For the adsorbed monomers and dimers, the structures were relaxed until the forces were less than 0.02 and 0.03 Å^{-1}, respectively, while the two bottom layers of the Au slab were fixed at the calculated bulk lattice constant of 4.135 Å. The lattice constant was obtained by finding the minimum of the potential energy curve of simple cubic supercell of four Au atoms in a face centred cubic structure as a function of lattice constant in steps of 0.005 Å. The density functional and the plane-wave kinetic energy cut-off were the same as the calculations for the adsorbed molecules and the a (12x12x12) sampling of the k point in the BZ. Finally, the STM images were calculated from the wave functions in the vacuum region using the Tersoff-Hamann approximation.

6.3 P monomer and dimers in the gas phase

6.3.1 P monomer

The calculated equilibrium structure of the isolated porphine (P) in the gas phase was found to be planar. The $trans$ tautomer of the inner H atoms was found to be 0.3 eV more stable than the cis tautomer. The resulting structure is shown in Fig. 6.1.

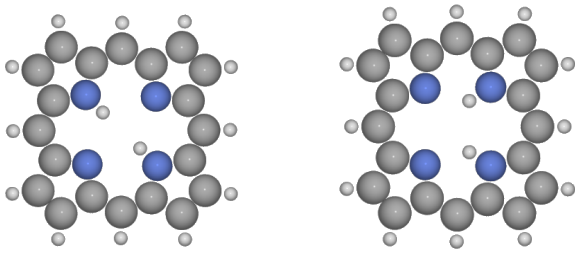

Figure 6.1: Trans and cis configurations of H2P.

6.3.2 P dehydrogenation

A possible reaction intermediate in the formation of the a P dimer from two P monomers is a dehydrogenated P here denoted by P(-nH) where n is the number of dehydrogenated C atoms. The dehydrogenation reaction is given by,

$$\text{P} \rightarrow \text{P}(-n\text{H}) + \frac{n}{2}\text{H}_2. \tag{6.1}$$

There are several ways the C atoms of the P can be dehydrogenated. In the case of single dehydrogenation ($n = 1$) either a C atom at the edge or the corner position of P is dehydrogenated (see, Fig. 6.2). In the case of double and triple dehydrogenations of P, we have considered those that should be most relevant for the formation of P dimers. They are shown in Fig. 6.3 and 6.3. The feasibilities for the various dehydrogenations can be obtained from the changes in the total energies $\Delta_r E$ of the reaction, Eq. 6.1, given by,

$$\Delta_r E = E_{\mathrm{P}(-n\mathrm{H})} + \frac{n}{2} E_{\mathrm{H}_2} - E_{\mathrm{P}} \tag{6.2}$$

where E_{P}, $E_{\mathrm{P}(-n\mathrm{H})}$ and E_{H_2} are the total energies of P, P(-nH) and the hydrogen molecule, respectively. The calculated $\Delta_r E$ for the considered single, double and triple dehydrogenations are shown in Table 6.1. Note that $\Delta_r E$ is not the free energy of the reaction since it does not include any free energy terms from the roto-vibrational and translational motion of the molecules. However, $\Delta_r E$ can still be used to determine the relative stabilities of the two P(-H) and the relative stabilities of the two P(-2H) since these terms for the H_2 molecules cancel out and the small free energy terms from the differences in roto-vibrational motion of the P and P(-nH) molecules is ignored here.

As shown by the calculated $\Delta_r E$ in Table 6.1, the dehydrogenation of the edge C atom is more stable than the corner C atom by about 0.27 eV. Furthermore, the double and the triple dehydrogenation energies are close to be additive in terms of the single dehydrogenation energies except for the adjacent double corner C atom dehydrogenation. The dehydrogenation energy of these two C atoms is about 0.6 eV less than twice the energy of the dehydrogenation of a corner C atom.

These calculated values for the dehydrogenation energies compare favourably with the energy obtained from measured H bond dissociation energies D_{H} for H-H and C-H. $\Delta_r E = D_{\mathrm{H}}$(C-H $\rightarrow$ C + H) - $\frac{1}{2} D_{\mathrm{H}}$(H-H $\rightarrow$ 2H) = 2.27 eV using the mean value for D_{H}(C-H $\rightarrow$ C + H = 4.51 eV and D_{H}(H-H $\rightarrow$ 2H) = 4.48 eV [108]. Note that these values are bond entalpies at 298 K and include zero-point energies and heat capacities.

6.3.3 Dimer formation

A P dimer can be formed from two P monomers by either making single, double or triple C-C connection between the P monomers, which are described by the reaction,

$$2\mathrm{P} \rightarrow \mathrm{P}(-n\mathrm{H})_2 + n\mathrm{H}_2 \tag{6.3}$$

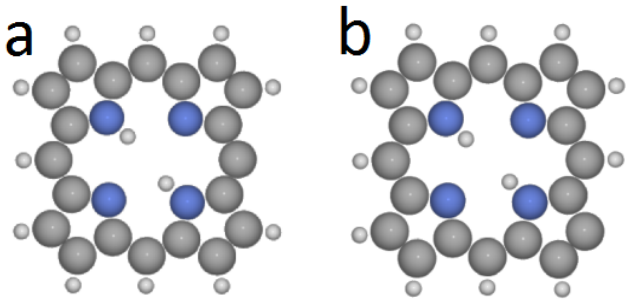

Figure 6.2: Single C a) edge and b) corner atom dehydrogenation of a P monomer.

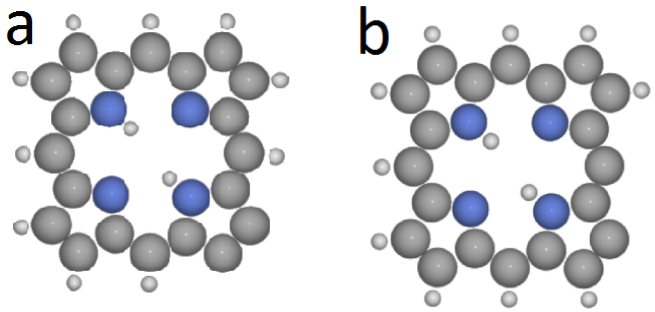

Figure 6.3: a) Double C corner atoms and b) corner-edge atoms dehydrogenation of a P monomer.

where P(-nH) is P dehydrogenated by n H atoms and n = 1, 2 and 3 for single-, double-connected and triple-connected dimers, respectively. The corresponding reaction energies $\Delta_r E$ are then given by,

$$\Delta_r E = E_{\mathrm{P}(-n\mathrm{H})_2} + nE_{\mathrm{H}_2} - 2E_{\mathrm{P}}, \tag{6.4}$$

where $E_{\mathrm{P}(-n\mathrm{H})_2}$ is the total energy of the n-connected dimer.

Here we have also investigated the strengths of C-C bonds between the monomers by calculating their dissociation energies D_{C}. This bond dissociation corresponds to the reaction,

$$\mathrm{P}(-n\mathrm{H})_2 \rightarrow 2\mathrm{P}(-n\mathrm{H}) \tag{6.5}$$

and D_{C} is then given by,

$$D = 2E_{\mathrm{P}(-n\mathrm{H})} - E_{\mathrm{P}(-n\mathrm{H})_2} \tag{6.6}$$

All calculated values for D_{C} and $\Delta_r E$ are shown in Tables 6.2 and 6.3, respectively.

Single-connected dimers

There are essentially four possible configurations of single-connected dimers. Two configurations correspond to the bonding of edge and corner C atoms denoted here

	$\Delta_r E$(g) (eV)	$\Delta_r E$(ad) (eV)	
		hollow	top
edge	2.79	1.68	2.79
corner	3.06	1.84	1.61
corner-edge	5.85-5.76		
corner-corner	5.51		2.99
corner-edge-corner	8.82		

Table 6.1: Calculated dehydrogenation energies $\Delta_r E$(g) and $\Delta_r E$(ad) of P in the gas phase and adsorbed on Au(111) in a hollow and a top site.

by (ec) and to the bonding of edge and edge C atoms denoted here by (ee). The other two configurations correspond to bonding of corner and corner C atoms in two inequivalent ways and are denoted here by (cc) and (cc)'.

The geometrically optimized structures of these four configurations are shown in Fig. 6.4. As shown by the side views, there are significant twist and distortions of the P monomers in the dimer from their native flat configurations due to steric hindrances introduced by the close proximity of adjacent C-H bonds to the C-C bonds. These distortions are particulary large for the (ee) configuration where the molecular planes have a large twist.

The relative stabilities of these different bonding configurations were obtained from the calculated changes in reaction energies for making single-connected dimer given by $\Delta_r E$ in Eq. (6.3) for $n = 1$. As shown by the calculated $\Delta_r E$ in Table 6.2, (cc) and (cc)' are the most stable configurations and are nearly degenerate. The (ec) configuration is the least stable one and $\Delta_r E$ is about 0.8 eV larger than for (cc) configuration, which is somewhat counterintuitive in view of the dehydrogenation of an edge C atom is more favoured than by a corner C atom. This trend in energies follows the trend of the different C-C bond strengths. As shown in Table 6.3, the calculated value of D_{C} increases with around an 1 eV when going from the edge-edge to the corner-corner C-C bond. These calculated values for D_{C} are in the range of measured values of D_{C} of about 3.8 eV for C-C single bonds to 7.5 eV for C-C double connection.

Double-connected dimers

There are five possible bonding configurations of double-connected dimers involving bonding of different combinations of edge and corner C atoms and here we consider four of them. In the dimer configuration denoted here by $(cc)^2$, the two C-C bonds are formed between corner C atoms of the monomers, whereas the dimer configuration

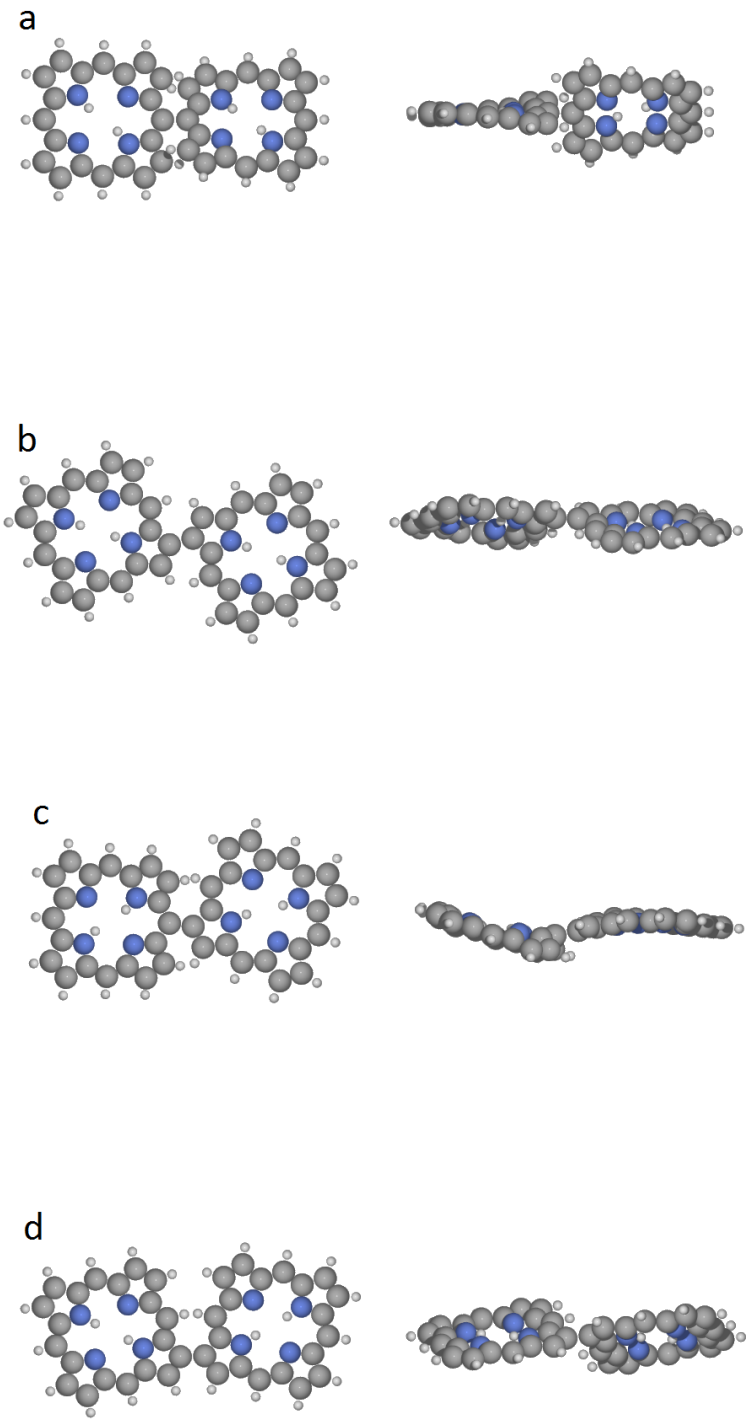

Figure 6.4: Top and side views of calculated equilibrium structures of the motifs (ee), (cc)′, (ec) and (cc) of single-connected dimers in the gas phase.

Dimer	$\Delta_r E(\mathrm{g})$ (eV)	$\Delta_r E(\mathrm{ad})$ (eV)
(ce)	1.08	1.98
(ee)	0.56	2.33
(cc)	0.20	1.03
(cc)′	0.21	0.78
$(cc)^2$	4.38	4.75
(cc)(ee)	1.53	2.96
(cc)′(ce)	1.44	1.86
$(ce)^2$	0.68	1.04
$(cc)^2$(ee)	0.51	1.00

Table 6.2: Calculated reaction energies $\Delta_r E(\mathrm{g})$ and $\Delta_r E(\mathrm{ad})$ of different motifs of single- and multiple-connected P dimers in the gas phase and adsorbed on Au(111), respectively.

Dimer	D_{C} (eV)
(ce)	4.77
(ee)	5.03
(cc)	5.90
(cc)′	5.91
$(cc)^2$	6.64
(cc)(ee)	9.49
(cc)′(ce)	9.92-9.83
$(ce)^2$	11.02-10.84
$(cc)^2$(ee)	17.13

Table 6.3: Calculated C-C bond dissociation energies D_{C} of different motifs of single- and multiple-connected P dimers in the gas phase.

formed by the two C-C bonds between corner and edge C atoms of the monomers is denoted by $(ce)^2$. In the dimer configuration denoted by (cc)'(ce) one C-C bond is formed between two corner C atoms and the other one is formed between a corner and an edge atom. Finally, the dimer configuration denoted by (cc)(ee) is formed between two corner atoms and between two edge atoms structures of these four dimer configurations are shown in Figs. 6.5a)-c). In all these cases, the dimers are flat as expected for all configurations except (cc)(ee) from the relatively large distances between the C-H bonds of the two P monomers in these dimers.

The relative stabilities of these dimer configurations were obtained from the reaction energies $\Delta_r E$ of the double-connected dimer which are given by Eq. (6.6) for $n = 2$. As shown by the calculated reaction energies $\Delta_r E$ in Table 6.2, there are quite large differences in the relative stabilities of the four configurations. Most notable is the result that $\Delta_r E$ is much larger for $(cc)^2$ than for the other three configurations. The trend of these relative stabilities can be understood from the increasing strain to form the C_6, C_5, C_4 rings in $(ce)^2$, (cc)'(ce) and $(cc)^2$, respectively, by C-C coupling. Note that also a C_6 ring is formed in the (cc)(ee) dimer but the strain to distort the H atoms away from each other of the non-connected corner atoms makes $\Delta_r E$ larger than the (cc)'(ce) dimer in which a C_5 ring is formed. $D_{\rm C}((cc)^2)$ = 6.64 eV is substantially larger than $2D_{\rm C}((cc))$ = 11.8 eV, whereas $D_{\rm C}((cc)'(ce))$ = 9.92 and $D_{\rm C}((cc)(ee))$ = 9.49 eV are much closer to $D_{\rm C}((cc))$ + $D_{\rm C}((ce))$ = 10.67 eV and $D_{\rm C}((cc))$ + $D_{\rm C}((ee))$ = 10.93 eV, respectively. In the case of $(ce)^2$ there is a cooperative effect for the formation of the double C-C connection and the six-membered C ring since $D_{\rm C}((ce)^2)$ = 11.02 eV is a bit larger than $2D_{\rm C}((ce))$ = 9.54 eV.

Triple-connected dimer

There is only one possible triple-connected dimer configuration, which has two equivalent bonds between two corner C atoms and one bond between two edge C atoms. This bonding motif is denoted here by $(cc)^2(ee)$. The geometrically optimized structure of this dimer is shown in Fig. 6.5 d). As expected this dimer is also flat. The calculated reaction energy $\Delta_r E$ of the triple-connected dimer as obtained from Eq. 6.6 is shown in Table 6.2. Here the calculated $D_{\rm C}$ in Table 6.3 shows that the formation of the triple C-C connections is slightly favoured by about 0.3 eV over forming three separate single C-C bonds: $D_{\rm C}((cc)^2(ee))$ = 17.1 > $2D_{\rm C}((cc))$ + $D_{\rm C}((ee))$ = 16.8 eV.

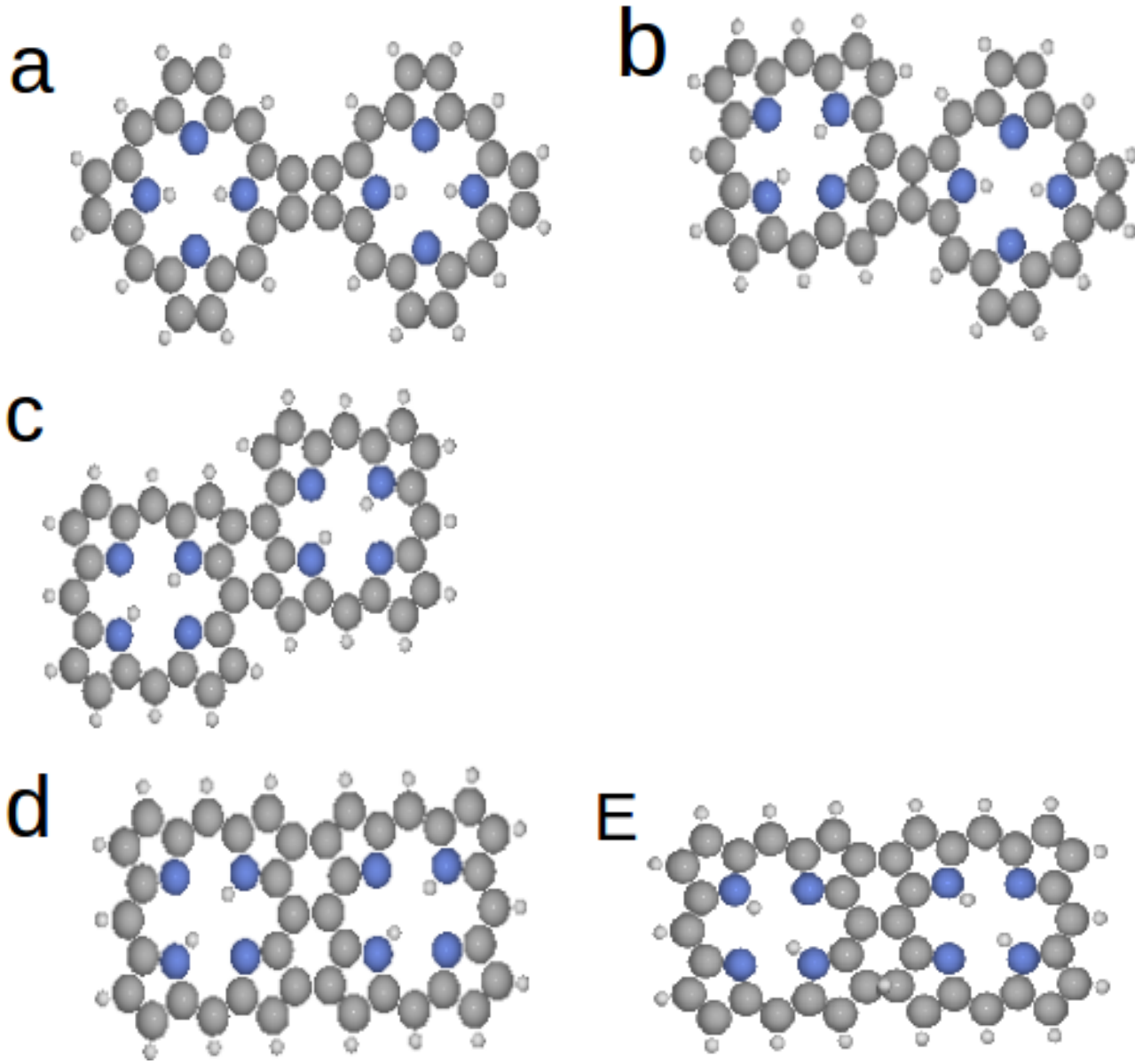

Figure 6.5: Top views of calculated structures of the double-connected motifs a) $(cc)^2$, b) (cc)'(ce), c) $(ce)^2$ the triple-connected motif d) $(cc)^2$(ee) of dimers in the gas phase and e)(cc)(ee) double connection.

6.4 Adsorption of P monomer and dimers on Au(111)

6.4.1 P adsorption

Two different adsorption sites were investigated for the P molecule adsorbed on the Au(111) surface. The two initial sites in the geometrical optimization were the top and hollow sites where the centre of the P molecule is on top of a Au atom and in a

hollow site on Au(111), respectively and the molecule is oriented with an edge parallel at the [110] direction of the Au(111) surface. As shown by the calculated structures of the adsorbed P in Fig. 6.6 b)-c), the adsorbed P is slightly displaced from the initial top site in the optimized configuration, which will be referred to as the top-like site, whereas the adsorbed P stays at hollow site during the geometrical optimization. The adsorbed molecule was found to be slightly deformed from its flat configuration in the gas phase with an adsorption height of 3.175 Å. This large value of the adsorption height is characteristic for physisorption, which can be reconciled with the calculated adsorption energies. The adsorption energy, E_{ad}, of P on Au(111) is here defined as the energy gain upon adsorption as,

$$E_{\mathrm{ad}} = E_{\mathrm{P}} + E_{\mathrm{Au(111)}} - E_{\mathrm{P/Au(111)}} \tag{6.7}$$

where $E_{\mathrm{Au(111)}}$ and $E_{\mathrm{P/Au(111)}}$ are the total energies of the bare surface and the adsorbed molecule on the bare surface, respectively. The hollow site with E_{ad} = 2.79 eV was found to be slightly more stable by about 0.09 eV than the top-like site. The orientational dependence of E_{ad} was also investigated on the top-like site by considering the orientational angles of 36°, 72°, 108°, and 144° respect to the centre of porphine axis at the initial position shown in figure 6.6. The variation of E_{ad} was found to be less than 0.19 eV. The calculated value of the adsorption energy and its weak dependence with site and orientation is in fact consistent with physisorption. Note that the van der Waals interaction energy scales with the size of the molecule and the calculated values of E_{ad} correspond to about 80 meV per atom which is in accordance with the scaling found for the adsorption energy of hydrocarbons on graphene [109].

6.4.2 H adatom

In the case of the on-surface dehydrogenation and monomer reactions, the produced hydrogen atoms can also end up adsorbed on the surface. Thus it is of interest to know the stability of the adsorbed H atom relative to the gas-phase, which is obtained from the reaction energy $\Delta_r E$ for the desorption of two adsorbed H atoms,

$$2\mathrm{H(ad)} \rightarrow \mathrm{H_2} \tag{6.8}$$

and $\Delta_r E$ is then given by,

$$\Delta_r E = E_{\mathrm{H_2}} - 2E_{\mathrm{H(ad)}} \tag{6.9}$$

In previous DFT calculations using the same vdW-DF as used here by Lucci and coworkers [110], they obtained $\Delta_r E$ = -0.28 eV. Furthermore, they calculated also the

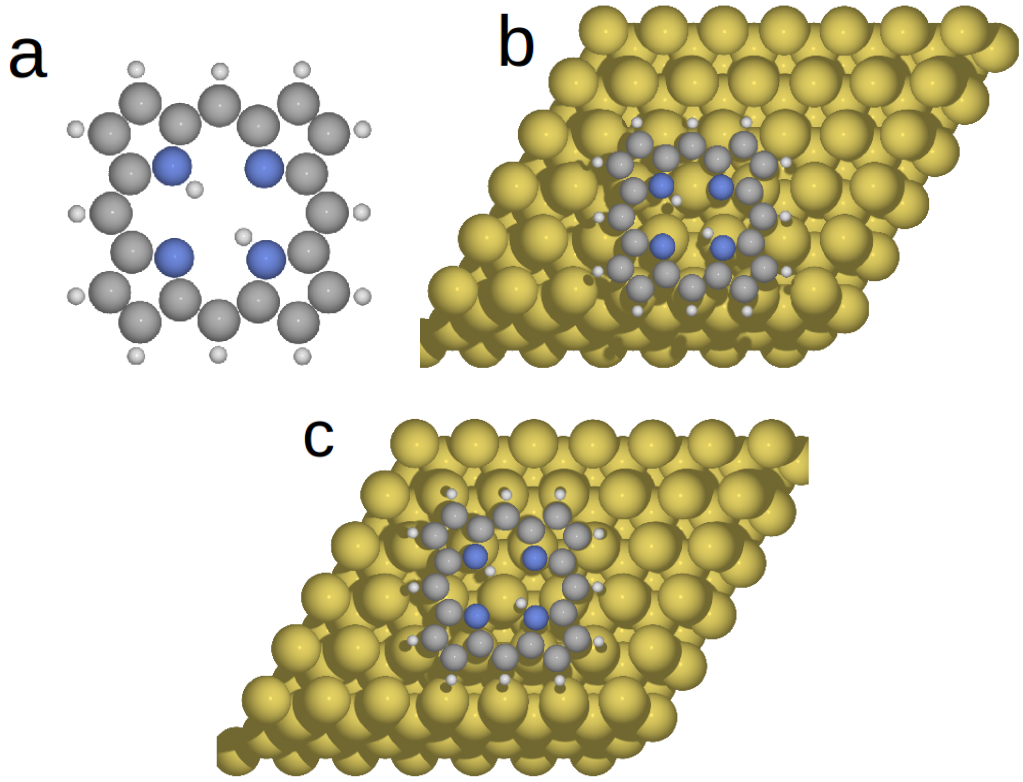

Figure 6.6: Calculated equilibrium structures of P in a) the gas phase and adsorbed on Au(111) surface starting from b) the hollow site and c) the top site.

energy barrier E_B to be 0.76 eV for the desorption. This barrier height will be important in the discussion in Section 6.5 about the reaction mechanisms.

6.4.3 P dehydrogenation

An important question is whether the dehydrogenation reaction,

$$\mathrm{P(ad)} \rightarrow \mathrm{P}(-n\mathrm{H})(\mathrm{ad}) + \frac{n}{2}\mathrm{H}_2, \tag{6.10}$$

of the adsorbed P is catalyzed by the surface or not. In the case of the dehydrogenation of a corner C atom, the calculated structures of P(-H)(ad) in Figs. 6.7 and 6.8 show that the corner C atom forms a bond with an Au atom with a characteristic bonding distance of 2.1 Å for both hollow and top-like sites. This bonding results also in a quenching of the spin moment, a significant deformation of the dehydrogenated molecule and an outward displacement of the Au atom. In the case of the dehydrogenation of an edge C atom, this kind of bond only occurs for the hollow site whereas for the top-like site no such bond is formed and the dehydrogenated P keeps the nearly flat geometry and spin-moment of the dehydrogenated P in the gas-phase. Also in the

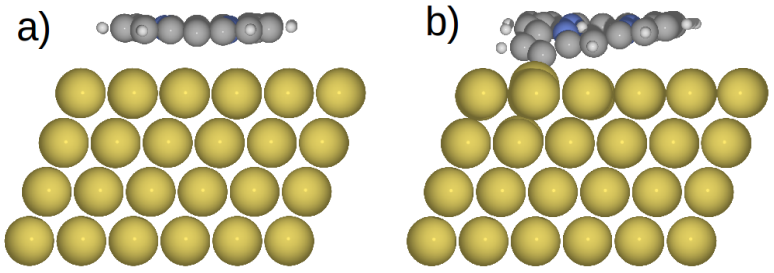

Figure 6.7: Calculated equilibrium structures of P(-H) on top site, when removing H from a) an edge C atom and b) a corner C atom.

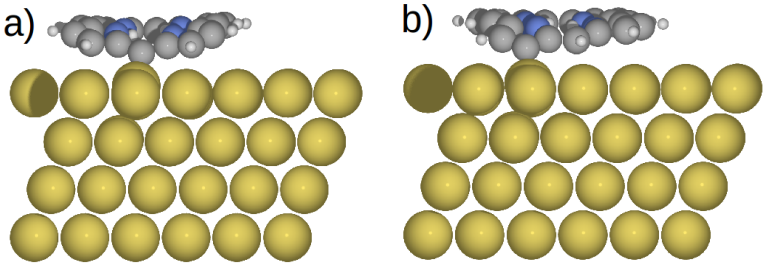

Figure 6.8: Calculated equilibrium structures of P(-H) on hollow site, when removing H a) an edge C atom and b) a corner C atom.

case of a double dehydrogenation of the two adjacent corner C atoms, they form both bonds with the Au surface atoms.

The C-Au bonding has a large influence on the dehydrogenation energies. The reaction energy $\Delta_r E$ of this reaction, Eq. 6.10, is given by,

$$\Delta_r E = E_{\mathrm{P}(-n\mathrm{H})(\mathrm{ad})} + \frac{n}{2} E_{\mathrm{H}_2} - E_{\mathrm{P}(\mathrm{ad})} \tag{6.11}$$

where $E_{\mathrm{P}(\mathrm{ad})}$ and $E_{\mathrm{P}(-n\mathrm{H})(\mathrm{ad})}$ are the total energies of the adsorbed P and P(-nH), respectively. The calculated values of $\Delta_r E$ for the dehydrogenation reactions resulting in the P(-H)(ad) shown in Figs. 6.7 and 6.8 for the top-like and the hollow sites, respectively, are tabulated and compared with the gas-phase values in Table 6.1. In the case of the formation of a C-Au bond, there is a large reduction of more than 1 eV of the dehydrogenation energy compared to the gas phase values. For hollow site, the calculated $\Delta_r E$ follows the trend between the dehydrogenation of edge and corner C atoms in the gas phase but the difference is smaller. In the case of the dehydrogenation of the edge C atom for the top site, where no C-Au bond is formed, the dehydrogenation energy is the same as in the gas phase.

6.4.4 P dimer formation

As in the gas-phase, the formation of the dimers on the Au(111) surface from two monomers can either involve the formation of single, double or triple C-C connections between the adsorbed P monomers as,

$$2\mathrm{P(ad)} \rightarrow \mathrm{P}(-n\mathrm{H})_2\mathrm{(ad)} + n\mathrm{H}_2 \tag{6.12}$$

where P(-nH)$_2$(ad) is the adsorbed P dehydrogenated by n H atoms and n = 1, 2 and 3 for single-, double-, and triple-connected dimers, respectively. The corresponding reaction energies of the formation of these dimers are then given by,

$$\Delta_r E = E_{\mathrm{P}(-\mathrm{nH})_2\mathrm{(ad)}} + nE_{\mathrm{H}_2} - E_{2\mathrm{P(ad)}} \tag{6.13}$$

where $E_{\mathrm{P}(-n\mathrm{H})_2\mathrm{(ad)}}$ is the total energy of the adsorbed n-connected dimer and $E_{2\mathrm{P(ad)}}$ is the total energy of two separated adsorbed P monomers. The latter energy was obtained in the calculations as $E_{2\mathrm{P(ad)}} = 2E_{\mathrm{P(ad)}} - E_{\mathrm{Au(111)}}$ where $E_{\mathrm{P(ad)}}$ is the energy of the adsorbed P monomer and $E_{\mathrm{Au(111)}}$ is the energy of the bare Au(111) slab.

There is a simple relation between reaction energies $\Delta E(\mathrm{ad})$ and $\Delta_r E(\mathrm{g})$ of the on-surface dimerization and gas-phase reactions, respectively. This difference is simply given by the difference of the adsorption energy of two P monomers and the P dimer as,

$$\Delta_r E(\mathrm{ad}) - \Delta_r E(\mathrm{g}) = 2E_{\mathrm{ad}}(\mathrm{P}) - E_{\mathrm{ad}}(\mathrm{P}(-n\mathrm{H})_2(\mathrm{ad})), \tag{6.14}$$

where $E_{\mathrm{ad}}(\mathrm{P}(-n\mathrm{H})_2(\mathrm{ad}))$ is the adsorption energy of a n-connected dimer defined in an analogous manner to the adsorption energy $E_{\mathrm{ad}}(\mathrm{P})$ of a P monomer in Eq.(6.7).

single-connected dimer

The geometric structures of the four configurations of the single-connected adsorbed dimers were calculated by starting from their geometries in the gas phase shown in Fig. 6.4. As shown in Fig. 6.9, the interactions of the dimers with surface changes their geometry structure due to the attraction to the surface. The average adsorption heights except for (ee) are about 3.3 Å and is similar to the physisorbed P monomer. In the case of (ee), the average adsorption height is 3.9 Å due to the large twist of the dimer. The calculated reaction energies, $\Delta_r E$, of the single-connected adsorbed P dimers were obtained from Eq.(6.12) ($n = 1$) and are shown and compared with the corresponding gas-phase values in Table 6.2. The trend over the different configurations except for the (ee) configuration is not changed upon adsorption but the energy difference between the configurations (cc) and (cc)' has increased significantly. A most notable result is the large increase of $\Delta_r E$ of about 1.8 eV for the (ee) dimer upon adsorption compared

to the increase of about 0.6 to 0.9 eV for the other configurations. This relatively large increase for the (ee) configuration can be understood from its relatively large average adsorption height and the associated decrease of adsorption energy compared to the other configurations. The increase of $\Delta_r E$ the other configurations upon adsorption simply reflects that the adsorption energies of these P dimers are less than twice that of the P monomer.

Double-connected dimers

Top views of the calculated configurations are shown in Fig. 6.10. The calculated reaction energies, $\Delta_r E$, of the adsorbed, double-connected dimers, as obtained from Eq. (6.13) for $n = 2$, are shown and compared with the corresponding gas-phase values in Table 6.2. Upon adsorption of the four gas-phase configurations of the double connected P dimers, the flat geometry of the P dimers did not change in the calculations and the adsorption height of 3.2 Å for all configuration except (cc)(ee) is very similar to the adsorption height of the P monomer. Due to the distortions of the H atoms of bonded to the corner C atom away from the molecular plane of the (cc)(ee) configuration, the average adsorption height is about 0.65 Å larger than the other configurations. This relatively large adsorption height causes a large increase of the reaction energy of about 1.4 eV compared to the other configurations. The reaction energies for the other configurations show the same trend as for the gas-phase values but have increased by about 0.4 eV for the same reason as for the single-connected dimers.

Triple-connected dimer

Also in this case upon adsorption of the triple-connected dimer, the flat geometry of the dimer did not change in the calculations and the adsorption height of 3.2 Å is also very similar to the adsorption height of the monomer and the double-connected dimers. The calculated geometric structure is shown in Fig. 6.10d). The calculated reaction energy, $\Delta_r E$, of the adsorbed, triple-connected dimers as obtained from Eq. (6.13) for $n = 3$ are shown and compared with the corresponding gas-phase values in Table 6.2. Also in this case, $\Delta_r E$ has also increased compared to its gas-phase value with about 0.49 eV, which is a slightly larger increase than 0.36-0.42 eV for the double-connected P dimer. This increase is probably in part due to the slight decrease in size when forming an additional C-C bond and the scaling of the van de Waals attraction with molecular size.

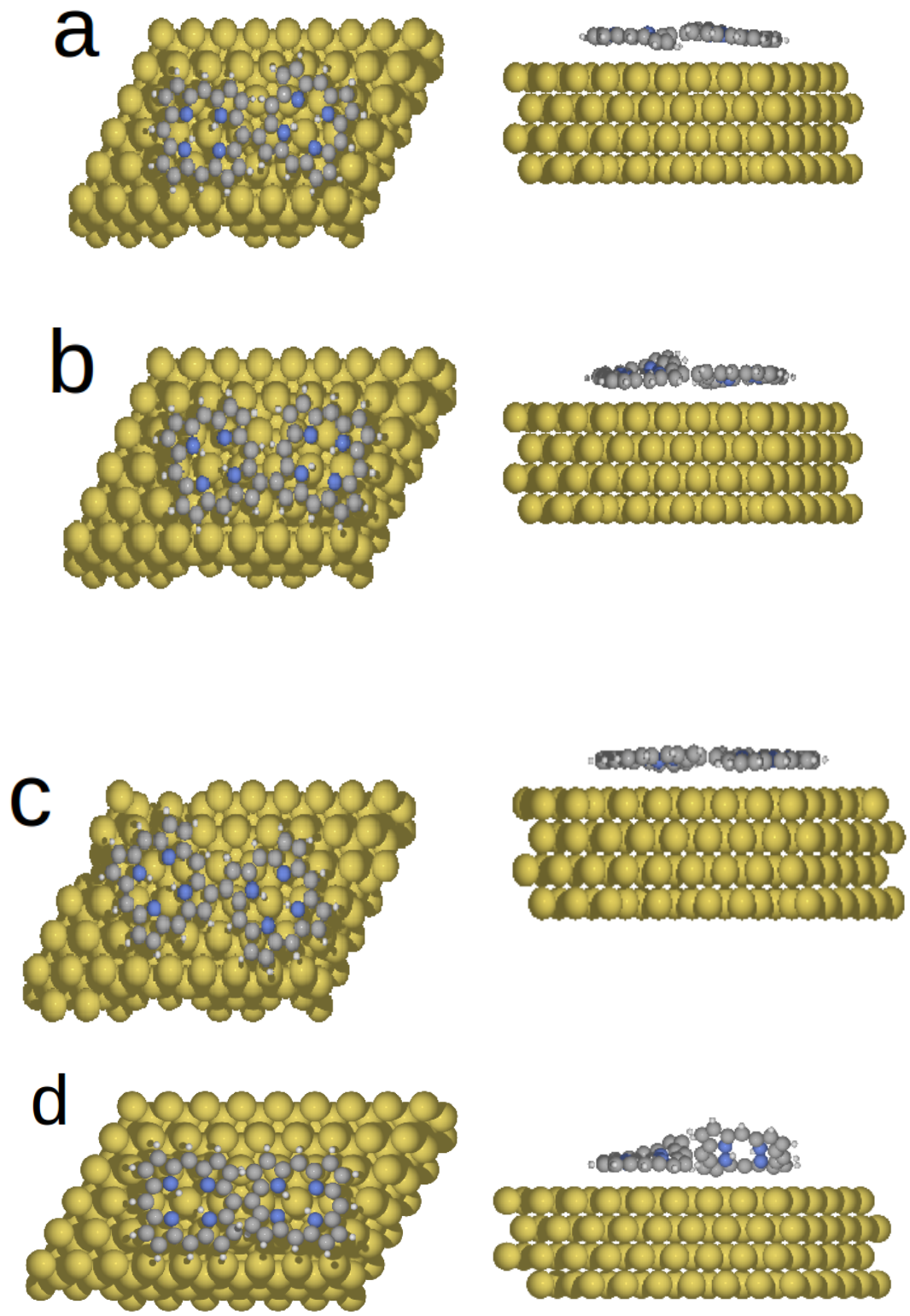

Figure 6.9: Top and side views of calculated equilibrium structures of the motifs a) (ec), b) (cc) and c) (cc)' of single-connected dimers adsorbed on Au(111).

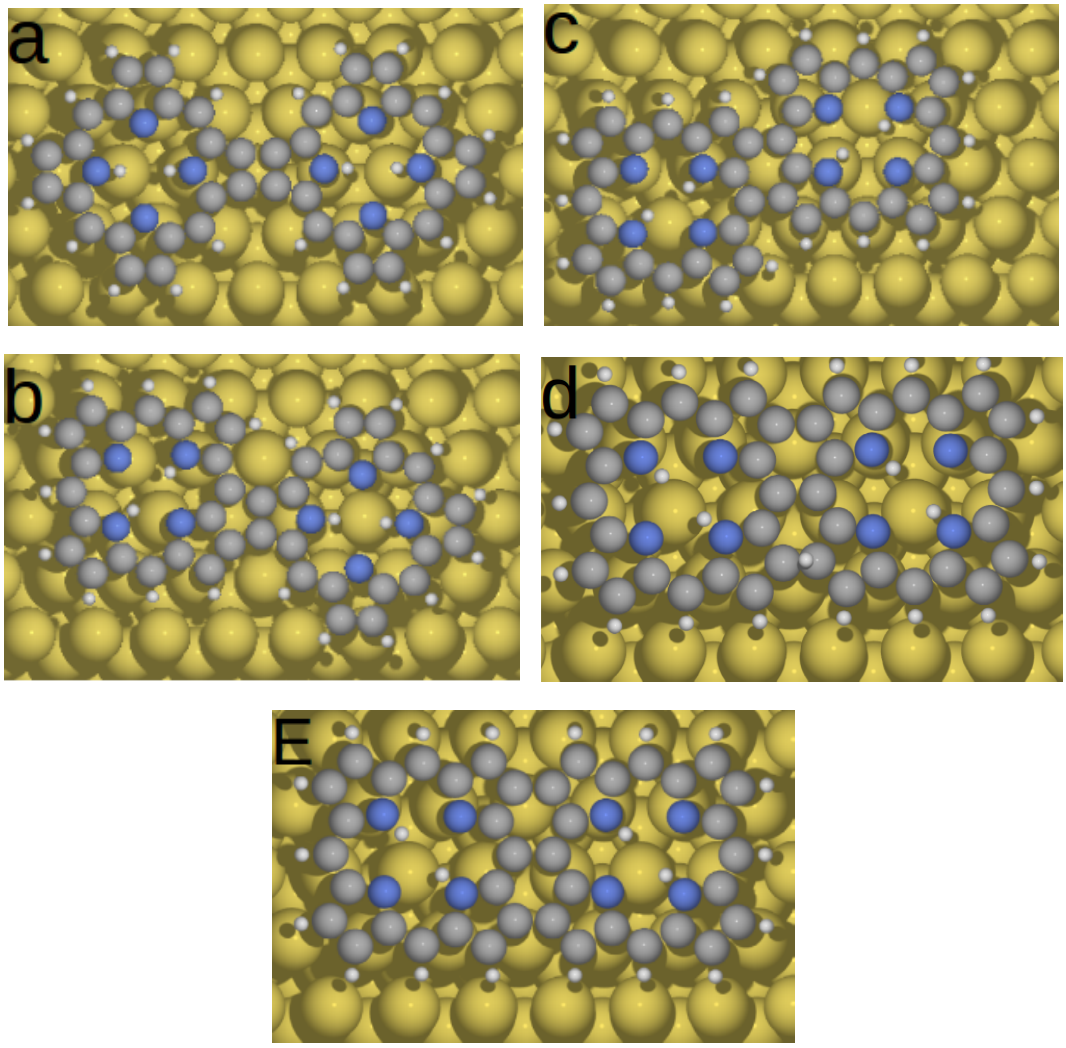

Figure 6.10: Top views of calculated structures of double-connected motifs a) $(cc)^2$, b) $(ce)^2$, c) (cc)'(ce) d) (cc)(ee) and triple-connected e) $(cc)^2$(ee) of dimers adsorbed on Au(111).

6.4.5 Free energy contributions

So far all calculations of reaction energies are based on potential energies, but Gibbs free energies are needed for a proper description of reaction thermodynamics. In addition to the potential energy term the free energy has also a contribution from vibrations, rotations and translations. In our case of C-H bond breaking and C-C bond making, we will assume that the contributions from vibrations to the internal energies and entropies of the reactants and the products more or less cancel each other. Thus, we will only keep the contribution from the translational and rotational motion.

As noted by Floris and coworkers [32], there will be a large contribution from the translational entropy of the hydrogen gas to the free energy in the temperature range

of interest 300 - 700K under ultrahigh vacuum conditions at a pressure of p = 10^{-7} Pa. In a simple ideal gas and rigid rotor model of the hydrogen molecule [108], they obtained $-TS$ = -1.8 to -2.2 eV per molecule for T = 500 - 600 K and $p = 10^{-7}$ Pa. In Figure 6.11, the contribution $\Delta\mu(\mathrm{H_2})$ to the calculated chemical potential $\Delta\mu(\mathrm{H_2})$ from the translational and the rotational motion is plotted as a function of temperature for three different ultralow pressures and also at the standard state pressure of 1 bar (see, the appendix of the chapter). The dominant contribution to $\Delta\mu(\mathrm{H_2})$ comes from the entropy of the translational motion.

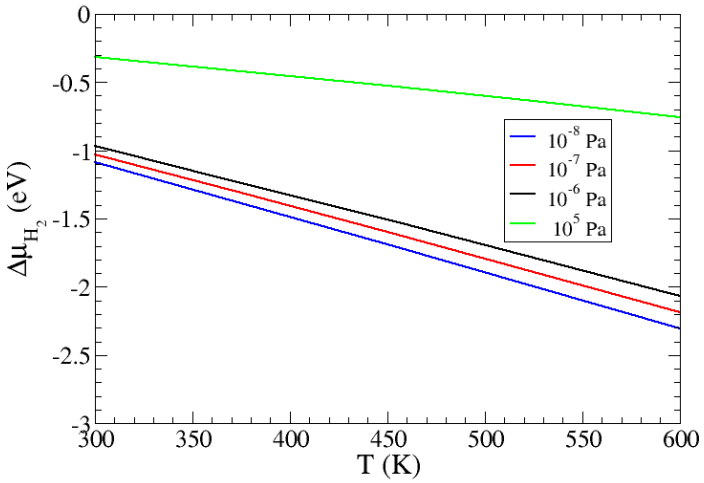

Figure 6.11: Translational and rotational contribution $\Delta\mu_{\mathrm{H_2}}$ to the chemical potential of $\mathrm{H_2}$ in the gas phase as a function of temperature T for a set of indicated pressures p.

There will also be a contribution from the translational and rotational motion to the reaction free energy for the adsorbed P monomers and dimers. Here these contributions are estimated by treating the adsorbed monomers and dimers as a 2D lattice gas or a 2D ideal gas. The lattice gas is appropriate for the dehydrogenated and chemisorbed P, whereas the 2D ideal gas is more appropriate for the physisorbed P and $\mathrm{P_2}$ at elevated temperatures.

As shown in appendix, the low-surface density dependence, of the chemical potential contribution of the 2D lattice and ideal 2D gases, $n_{2\mathrm{D}} \ll n_0$ where n_0 is mono-layer surface density, can both be expressed as,

$$\Delta\mu = \Delta\mu^{\dagger} + k_B T \ln\left(\frac{n_{2\mathrm{D}}}{n^{\dagger}_{2\mathrm{D}}}\right) \ , \tag{6.15}$$

Here $n^{\dagger}_{2\mathrm{D}}$ is the standard-state value for the surface density proposed by Campbell et

		P(ad)	P(-H)$_2$(ad)			
	T (K)		(cc)	(cc)'	(ce)	(ee)
$\Delta\mu^{\dagger}_{2D-g}$ (eV)	300	-0.64 (-0.44)	-0.68 (-0.45)	-0.67 (-0.45)	-0.69 (-0.45)	-0.69 (-0.45)
	500	-1.15 (-0.78)	-1.20 (-0.79)	-1.17 (-0.79)	-1.20 (-0.79)	-1.20 (-0.79)
	700	-1.65 (-1.12)	-1.73 (-1.14)	-1.68 (-1.14)	-1.73 (-1.14)	-1.73 (-1.14)
		P(-2H)$_2$(ad)				P(-3H)$_2$(ad)
		(cc)^2	(cc)'(ce)	(ce)^2	(cc)(ee)	(cc)^2(ee)
$\Delta\mu^{\dagger}_{2D-g}$ (eV)	300	-0.69 (-0.46)	-0.70 (-0.46)	-0.69 (-0.46)	-0.70 (-0.46)	-0.69 (-0.46)
	500	-1.19 (-0.80)	-1.22 (-0.80)	-1.19 (-0.80)	-1.22 (-0.80)	-1.19 (-0.80)
	700	-1.71 (-1.15)	-1.75 (-1.15)	-1.71 (-1.15)	-1.75 (-1.15)	-1.71 (-1.15)

Table 6.4: Calculated standard state values, $\Delta\mu^{\dagger}_{2D-g}$, of the chemical potential contribution from the translational and rotational motions of the various motifs of the P monomers and dimers in the adsorbed phase at three different temperatures. Values within the parentheses correspond to the contribution from the translational motion only.

al [111] (see, appendix of this chapter): $n^{\dagger}_{2D}$ = 0.117 – 0.0663 nm^{-2} at T = 300 – 700 K. The corresponding standard-state values for translational and rotational contributions to chemical potential for the 2D lattice and ideal gas are given by,

$$\Delta\mu^{\dagger}_{2D-l} = k_B T \ln\left(\frac{n^{\dagger}_{2D}}{n_0 N_{deg}}\right) \tag{6.16}$$

and

$$\Delta\mu^{\dagger}_{2D-g} = k_B T \ln\left(\frac{n^{\dagger}_{2D}}{q^{\dagger} q_R}\right) , \tag{6.17}$$

respectively. Here N_{deg} is the orientational degeneracy of the chemisorbed, dehydrogenated P and $q^{\dagger}$ and q_R are classical partition functions of the 2D rotational and translational motion, respectively, of the physisorbed P monomers and dimers as defined in correlated appendix.

In the case of the 2D lattice gas of monomers, when assuming a three-fold orientational degeneracy (N_{deg} = 3) and $n_0 \approx$ 0.03 Å^2 (based on dense-packing density), $\Delta\mu^{\dagger}_{2D-l}$ = -0.15 – -0.37 eV, in the temperature range, T = 300 – 700 K of interest. In the case of the 2D ideal gas, the calculated values of $\Delta\mu^{\dagger}_{2D-g}$ for T=300 and 600 K are shown in Table 6.4 for the various adsorbed P monomers. The values of $\Delta\mu^{\dagger}_{2D-g}$ for the various adsorbed P monomers and dimers are very similar with a significant contribution from the rotational motion: $\Delta\mu^{\dagger}_{2D-g}$ = -0.64 —0.70 eV and -1.40 – -1.50 eV at 300 and 600 K, respectively.

In the case of the dehydrogenation reaction, Eq. (6.10), and for a fixed pressure p_0 of the hydrogen gas, the reference value of the reaction Gibbs energy per molecule will then according to Eqns.(6.16) and (6.17) be given by,

$$\Delta_r G^\dagger = \Delta_r E + \Delta G^\dagger_{\rm dehyd} + \frac{n}{2}\Delta\mu_0({\rm H}_2) \tag{6.18}$$

where

$$\Delta G^\dagger_{\rm dehyd} = \Delta\mu^\dagger_{\rm 2D-l} - \Delta\mu^\dagger_{\rm 2D-g}({\rm P}(-{\rm nH})({\rm ad}))\ . \tag{6.19}$$

and $\Delta\mu_0({\rm H}_2)$ is the chemical potential contribution at pressure p_0 of the hydrogen gas. The calculated values for $\Delta G^\dagger_{\rm dehyd}$ at 300, 500 and 700 K are shown in Table 6.6. From Eq. (6.10), one now obtains the following chemical equilibrium equation for the surface densities of the P admonomer and the dehydrogenated admonomer at fixed pressure p_0 of the hydrogen gas,

$$\frac{n_{\rm 2D}[{\rm P}(-n{\rm H})({\rm ad})]}{n_{\rm 2D}[{\rm P}({\rm ad})]} = \exp\left(-\frac{\Delta_r G^\dagger}{k_B T}\right) \tag{6.20}$$

In the case of the dimerization reaction, Eq. (6.12), and for a fixed pressure p_0 of the hydrogen gas, the reference value of the reaction Gibbs energy per molecule will then according to Eqns.(6.16) and (6.17) be given by,

$$\Delta_r G^\dagger = \Delta_r E + \Delta G^\dagger_{\rm dimer} + n\Delta\mu_0({\rm H}_2) \tag{6.21}$$

where

$$\Delta G^\dagger_{\rm dimer} = \Delta\mu^\dagger_{\rm 2D-g}({\rm P}_2({\rm ad})) - 2\Delta\mu^\dagger_{\rm 2D-g}({\rm P}({\rm ad})) \tag{6.22}$$

The calculated values for $\Delta G^\dagger_{\rm dimer}$ at 300, 500 and 700 K are shown in Table 6.6. Note that the From Eq. (6.21), and one now obtains the chemical equilibrium equation for the surface densities of the P admonomer and the addimer at fixed pressure p_0 of the hydrogen gas,

$$\frac{n_{\rm 2D}[{\rm P}(-n{\rm H})_2({\rm ad})]n^\dagger_{\rm 2D}}{n_{\rm 2D}[{\rm P}({\rm ad})]^2} = \exp(-\frac{\Delta_r G^\dagger}{k_B T})\ . \tag{6.23}$$

In order to make a comparison between the reactions in the adsorbed and gas-phase, we have also calculated the free energy contributions from the translational and rotational motions of the P monomers and dimers in the gas phase. As shown in appendix of the chapter, The corresponding standard state values for translational and rotational contributions to chemical potential for the 3D ideal gas are given by,

$$\Delta\mu^\dagger_{\rm 3D-g} = -k_B T\ln(q^\dagger_T q_R)\ , \tag{6.24}$$

respectively. Here $q^\dagger_T$ and q_R are the classical partition functions of the 3D rotational and translational motion, respectively of the P monomers and dimers. As shown in

		P(g)	P(-H)$_2$(g)			
	T (K)		(cc)	(cc)'	(ce)	(ee)
$\Delta\mu^{\dagger}_{3D-g}$ (eV)	300	-0.88 (-0.50)	-1.00 (-0.52)	-0.98 (-0.52)	-1.00 (-0.52)	-0.98 (-0.52)
	500	-1.55 (-0.88)	-1.75 (-0.93)	-1.72 (-0.93)	-1.75 (-0.93)	-1.71 (-0.93)
	700	-2.25 (-1.29)	-2.53 (-1.35)	-2.50 (-1.35)	-2.53 (-1.35)	-2.48 (-1.35)
		P(-2H)$_2$(g)				P(-3H)$_2$(g)
		(cc)^2	(cc)'(ce)	(ce)^2	(cc)(ee)	(cc)^2(ee)
$\Delta\mu^{\dagger}_{3D-g}$ (eV)	300	-0.96 (-0.52)	-0.98 (-0.52)	-0.98 (-0.52)	-0.98 (-0.52)	-0.96 (-0.52)
	500	-1.69 (-0.93)	-1.75 (-0.93)	-1.72 (-0.93)	-1.71 (-0.93)	-1.68 (-0.93)
	700	-2.45 (-1.35)	-2.53 (-1.35)	-2.49 (-1.35)	-2.48 (-1.35)	-2.44 (-1.35)

Table 6.5: Calculated standard state values, $\Delta\mu^{\dagger}_{3D-g}$, of the chemical potential from the translational and rotational motions of the various motifs of the P monomers and dimers in the gas phase at three different temperatures. Values within the parentheses correspond to the contribution from the translational motion only.

Table 6.5, the calculated values $\Delta\mu^{\dagger}_{3D-g}$ for the various P monomers and dimers are very similar with a large contribution from the rotational motion: $\Delta\mu^{\dagger}_{3D-g}$ = -0.88 – -0.98 eV and -2.25 – -2.53 eV at 300 and 700 K, respectively. These values for $\Delta\mu^{\dagger}_{2D-g}$ are substantially larger than in the adsorbed phase due to the more confined motion in the adsorbed phase compared to the gas phase. The corresponding values for $\Delta G^{\dagger}_{\rm dehyd}$ and $\Delta G^{\dagger}_{\rm dimer}$ are shown in Table 6.6. Note that in the gas-phase, we use the standard state value of 1 bar for p_0 when obtaining the reaction free energies in the gas-phase from Eqns. 6.18 and 6.22.

6.4.6 Calculated STM images of adsorbed P dimers

In the experiments, the assignments of the different bonding motifs of the adsorbed dimers were based on an analysis of STM images. Thus, it is of interest to calculate STM images of the different bonding configurations of the addimers and to see to what extent they can be discriminated from their appearances. In Figs. 6.12 and 6.13, we present the calculated STM images of single-connected and multiple-connected addimers, respectively. These topographical images were calculated at a constant local density of states at a sample bias of 0.5 eV and the tip apex-surface distance was about 11 Å away from the molecule. The shape of these images clearly reflect the geometrical

T (K)	$\Delta G^{\dagger}_{\mathrm{dehyd}}$	$\Delta G^{\dagger}_{\mathrm{dimer}}$
	(ad)	
300	0.55	0.63±0.01
500	0.95	1.10±0.03
700	1.36	1.59±0.04
	(g)	
300	-0.03	0.77±0.02
500	-0.05	1.38±0.04
700	-0.06	2.00±0.05

Table 6.6: Calculated standard state values, $\Delta G^{\dagger}_{dehyd}$ and $\Delta G^{\dagger}_{dimer}$, of the change in chemical potential for the dehydrogenation and dimer reactions in the adsorbed and the gas phase. The error bars indicates the variation of the values for the different dimer motifs.

shape of the molecules with a depression in the centre of the molecules. The C-C bonds between the monomers show up as characteristic protrusions from which the number of C-C bonds between the monomers can be distinguished in most cases. Except for the motifs (cc)' and $(cc)^2$, all the other different bonding configurations can be discriminated from the shape of the STM images and the characteristic protrusions from the C-C bonds between the monomers.

6.5 Discussion of dimer formation reaction

Based on our calculated reaction energies for the dehydrogenation and dimerization reactions and the estimated free-energy contributions from translational and rotational motion, we will now begin by discuss the thermodynamics and kinetics of these reactions in the adsorbed phase and the gas phase. In Figs. 6.14 and 6.16, we show the calculated reaction free energies $\Delta_r G^{\dagger}$ of these gas-phase and on-surface reactions, respectively, at three different temperatures. In the case of the gas-phase reactions, $\Delta_r G^{\dagger}$ were calculated using the standard state value 1 Bar of the hydrogen pressure whereas for the on-surface reactions the pressure was 10^{-7} Pa corresponding to a typical hydrogen pressure in the vacuum chamber. In order to make a more direct comparison between the reaction free energies for the gas-phase and on-surface reaction, we also show in Fig. 6.15 the reaction free energies $\Delta_r G$ in the hypothetical situation that the hydrogen pressure is kept at 10^{-7} Pa. Note that at zero-temperature there is only a contribution to $\Delta_r G^{\dagger}$ from the reaction energy $\Delta_r E$: $\Delta_r G^{\dagger} = \Delta_r E$.

In the gas phase at the standard state pressure of the reactants and the products, $\Delta_r G^\dagger$ is positive for all the dehydrogenation and dimerisation reactions except for the triple-connected dimer at the highest temperature of 700 K. Furthermore, $\Delta_r G^\dagger$ decreases only for the formation of the triple-connected dimer with increasing temperature due to the fact that the decrease in entropy from the formation of the hydrogen gas does not compensate the decrease in entropy in the formation of the single-connected and double-connected dimers from two monomers. In contrast to the dimerisation reaction, the entropy change between the monomer and the dehydrogenated monomer is very small and the decrease of $\Delta_r G^\dagger$ with temperature is governed by the increase of entropy for the hydrogen gas.

The behaviour of $\Delta_r G^\dagger$ with temperature for the on-surface dimerisation reactions are dramatically different from the gas-phase reactions at standard state pressure for the reactants and products primarily due to the ultra-low pressure of the hydrogen gas. This effect is demonstrated by the calculated reaction free energies in the gas phase when the hydrogen pressure is kept artificially at the same ultra-low pressure as for the on-surface reactions. As discussed before in Section 6.4.3, the values of $\Delta_r G^\dagger$ at zero temperature shows that the $\Delta_r E$ of the dehydrogenation reactions decrease substantially on the surface suggesting that this reaction is catalyzed by the surface whereas $\Delta_r E$ of the dimerization reactions actually increase upon adsorption suggesting that these reactions are not catalyzed on the surface. $\Delta_r G^\dagger$ for the dimerization reactions show a rapid decrease with temperature especially for the multiple-connected dimers. This decrease is caused by the large contribution to the entropy of the hydrogen gas kept at a pressure of 10^{-7} Pa and this effect become increasingly important with the number of C-C bonds formed. The decrease of the entropy due to the formation of dimers from two monomers is smaller for the on-surface reaction than for the gas-phase reaction due to the reduced dimensionality. This decrease is not able to compensate for the increase of entropy in the formation of the hydrogen gas. Due to this increase the formation of the single-connected (cc)' motif, the double-connected $(ce)^2$ and (cc)'(ce) motifs and the triple-connected $(cc)^2(ee)$ motif are thermodynamically feasible at elevated temperatures and even the double-connected (cc)(ee) is feasible at 700 K.

The behaviour of the reaction free energies for the on-surface reactions would suggest that at elevated temperatures triple-connected dimers would be exclusively formed. However, this conclusion rests on the assumption that these reactions are in chemical equilibrium. In particular, the key thermodynamic driving force behind on-surface dimer formation is based on the assumption that the adsorbed H atoms being in chemical equilibrium with the hydrogen gas. Using the calculated value of 0.76 eV

for the barrier height of the H desorption reaction, the Arrhenius-like expression of classical transition state theory [108] for the reaction rate supports that the adsorbed H atoms are in chemical equilibrium with the hydrogen gas. In Fig. 6.17, we show the rates k as a function of temperature T and free energy barriers, where the rates are given by the Eyring equation [112],

$$k = \frac{k_B T}{h} \exp\left(-\frac{G_{\mathrm{B}}}{k_B T}\right) \tag{6.25}$$

and G_{B} is the free-energy barrier. As shown in Fig. 6.17, k for the hydrogen desorption is larger than $1/\mathrm{s}$ when $T > 300$ K and assuming G_{B} = 0.76 eV. We have not attempted to calculate any barrier for the various reaction pathways but our calculated reaction free energies give indirectly some important information about the reaction barriers.

In order to ease the discussion of possible on-surface reaction pathways and their barriers for dimer formation, we show in Fig. 6.18 those pathways that involve single C-C connection or single dehydrogenations. The $\Delta_r G$ for the single dehydrogenation of the monomer gives a lower bound of about 1.8 eV for the energy barrier for the formation of a single-connected dimer by two sequential dehydrogenations followed by single C-C coupling. According to Fig. 6.17, this lower bound for the energy barrier suggests that this pathway is not viable in the temperature range 300 - 600 K. In fact, a recent study by [113] of graphene on a Au(111) surface have shown that the most favourable reaction pathway for the C-C connection is via a concerted double C-H connection breaking and a single C-C bond formation in which the H atoms ends up adsorbed on the surface. Thus this study suggests that the formation of the single-connected dimers could also follows the same reaction pathway.

Furthermore, the formation of $(cc)^2$ from (cc) by a single C-C connection can be ruled out by the lower bound of about 2 eV for the corresponding barrier set by the difference between $\Delta_r G$ for the formation of $(cc)^2$ and (cc). The results for $\Delta_r G$ shows that there are no such lower bounds for the barriers of formation by single C-C connection of $(ce)^2$ from (ce) and (cc)'(ce) from (cc)'.

A notable fact, as shown in Fig. 6.18, is the observation that $(cc)^2$(ee) can only be formed by a single C-C connection from the double C-C connection dimer (cc)(ee). However, the relatively large value of $\Delta_r G$ for this intermediate compared the other two intermediates $(ce)^2$ suggests the formation of $(cc)^2$(ee) should be suppressed but a firm conclusion requires a calculation of the reaction barrier between (cc)(ee) and $(cc)^2$(ee).

6.6 Comparison with experiments

The scanning tunneling microscopy (STM) experiments of the on-surface dimerization reactions of P monomers are still in progress by the groups at University of Liverpool and University of Graz lead by Raval and Grill, respectively. However, surface steps were shown to play a key role in the on-surface reaction studied by the Liverpool group in contrast to the study by the Graz group. Thus our discussion of the experimental results is still preliminary and will be limited to the data recorded by the Graz group.

The different bonding motifs of the dimers in the experiments were identified from the STM images. In Fig. 6.19, we show all the bonding motifs of dimers that were identified from the STM images. The motifs $(ce)^2$, (cc)'(ce) and $(cc)^2$(ee) are readily identified from these images, as corroborated by our calculated STM images in Figs. 6.12, 6.13. As discussed in Section 6.4.6, the bonding motifs (cc)' and $(cc)^2$ cannot easily be discriminated from the STM images so in this case our assignment is based on the fact that $\Delta_r G$ for $(cc)^2$ is too high to be formed on the surface, whereas $\Delta_r G$ of (cc)' is much more favourable and should be readily formed on the surface.

The statistics of the relative occurrence of the binding motifs at different surface temperatures as observed by the Graz and the Liverpool group are shown in Tables 6.7 and 6.8, respectively. The data by the Graz group was obtained by a deposition on the surface at constant flux of molecules and kept at the indicated temperatures followed by STM imaging at 5 Kelvin . In contrast, the data by the Liverpool group was obtained by deposition at room temperature followed by annealing to the indicated temperatures and the STM images were obtained after cooling down to room temperature. A rather surprising result is the large difference in statistics for the dimer formation recorded by the Graz and the Liverpool group. In particular, the much higher relative occurrence of the bonding motifs $(ce)^2$ and $(cc)^2$(ee) observed by the Liverpool group than for the Graz group but is tentatively attributed to the key role played by the steps on the surface.

The statistics by the Graz group can be rationalized by our (free) energy calculations for dimerization reactions. The decrease of surface density of adsorbed molecules with temperature is simply caused by thermal desorption. The calculated adsorption energies of the dimers are about twice as large the calculated monomer adsorption energy of about 2.8 eV. (Section 6.4.1). This selective desorption of monomers is then in part responsible for the increased reacted fraction of monomers with temperature. Under the prevailing conditions, the reaction is obviously kinetically constrained since in chemical equilibrium, one would expect the exclusive formation of triple-connected dimers at elevated sample temperatures. However, the observation of only single-

Dimer	T (K)				
	523	573	623	673	723
(cc)′	69	67	10	4	4
(cc)′(ce)	31	31	80	94	96
$(ce)^2$	0	2	10	1	0
$(cc)^2(ee)$	0	0	1	2	0
Reacted	2	3	22	26	27
n_{2D} (nm^{-2})	0.412	0.485	0.345	0.275	0.049

Table 6.7: Relative occurrence of different binding motifs and reacted molecules, and surface densities, n_{2D}, for each sample after molecule deposition at the indicated sample temperatures T. The data was obtained by the Graz group.

connected (cc)′ motifs and no other single-connected motifs is corroborated by $\Delta_r G$ of (cc)′ being smaller with more than 0.25 eV than the other single connected motifs. Furthermore, the formation of only double-connected (cc)′(ce) motifs and no double-connected $(ce)^2$ motifs at the lower temperatures can be understood from the fact that (cc)′(ce) and $(ce)^2$ motifs motifs can only be formed by single C-C connection from the (cc)′ and (ce) motifs, respectively (Fig. 6.18). The (cc)′ motifs will then be depleted at higher temperatures due to $\Delta_r G$ becomes more favourable for formation of (cc)′(ce) motifs compared to the (cc)′ motifs. The $(ce)^2$ motif is the most favourable double-connected motif based on the calculated $\Delta_r G$ but can only be formed by single C-C connection via the reaction intermediate (ce) which has a substantially higher $\Delta_r G$ than the (cc)′ motif. Thus this bottleneck rationalizes the much lower occurence of the $(ce)^2$ motif compared to the (cc)′(ce) motif. Finally, the strong suppression of the formation of the triple-connected $(cc)^2(ee)$ motif despite being the most thermodynamically favourable one can be rationalized by this motif can only formed by single C-C connection from the (cc)(ee) motif which has a relatively large $\Delta_r G$ compared to the other double-connected motifs except $(cc)^2$.

6.7 Summary

In this Chapter, we have presented a density functional theory (DFT) study of the on-surface dimerization of porphine (P) monomers adsorbed on the Au(111) surface by single, double and triple C-C connection. This study was motivated by recent STM experiments of this reaction under ultra-high vacuum condition. The P monomers and dimers are found to be physisorbed on the surface. The energy hierarchy of the different double-connected dimer motifs can be simply be understood from the increase

Dimer	T (K)			
	573	613	633	653
(cc)'	6%	12%	13%	8%
(cc)'(ce)	56%	54%	30%	52%
$(ce)^2$	18%	17%	27%	20%
$(cc)^2(ee)$	20%	17%	30%	19%
n_{2D} (nm^{-2})	0.34	0.38	0.24	0.2

Table 6.8: Relative occurrence of different binding motifs and reacted molecules, and surface densities, n_{2D},for each sample after molecule deposition annealing at the indicated sample temperatures T. The data was obtained by the Liverpool group.

of strain energy when forming four-, five- and six-membered C rings. The on-surface reaction energy for the formation of the dimers from the monomers follows the calculated trend for the corresponding energies in the gas-phase. In fact, the reaction energies are larger on the surface than in the gas-phase due to the adsorption energies of the dimers were less than twice the adsorption energy of the monomer and the physisorption disfavours the formation of non-planar dimers. In contrast, the dehydrogenation of the P monomers is catalyzed by the surface and the dehydrogenated monomer form a chemisorption bond with the surface. However, the formation energy of the dehydrogenated monomer is argued to be too large for acting as a reaction intermediate in the formation of the single-connected dimers of interest in the experiments. These dimers are instead argued to be formed by a concerted dehydrogenation of the two monomers and C-C bond formation.

The free energy contributions from the translational and rotational motion of the monomers and the dimers and of the hydrogen gas were also included in the study of the thermodynamics of the dimerization and dehydrogenation reactions. In particular, the high entropy from the translational motion of the low-pressure hydrogen gas in the vacuum chamber corresponding to a large negative chemical potential was found to be a key thermodynamic driving force behind the on-surface dimerization reaction. This conclusion is based on the fact that the hydrogen gas was found is expected to be in chemical equilibrium with the adsorbed H atoms at the temperatures of interest in the experiments from the calculated energy barrier for H desorption. In contrast, the formation of single-connected and double-connected dimers was not found to be feasible in the gas-phase under the standard state and the formation of triple-connected dimers was only feasible at the highest temperature. The entropy contributions from the translational and rotational motions of the monomers and the dimers are not negligible especially in the gas-phase. In particular, the decrease of the entropy in the gas

phase when forming a dimer from two monomers increases the reaction energies but less so on the surface due to its reduced dimensionality.

Our study is able to rationalize the experiments by the scanning tunnelling microscopy (STM) group at the University of Graz lead by Grill. Our calculated STM images corroborate their assignment of the different dimer bonding motifs from the observed STM images. In particular, the discrimination between single-connected and double-connected dimer motifs formed by coupling between corner C atoms are resolved by our calculated reaction energies. The calculated reaction energies also rationalizes why only one of the possible single-connected dimers are observed. The prevalence of a double-connected motif over a double-connected motif with a smaller energy is explained by kinetics and the possible single C-C connection reaction pathways. The latter motif has a single-connected reaction intermediate with higher energy than the former motif. The rare occurences of the triple-connected dimer despite being largely favoured by the chemical potential of the hydrogen gas in the vacuum chamber can be reconciled by its formation requires a single C-C connection from a double-connected intermediate with a relatively large free energy.

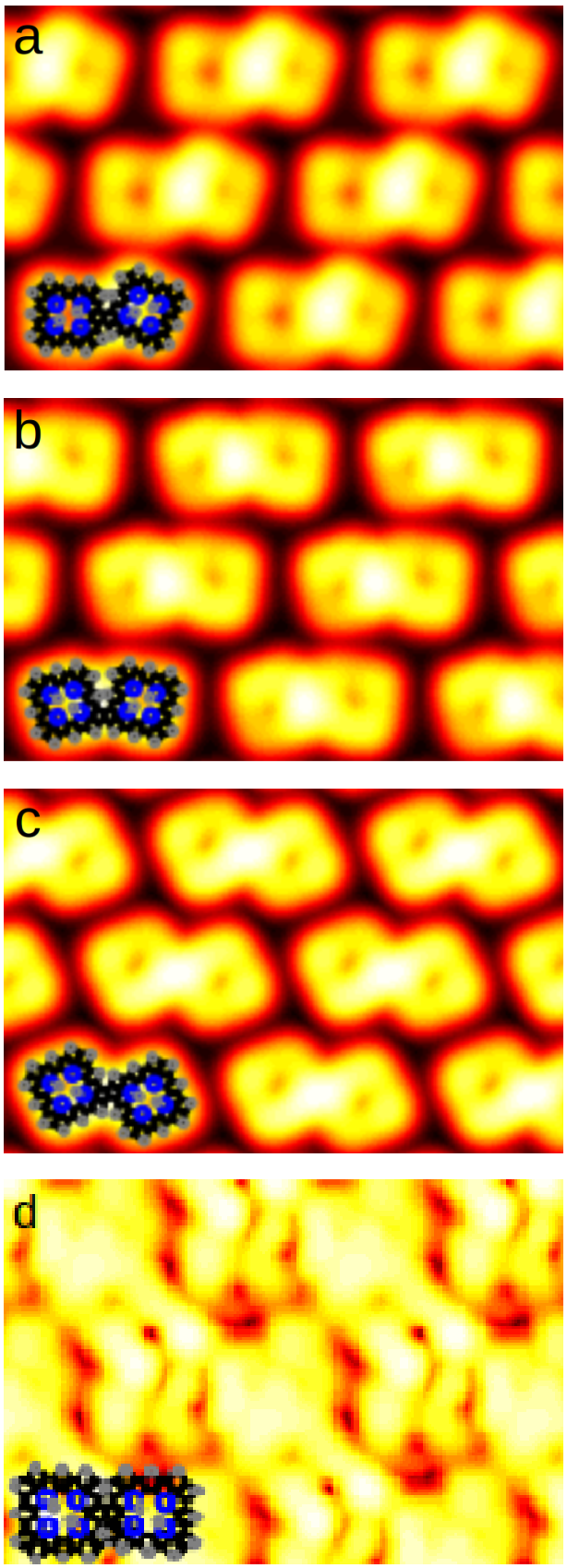

Figure 6.12: Calculated topographic STM images of the single-connected motifs a) $M_{(ce)}$, b) $M_{(cc)}$, c) $M'_{(cc)}$ and d) $M'_{(ee)}$ of adsorbed dimers on Au(111).

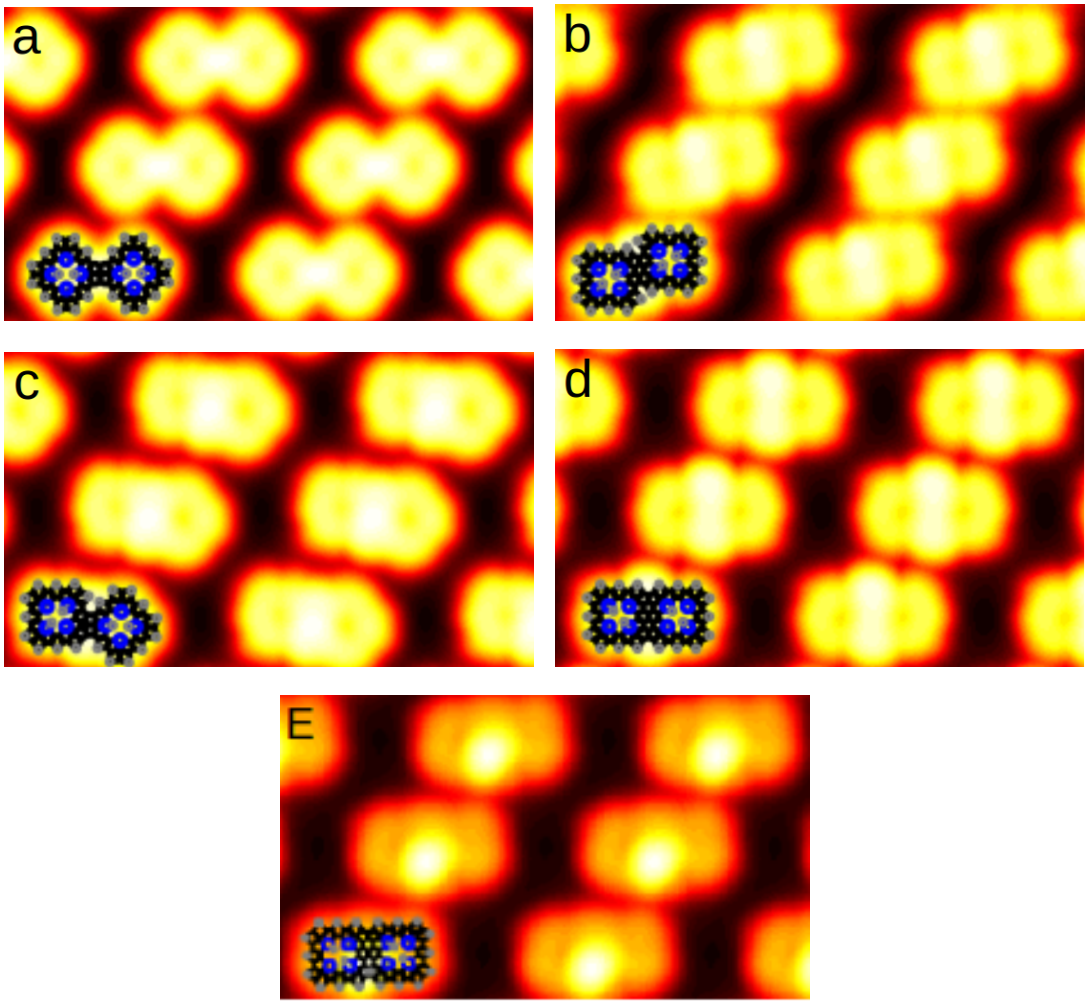

Figure 6.13: Calculated topographic STM images of the double-connected and the triple-connected motifs a) $(cc)^2$, b) $(ce)^2$, c) (cc)'(ce), d) $(cc)^2(ee)$, and e) (cc)(ee) of adsorbed dimers on Au(111).

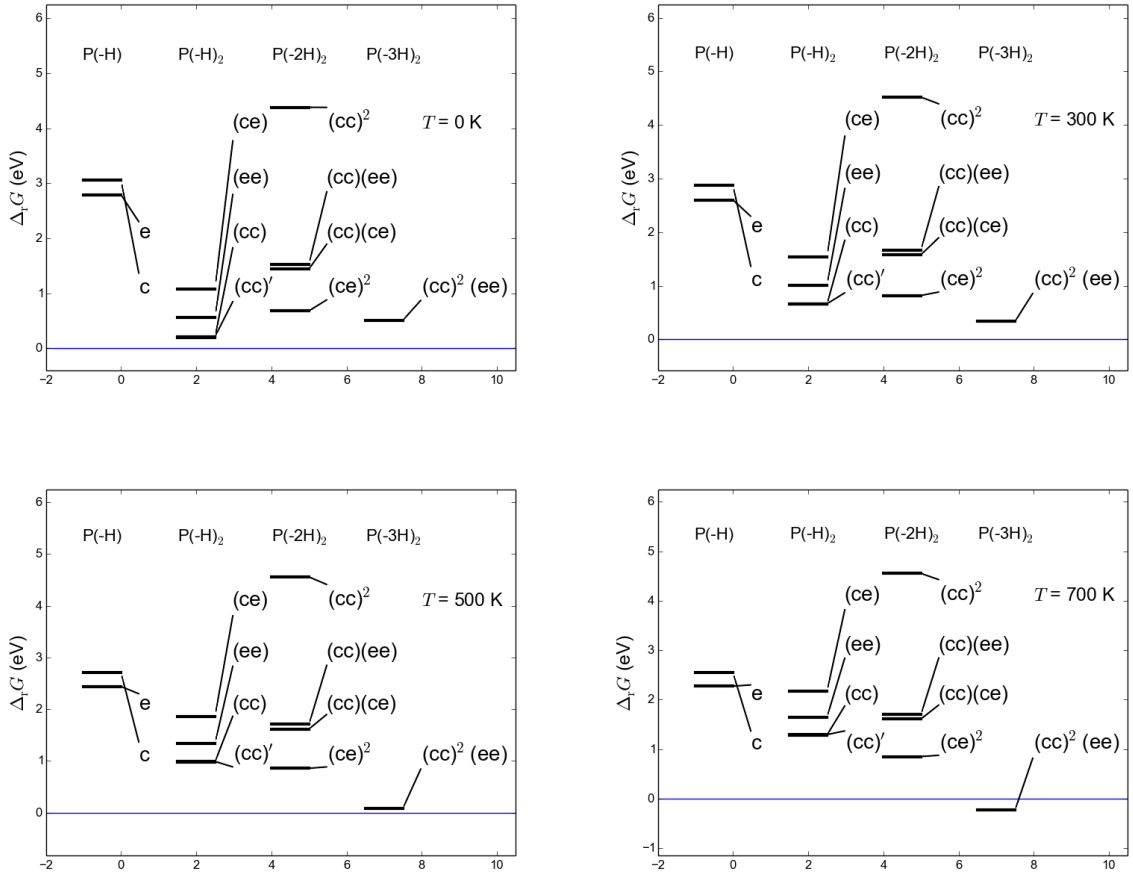

Figure 6.14: Reaction free energies, $\Delta_r G^{\dagger}$, for the dehydrogenation and dimerisation reactions in the gas-phase at four different temperatures T.

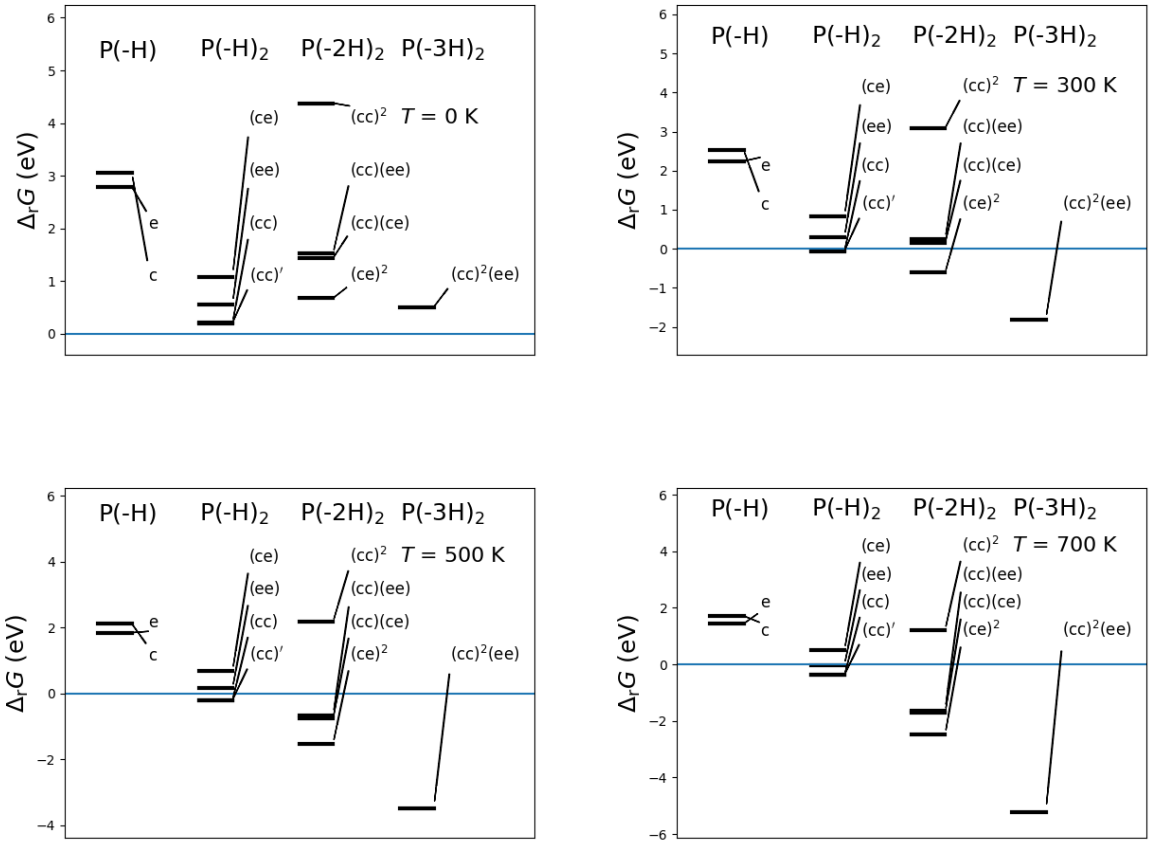

Figure 6.15: Reaction free energies, $\Delta_r G$, for the dehydrogenation and dimerisation reactions in the gas phase at four different temperatures T when the hydrogen pressure is kept artificially at 10^{-7} Pa. The pressure of the monomers and dimers is still at the standard state pressure of 1 bar.

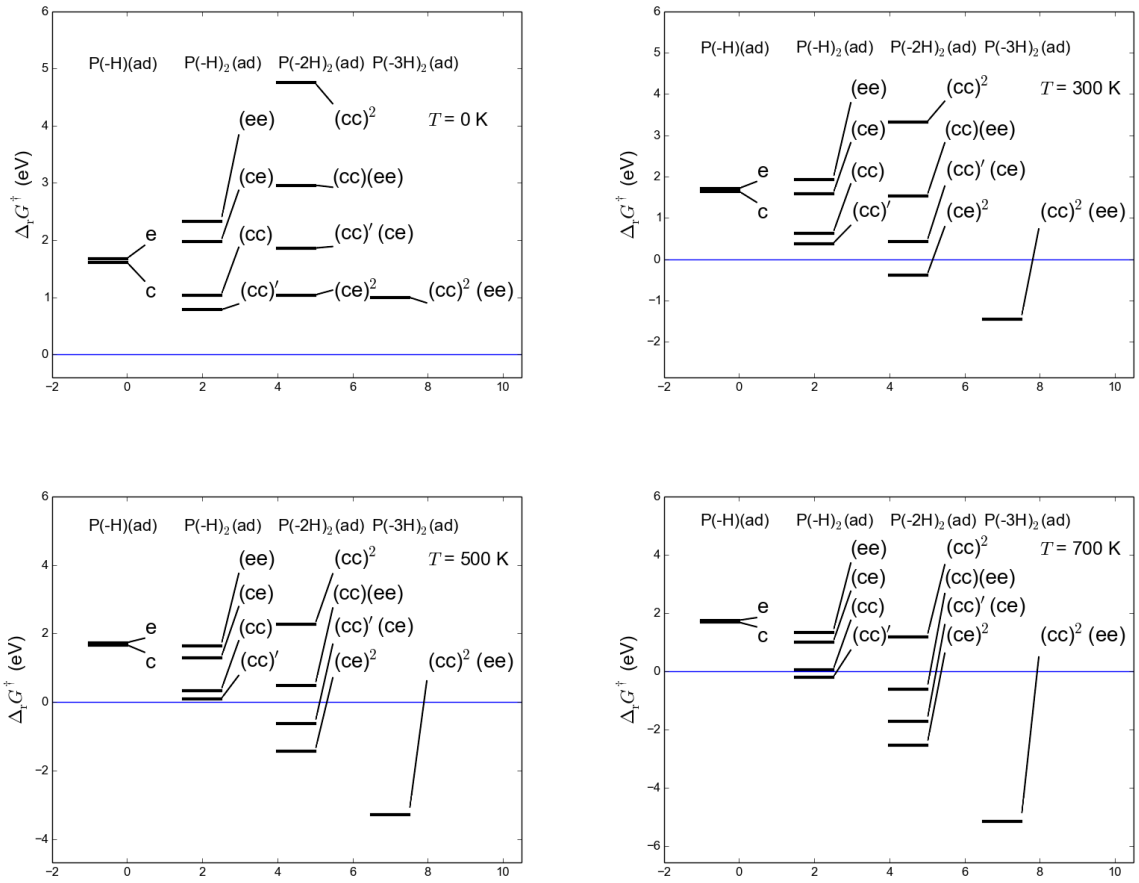

Figure 6.16: Reaction free energies, $\Delta_r G^\dagger$, for the on-surface dehydrogenation and dimerisation reactions at four different temperatures T

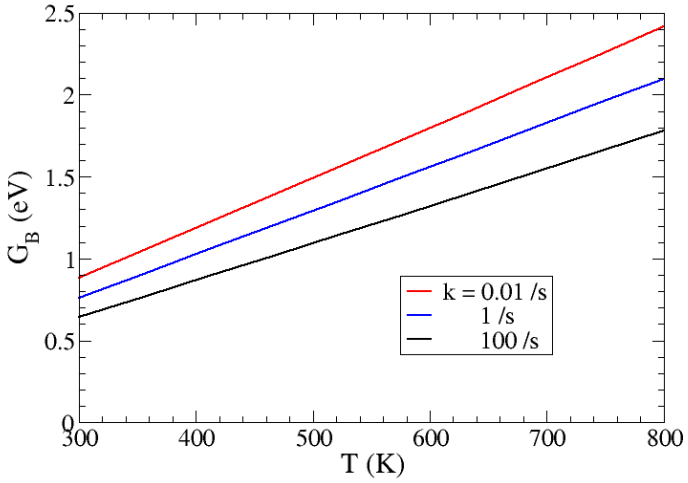

Figure 6.17: Free energy barriers, G_{B}, as function of temperature T for a fixed rate k.

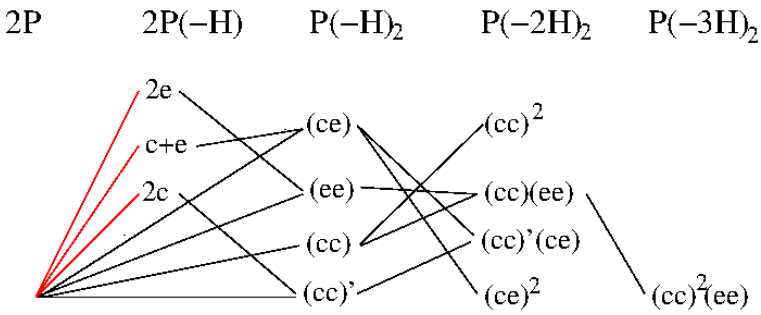

Figure 6.18: Reaction pathways for forming single-, double and triple-connected dimers by single C-C connection (black lines) and for single dehydrogenations (red lines).

Figure 6.19: STM images of observed P dimer motifs on the Au(111) surface. Starting from left hand-side they are assigned to correspond to (cc)',(ce)^2,(cc)'(ce) and (cc)^2(ee) motifs. Note that the (cc)' and the (cc)^2 motif were discrimated by the latter having much larger formation energy than the former. The date was obtained by the Graz group.

Chapter 7

Concluding remarks and outlook

This thesis is concerned with density functional theory (DFT) calculations of porphyrin molecules adsorbed on a copper surface and and coordinated to carbon monoxide molecules. The specific systems were motivated by experimental studies based on scanning tunnelling microscope (STM) of self assembly and on-surface reactions, and second harmonic generation of fundamental vibrations and overtones. The primary porphyrin molecules studied were ruthenium tetraphenyl porphyrin (RuTPP) and porphine (H_2-P) being the parent porphyrin molecule. As a comparison also the adsorption of two other metalled tetraphenyl porphyrins (MTPP) were also studied: M = Co and Zn. Below some concluding remarks are given and also an outlook for further studies.

7.0.1

Self assembly of MTPP on Cu(110) surfaces. The DFT calculations showed that the isolated RuTPP, CoTPP and ZnTPP have all considerable twist of the phenyl rings due to the strong steric hindrance between the phenyl rings but with the macro cycle left in a flat geometry. Upon adsorption, the phenyl rings tilts away from the surface which increases with the coverage. Also the twist of the phenyl groups are changed upon adsorption. The phenyl rings show up as characteristic protrusions in the calculated and measured STM images. The spin moments of RuTPP and CoTPP with partially filled d shell are quenched upon adsorption. The d shell of both isolated and asdorbed ZnTPP is found to be closed.

CO bonding on isolated and adsorbed MTPP on the Cu(110) surface. The DFT calculations showed that CO does not form a chemical bond with the metal centre of ZnTPP due to the closed d shell of the Zn atom. In contrast, CO forms a strong bond with the metal centres of the isolated and adsorbed RuTPP. The CO molecule

is bonded perpendicular to the macro cycle of RuTPP but is slightly tilted on Co-TPP. The CO adsorption energy on RuTPP is about the three and half times larger on CoTPP but is reduced by almost a factor two when adsorbed, whereas the CO adsorption energy changes only slightly between isolated and adsorbed CoTPP. The calculated CO adsorption energy on the bare Cu(110) surface lies in between the corresponding energies for adsorbed RuTPP and CoTPP and explains why CO bonding to the adsorbed MTPP is only observed for M=Ru. The calculated STM images corroborate that the CO molecule appears as a strong protrusion in the centre of the adsorbed RuTPP molecule. The calculated projected DOS on the frontier orbitals of the isolated and adsorbed RuTPP and CoTPP are in accordance with the Blyholder model corresponding to an electron donation from the 5σ CO orbitals into the metal and a back donation to the $2\pi*$ CO orbitals

Anharmonicity of the internal CO stretch. The anharmonicity of the internal CO stretch in various bonding situations was studied by DFT calculation of the potential energy curve for C-O distance. A direct comparison of the frequencies as obtained from a fit to a Morse potential or perturbation theory with the measured fundamental internal CO stretch frequencies and overtones was also made. The calculated values for the anharmonicity of the isolated CO and the adsorbed CO on Cu(110) were in good agreement with the experimental results at low coverages. The small decrease of the calculated anharmonicity with increasing CO coverage is understood from the decrease of the root-mean square amplitude of the CO vibration with increasing vibrational frequency due to dipole-dipole interactions. However, the calculated coverage shift of the fundamental C-O frequency is not observed in the experiments. The relatively large, anomalous value for the anharmonicity of the C-O stretch for CO adsorbed on RuTPP on Cu(110) was not reproduced in our calculations. However, the calculations reproduced the large red shift of the fundamental C-O frequency upon adsorption on RuTPP.

H_2-P dimer formation on Au(111). DFT calculations of the reaction energies for H_2-P dimer formation by single, double and triple C-C couplings and dehydrogenation in the gas phase and adsorbed on the Au(111) have been carried out. This study was motivated by on-going STM experiments of this on-surface reaction under ultra-high vacuum conditions. The H_2-P monomer and the various dimers were found to be physisorbed on the surface whereas dehydrogenation led to the formation of chemisorption bond. The physisorption bond favours the formation of planar dimers but the reaction energies are larger on the surface due to the physisorption energy for the

dimer is less than twice of that for the monomer. The formation of dimers with six-membered C rings were favoured over five- and four-membered C rings due to their higher strain energies. The free energy contributions from the translational and rotational motion of the reactants and the products in the gas phase and on the surface were also estimated. The large entropy of the formed hydrogen gas kept at an ultra-low pressure made the dimerisation on-surface reaction strongly exothermic and feasible at elevated temperature. The calculations are able to rationalise more or less the occurrences of the various dimer bonding motifs in the STM experiments. The calculated STM images were also useful in discriminating between the various dimer bonding motifs.

7.1 Outlook

This thesis has touched on essentially three areas of porphyrins adsorption on surfaces and is by no means a complete study. There are a number of avenues for further study. Here we will just give a few suggestions for future studies.

The self assembly of porphyrins on surfaces and their coordination to small molecules through their metal centres such as, for example CO and O_2, is an emerging field of study with potentially important ramifications for catalysis and nano technology. For example, there is a need for more systematic studies of CO coordination to metalated porphyrins and also the influence of the functionalisation by side groups.

The origin of the relatively large anharmonicity of the internal CO stretch of CO-RuTPP/Cu(110) is puzzling and is not clear from our DFT study. One probably needs to study more systems in order to see whether the calculations of this kind of anharmonicity is too demanding for DFT calculations or that we are missing some important physical mechanism.

The study of the on-surface, dimerisation reaction of H_2-P on the inert Au(111) surface has so far been limited to the reaction thermodynamics. In order to understand fully the kinetics of this reaction, it would be necessary to calculate reaction barriers. However, these calculations are very computationally challenging due to the large size of the systems and one needs to identify the key barriers among the relatively large number of possible barriers. Another interesting computational study but also very challenging would be the calculation of reaction energies and barriers at stepped surfaces. Recent STM experiments have shown that the distribution of bonding motifs is completely different in the presence of steps than on the terraces.

Appendix A

Chapter 2 and chapter 3

A.1 Dipole-dipole interaction

Here we present a short derivation of Eq.(5.23) for the effect of the dipole-dipole interaction on the harmonic vibrational frequency of the internal CO stretch at the Γ point for an ordered overlayer. The dipole-dipole interaction energy for an displacement u of the internal CO stretch mode is per molecule given by,

$$V_{\mathrm{dip-dip}} = \frac{(e^*)^2 U u^2}{2} \tag{A.1}$$

where e^* is the effective charge, defined as the slope of the calculated dipole moment with respect to u, and the dipole sum U is given by,

$$U = \sum_{\vec{R}\neq 0} \left(\frac{1}{R^3} + \frac{1}{(R^2+4d^2)^{3/2}} - \frac{12d^2}{(R^2+4d^2)^{\frac{5}{2}}} \right) \tag{A.2}$$

Here $\vec{R}$ are the 2D lattice vectors of the ordered overlayer and d is the distance between the dipole moment, assumed to be at the centre of the CO molecule, and the image plane. Note that dipole moment has no contribution from the image charge distribution located at the image plane.

The force constant for the internal stretch is now given by $4\pi^2\mu\nu_0^2$, where ν_0 is the harmonic frequency. Since the dipole-dipole interaction in Eq. (A.1 corresponds to a contribution $(e^*)^2U$ to the force constant, the force constant in the absence of the dipole-dipole interaction is then given by,

$$4\pi^2\mu(\nu_0 - \Delta\nu_0)^2 = 4\pi^2\mu\nu_0^2 - (e^*)^2 U \ , \tag{A.3}$$

where $\nu_0 - \Delta\nu_0$ is the harmonic frequency in the absence of dipole-dipole interactions. Finally, Eq. (5.23) follows directly from the result in Eq. (A.3).

A.2 Free-energy contributions

The contribution μ_{RT} from the rotational and translational motion of a molecule to the chemical potential of the ideal gas is given in terms of the corresponding classical partition functions q_T and q_R as [108],

$$\mu_{TR} = -k_B T \ln q_T q_R. \tag{A.4}$$

Here, q_T is the translational partition function of a molecule in the molecular volume and is given in d dimensions by,

$$q_T = \left(\frac{L}{L_{\mathrm{th}}}\right)^d \tag{A.5}$$

where L_{th} is the thermal de Broglie wavelength of the molecule with mass M,

$$L_{\mathrm{th}} = \sqrt{\frac{2\pi\hbar^2}{M k_B T}} \tag{A.6}$$

and L^d is the molecular volume. In the case of the 2D ideal gas on the surface, the molecular volume is the area per molecule, $L^2 = 1/n_{2\mathrm{D}}$, $n_{2\mathrm{D}}$ is the surface density. The partition function $q^\dagger$ in Eq. 6.24 is then defined as,

$$q^\dagger = \frac{1}{n^\dagger_{2\mathrm{D}} L^2_{\mathrm{th}}}. \tag{A.7}$$

Here we have followed the suggestion by Campbell [111] for the definition of the standard-state value, $n^\dagger_{2\mathrm{D}}$, of the surface density as,

$$n^\dagger_{2\mathrm{D}} = e^{1/3}\left(\frac{p^\dagger}{k_B T}\right)^{2/3} \tag{A.8}$$

where $p^\dagger$ = 1 bar is the standard-state pressure. This definition is dictated by the entropy of the 2D ideal gas being two thirds of the 3D ideal gas.

In the case of the 3D ideal gas, the molecular volume, L^3, is determined by the pressure from equation of state as,

$$L^3 = \frac{k_B T}{p} \tag{A.9}$$

where p is the pressure. The standard-state value, $q^\dagger_T$, of q_T is then determined by the standard-state value of 1 bar for the pressure.

The rotational partition function for a 2D rotor can be obtained directly from the partition function in Eq.(A.5) by replacing L and M with $\frac{2\pi}{\sigma}$ and the moment-of-inertia I, respectively, as,

$$q_R = \frac{1}{\sigma}\left(\frac{2k_B T}{\hbar^2}\right)^{1/2}\sqrt{\pi I}. \tag{A.10}$$

Here σ gives the number of symmetry operations of the molecule that correspond to proper rotations. The corresponding results for the linear 3D rotor and the non-linear 3D rotor cannot be obtained from the results for the translational partition function and are given by,

$$q_R = \frac{1}{\sigma} \begin{cases} \frac{2k_B T}{\hbar^2} I, & \text{3D linear rotor} \\ \left(\frac{2k_B T}{\hbar^2}\right)^{3/2} \pi \sqrt{I_1 I_2 I_3}, & \text{3D non} - \text{linear rotor} \end{cases} \tag{A.11}$$

Here, I_1, I_2 and I_3 are the principal moments of inertia of the 3D rotor and I is the moment-of-inertia for the 3D linear rotor.

The results in Tables 6.4 and 6.5 were obtained using Eqns.(A.10) and (A.11) where the moments-of-inertia were calculated using the ASE package [94] from the calculated equilibrium structures of the molecule. In the case of the adsorbed molecules, they were treated as 2D rotors, where now I corresponds to the moment-of-inertia around an axis perpendicular to the surface.

Bibliography

1. Prutton, M. *Introduction to Surface Physics* (Clarendon Press, 1994).
2. Binnig, G. & Rohrer, H. Scanning tunneling microscopy. *Surface Science* **126,** 236 –244 (1983).
3. Li, B., Li, Z., Yang, J. & Hou, J. G. STM studies of single molecules: molecular orbital aspects. *Chem. Commun.* **47,** 2747–2762 (2011).
4. Binnig, G., Rohrer, H., Gerber, C. & Weibel, E. 7 7 Reconstruction on Si(111) Resolved in Real Space. *Phys. Rev. Lett.* **50,** 120–123 (1983).
5. Chang, C. C. Auger electron spectroscopy. *Surface Science* **25,** 53 –79 (1971).
6. Riviére, J. C. Auger electron spectroscopy. *Contemporary Physics* **14,** 513–539 (1973).
7. Arnolds, H. & Bonn, M. Ultrafast surface vibrational dynamics. *Surface Science Reports* **65,** 45 –66 (2010).
8. Buckingham, J. D. Thermionic emission properties of a lanthanum hexaboride/rhenium cathode. *British Journal of Applied Physics* **16,** 1821 (1965).
9. Liang, S.-J. & Ang, L. K. Electron Thermionic Emission from Graphene and a Thermionic Energy Converter. *Phys. Rev. Applied* **3,** 014002 (2015).
10. Diez, S. J. *et al.* Crystallization at Solvent Interfaces Enables Access to a Variety of Cocrystal Polymorphs and Hydrates. *Crystal Growth & Design* **18,** 3263–3268 (2018).
11. Lusi, M. Engineering Crystal Properties through Solid Solutions. *Crystal Growth & Design* **18,** 3704–3712 (2018).
12. Deimel, P. S. *et al.* Direct quantitative identification of the "surface trans-effect". *Chem. Sci.* **7,** 5647–5656 (2016).
13. Liu, W., Tkatchenko, A. & Scheffler, M. Modeling Adsorption and Reactions of Organic Molecules at Metal Surfaces. *Accounts of Chemical Research* **47.** PMID: 24915492, 3369–3377 (2014).

14. Bowker, M. Introduction to surface chemistry and catalysis. By Gabor A. Somorjai, Wiley, Chichester, UK 1994, XXIV, 667 pp., hardcover, Â£24.95, ISBN 0-471-03192-5. *Chemical Vapor Deposition* **1,** 90–90 (1995).

15. Tung, R. T. Electron transport at metal-semiconductor interfaces: General theory. *Phys. Rev. B* **45,** 13509–13523 (1992).

16. YAMAMOTO, N. & YAMAMOTO, M. in *Control of Semiconductor Interfaces* (eds Ohdomari, I., Oshima, M. & Hiraki, A.) 561 –566 (Elsevier, Amsterdam, 1994).

17. Nishi, Y. in *Control of Semiconductor Interfaces* (eds Ohdomari, I., Oshima, M. & Hiraki, A.) 9 –12 (Elsevier, Amsterdam, 1994).

18. Tanaka, T. & Osuka, A. Conjugated porphyrin arrays: synthesis, properties and applications for functional materials. *Chem. Soc. Rev.* **44,** 943–969 (2015).

19. Auwarter, W., Ecija, D., Klappenberger, F. & Barth, J. V. Porphyrins at interfaces. *Nat Chem* **7.** Review, 105–120 (2015).

20. Moore, M. R. in, 1–28 (Springer New York, New York, NY, 2009).

21. Karpuschkin, T., Kappes, M. M. & Hampe, O. Binding of O2 and CO to Metal Porphyrin Anions in the Gas Phase. *Angewandte Chemie International Edition* **52,** 10374–10377 (2013).

22. Royer, S. & Duprez, D. Catalytic Oxidation of Carbon Monoxide over Transition Metal Oxides. *ChemCatChem* **3,** 24–65 (Dec. 2010).

23. Vendelbo, S. B. *et al.* Self Blocking of CO Dissociation on a Stepped Ruthenium Surface. *Topics in Catalysis* **53,** 357–364 (2010).

24. Solladié, N., Rein, R. & Walther, M. *Light harvesting porphyrin-crown ether conjugates: Toward artificial photosynthetic systems* (May 2007).

25. Blyholder, G. Molecular Orbital View of Chemisorbed Carbon Monoxide. *The Journal of Physical Chemistry* **68,** 2772–2777 (1964).

26. Föhlisch, A. *et al.* The bonding of CO to metal surfaces. *The Journal of Chemical Physics* **112,** 1946–1958 (2000).

27. Slater, J. C. & Krutter, H. M. The Thomas-Fermi Method for Metals. *Phys. Rev.* **47,** 559–568 (1935).

28. Hohenberg, P. & Kohn, W. Inhomogeneous Electron Gas. *Phys. Rev.* **136,** B864–B871 (1964).

29. Honkala, J. *et al.* Ammonia synthesis from first principles calculations. *Science* **307,** 555–558 (2005).

30. Schweinfest, R., Paxton, A. T. & Finnis, M. W. Bismuth embrittlement of copper is an atomic size effect. *Nature* **432,** 1008 EP – (2004).

31. Donovan, P., Robin, A., Dyer, M. S., Persson, M. & Raval, R. Unexpected Deformations Induced by Surface Interaction and Chiral Self-Assembly of CoII-Tetraphenylporphyrin (Co-TPP) Adsorbed on Cu(110): A Combined STM and Periodic DFT Study. *Chemistry â A European Journal* **16,** 11641–11652 (2010).

32. Floris, A. *et al.* Driving Forces for Covalent Assembly of Porphyrins by Selective CâH Bond Activation and Intermolecular Coupling on a Copper Surface. *Journal of the American Chemical Society* **138.** PMID: 27097295, 5837–5847 (2016).

33. Herper, H. C. *et al.* Iron porphyrin molecules on Cu(001): Influence of adlayers and ligands on the magnetic properties. *Phys. Rev. B* **87,** 174425 (2013).

34. Knaak, T. *et al.* Surface cis Effect: Influence of an Axial Ligand on Molecular Self-Assembly. *Journal of the American Chemical Society* **138.** PMID: 27233351, 7544–7550 (2016).

35. Browne, W. R. & Feringa, B. L. Making molecular machines work. *Nature Publishing Group* **1.** Review Article, 25 EP – (2006).

36. Changtong, C. *et al.* A porphyrin molecule that generates, traps, stores, and releases singlet oxygen. *Journal of Photochemistry and Photobiology A: Chemistry* **260,** 9 –13 (2013).

37. Paul, S., Amalraj, F. & Radhakrishnan, S. CO sensor based on polypyrrole functionalized with iron porphyrin. *Synthetic Metals* **159,** 1019 –1023 (2009).

38. Seol, M.-L., Choi, S.-J., Kim, C.-H., Moon, D.-I. & Choi, Y.-K. Porphyrin − Silicon Hybrid Field-Effect Transistor with Individually Addressable Top-gate Structure. *ACS Nano* **6.** PMID: 22148941, 183–189 (2012).

39. Yu, J., Mathew, S., Flavel, B. S., Johnston, M. R. & Shapter, J. G. Ruthenium Porphyrin Functionalized Single-Walled Carbon Nanotube ArraysâA Step Toward Light Harvesting Antenna and Multibit Information Storage. *Journal of the American Chemical Society* **130.** PMID: 18597433, 8788–8796 (2008).

40. Hess, C., Bonn, M., Funk, S. & Wolf, M. Hot-band excitation of CO chemisorbed on Ru(001) studied with broadband-IR sum-frequency generation. *Chemical Physics Letters* **325,** 139 –145 (2000).

41. Sedghi, G. *et al.* Long-range electron tunnelling in oligo-porphyrin molecular wires. *Nat Nano* **6,** 517–523 (2011).

42. Kumar, S., Choudhuri, I. & Pathak, B. An atomically thin ferromagnetic half-metallic pyrazine-fused Mn-porphyrin sheet: a slow spin relaxation system. *J. Mater. Chem. C* **4,** 9069–9077 (2016).

43. Mondal, S. Recent advancement of Ullmann-type coupling reactions in the formation of C–C bond. *ChemTexts* **2,** 17 (2016).

44. Ma, D., Cai, Q. & Zhang, H. Mild Method for Ullmann Coupling Reaction of Amines and Aryl Halides. *Organic Letters* **5.** PMID: 12841753, 2453–2455 (2003).

45. Hofer, W. A., Foster, A. S. & Shluger, A. L. Theories of scanning probe microscopes at the atomic scale. *Rev. Mod. Phys.* **75,** 1287–1331 (2003).

46. Zangwill, A. *Physics at Surfaces* (Cambridge University Press, 1988).

47. Chiang, S. Scanning Tunneling Microscopy Imaging of Small Adsorbed Molecules on Metal Surfaces in an Ultrahigh Vacuum Environment. *Chemical Reviews* **97.** PMID: 11851442, 1083–1096 (1997).

48. Tersoff, J. & Hamann, D. R. Theory of the scanning tunneling microscope. *Phys. Rev. B* **31,** 805–813 (1985).

49. Bardeen, J. Tunnelling from a Many-Particle Point of View. *Phys. Rev. Lett.* **6,** 57–59 (1961).

50. Krim, L., Sorgues, S., Soep, B. & Shafizadeh, N. Infrared Spectra of RuTPP, Ru-COTPP, and Ru(CO)2TPP Isolated in Solid Argon. *The Journal of Physical Chemistry A* **109.** PMID: 16834214, 8268–8274 (2005).

51. Kreuzer, L. B. Ultralow Gas Concentration Infrared Absorption Spectroscopy. *Journal of Applied Physics* **42,** 2934–2943 (1971).

52. O'Connor, R. T., DuPré, E. F. & Mitcham, D. Applications of Infrared Absorption Spectroscopy to Investigations of Cotton and Modified Cottons: Part I: Physical and Crystalline Modifications and Oxidation. *Textile Research Journal* **28,** 382–392 (1958).

53. Fowles, G. *Introduction to Modern Optics* (Dover Publications, 1989).

54. Hecht, E. *Optics* (Addison-Wesley, 2002).

55. Zhu, X. D., Suhr, H. & Shen, Y. R. Surface vibrational spectroscopy by infrared-visible sum frequency generation. *Phys. Rev. B* **35,** 3047–3050 (1987).

56. Zhang, V. L., Arnolds, H. & King, D. A. Hot band excitation of CO/Ir111 studied by broadband sum frequency generation. *Surface Science* **587.** Proceedings of the 11th International Conference on Vibrations at Surfaces, 102 –109 (2005).

57. Tegeder, P. Optically and thermally induced molecular switching processes at metal surfaces. *Journal of Physics: Condensed Matter* **24,** 394001 (2012).

58. Griffiths, D. *Introduction to Quantum Mechanics* (Pearson Prentice Hall, 2005).

59. Martin, R. *Electronic Structure: Basic Theory and Practical Methods* (Cambridge University Press, 2004).

60. Kohanoff, J. *Electronic Structure Calculations for Solids and Molecules: Theory and Computational Methods* (Cambridge University Press, 2006).

61. Koch, W & C. A. Holthausen, M. *A Chemist Guide to Density Functional Theory* (Jan. 2001).

62. Teller, E. On the Stability of Molecules in the Thomas-Fermi Theory. *Rev. Mod. Phys.* **34,** 627–631 (1962).

63. Kohn, W. & Sham, L. J. Self-Consistent Equations Including Exchange and Correlation Effects. *Phys. Rev.* **140,** A1133–A1138 (1965).

64. Filippi, C., Healy, S. B., Kratzer, P., Pehlke, E. & Scheffler, M. Quantum Monte Carlo Calculations of H_2 Dissociation on Si(001). *Phys. Rev. Lett.* **89,** 166102 (2002).

65. Austin, B. M., Zubarev, D. Y. & Lester, W. A. Quantum Monte Carlo and Related Approaches. *Chemical Reviews* **112.** PMID: 22196085, 263–288 (2012).

66. Perdew, J. P., Burke, K. & Ernzerhof, M. Generalized Gradient Approximation Made Simple. *Phys. Rev. Lett.* **77,** 3865–3868 (1996).

67. Perdew, J. P. *et al.* Atoms, molecules, solids, and surfaces: Applications of the generalized gradient approximation for exchange and correlation. *Phys. Rev. B* **46,** 6671–6687 (1992).

68. Becke, A. D. Density-functional exchange-energy approximation with correct asymptotic behavior. *Phys. Rev. A* **38,** 3098–3100 (1988).

69. Klime š, J. c. v., Bowler, D. R. & Michaelides, A. Van der Waals density functionals applied to solids. *Phys. Rev. B* **83,** 195131 (2011).

70. Ashcroft, N. & Mermin, N. *Solid State Physics* (Cengage Learning, 2011).

71. Gonzalez, E., Brothers, P. J. & Ghosh, A. Density Functional Theory Calculations on Ruthenium(IV) Bis(amido) Porphyrins: Search for a Broader Perspective of Heme Protein Compound II Intermediates. *The Journal of Physical Chemistry B* **114.** PMID: 20979402, 15380–15388 (2010).

72. Mochida, I. *et al.* A kinetic study on reduction of nitric oxide over cobalt tetraphenylporphyrin supported on titanium dioxide. *Journal of Catalysis* **77,** 519 –526 (1982).

73. Rezaeifard, A. & Jafarpour, M. The catalytic efficiency of Fe-porphyrins supported on multi-walled carbon nanotubes in the heterogeneous oxidation of hydrocarbons and sulfides in water. *Catal. Sci. Technol.* **4,** 1960–1969 (2014).

74. Wiengarten, A. *et al.* Surface-assisted Dehydrogenative Homocoupling of Porphine Molecules. *Journal of the American Chemical Society* **136.** PMID: 24955656, 9346–9354 (2014).

75. Moresco, F. *et al.* Conformational Changes of Single Molecules Induced by Scanning Tunneling Microscopy Manipulation: A Route to Molecular Switching. *Phys. Rev. Lett.* **86,** 672–675 (2001).

76. Winkelmann, C. B. *et al.* Optical Switching of Porphyrin-Coated Silicon Nanowire Field Effect Transistors. *Nano Letters* **7.** PMID: 17497816, 1454–1458 (2007).

77. Iancu, V., Deshpande, A. & Hla, S.-W. Manipulating Kondo Temperature via Single Molecule Switching. *Nano Letters* **6.** PMID: 16608290, 820–823 (2006).

78. Wang, C. *et al.* Coordination reaction between tetraphenylporphyrin and nickel on a TiO2(110) surface. *Chem. Commun.* **50,** 8291–8294 (61 2014).

79. Christiansen, M., Thomsen, E. & Onsgaard, J. Coadsorption of K and CO on Cu(110). *Surface Science* **261,** 179 –190 (1992).

80. Hammer, B., Morikawa, Y. & Nørskov, J. K. CO Chemisorption at Metal Surfaces and Overlayers. *Phys. Rev. Lett.* **76,** 2141–2144 (1996).

81. Kresse, G. & Furthmüller, J. Efficiency of ab-initio total energy calculations for metals and semiconductors using a plane-wave basis set. *Computational Materials Science* **6,** 15 –50 (1996).

82. Kresse, G. & Furthmüller, J. Efficient iterative schemes for ab initio total-energy calculations using a plane-wave basis set. *Phys. Rev. B* **54,** 11169–11186 (1996).

83. Kresse, G, Hafner, J & Needs, R. J. Optimized norm-conserving pseudopotentials. *Journal of Physics: Condensed Matter* **4,** 7451 (1992).

84. Kresse, G. & Joubert, D. From ultrasoft pseudopotentials to the projector augmented-wave method. *Phys. Rev. B* **59,** 1758–1775 (1999).

85. Loffreda, D., Jugnet, Y., Delbecq, F., Bertolini, J. C. & Sautet, P. Coverage Dependent Adsorption of Acrolein on Pt(111) from a Combination of First Principle Theory and HREELS Study. *The Journal of Physical Chemistry B* **108,** 9085–9093 (2004).

86. omiya, T. *Energy Conversion between CO and Porphyrins on Surfaces Studied by Ultrafast Vibrational and Scanning Tunneling Spectroscopies* PhD thesis (University of Liverpool, 2005).

87. Liao, M.-S. & Scheiner, S. Electronic structure and bonding in metal porphyrins, metal=Fe, Co, Ni, Cu, Zn. *The Journal of Chemical Physics* **117,** 205–219 (2002).

88. Liao, M.-S. & Scheiner, S. Relativistic effects in iron-, ruthenium-, and osmium porphyrins. *Chemical Physics* **285,** 195 –206 (2002).

89. Zuo, Z., Huang, W., Han, P. & Li, Z. Adsorption of CO on Cu (110) and (100) surfaces using COSMO-based DFT. *Journal of Molecular Modeling* **15,** 1079–1083 (2009).

90. Omiya, T. *et al.* Desorption of CO from individual ruthenium porphyrin molecules on a copper surface via an inelastic tunnelling process. *Chem. Commun.* **53,** 6148–6151 (2017).

91. Morse, P. M. Diatomic Molecules According to the Wave Mechanics. II. Vibrational Levels. *Phys. Rev.* **34,** 57–64 (1929).

92. Woodruff, D., Hayden, B., Prince, K. & Bradshaw, A. Dipole coupling and chemical shifts in IRAS of CO adsorbed on Cu(110). *Surface Science* **123,** 397 –412 (1982).

93. Dabo, I. Resilience of gas-phase anharmonicity in the vibrational response of adsorbed carbon monoxide and breakdown under electrical conditions. *Phys. Rev. B* **86,** 035139 (2012).

94. Hammer, B., Hansen, L. B. & Nørskov, J. K. Improved adsorption energetics within density-functional theory using revised Perdew-Burke-Ernzerhof functionals. *Phys. Rev. B* **59,** 7413–7421 (1999).

95. Oliphant, T. E. Python for Scientific Computing. *Computing in Science Engineering* **9,** 10–20 (2007).

96. Larsen, A. H. *et al.* The atomic simulation environmentâa Python library for working with atoms. *Journal of Physics: Condensed Matter* **29,** 273002 (2017).

97. Dahl, J. P. & Springborg, M. The Morse oscillator in position space, momentum space, and phase space. *The Journal of Chemical Physics* **88,** 4535–4547 (1988).

98. Weast, R. C., Lide, . David R. & of Rhode Island. Coastal Resources Center, U. *CRC handbook of chemistry and physics* English. Periodical; Periodical/Journal, magazine, other. "A ready-reference book of chemical and physical data.". 1978.

99. Fukuda, T. *et al.* Dissociation of carbon dioxide and creation of carbon particles and films at room temperature. *New Journal of Physics* **9,** 321 (2007).

100. Grass, M *et al.* Unoccupied electronic states and surface barriers at Cu surfaces. *Journal of Physics: Condensed Matter* **5,** 599 (1993).

101. Azizyan, A. S., Kurtikyan, T. S., Martirosyan, G. G. & Ford, P. C. Tracking Reactive Intermediates by FTIR Monitoring of Reactions in Low-Temperature Sublimed Solids: Nitric Oxide Disproportionation Mediated by Ruthenium(II) Carbonyl Porphyrin Ru(TPP)(CO). *Inorganic Chemistry* **52.** PMID: 23573997, 5201–5205 (2013).

102. Grill, L. *et al.* Nano-architectures by covalent assembly of molecular building blocks. *Nature nanotechnology* **2,** 687–91 (Nov. 2007).

103. Hanke, F., Haq, S., Raval, R. & Persson, M. Heat-to-Connect: Surface Commensurability Directs Organometallic One-Dimensional Self-Assembly. *ACS Nano* **5.** PMID: 22003852, 9093–9103 (2011).

104. Haq, S. *et al.* Clean Coupling of Unfunctionalized Porphyrins at Surfaces To Give Highly Oriented Organometallic Oligomers. *Journal of the American Chemical Society* **133.** PMID: 21707113, 12031–12039 (2011).

105. In't Veld, M., Iavicoli, P., Haq, S., Amabilino, D. B. & Raval, R. Unique intermolecular reaction of simple porphyrins at a metal surface gives covalent nanostructures. *Chem. Commun.* 1536–1538 (2008).

106. Kresse, G. & Hafner, J. Ab initio. *Phys. Rev. B* **47,** 558–561 (1993).

107. Dion, M., Rydberg, H., Schröder, E., Langreth, D. C. & Lundqvist, B. I. Van der Waals Density Functional for General Geometries. *Phys. Rev. Lett.* **92,** 246401 (2004).

108. Atkins, P. & de Paula, J. *Atkins' Physical Chemistry* (OUP Oxford, 2010).

109. Björk, J. *et al.* Adsorption of Aromatic and Anti-Aromatic Systems on Graphene through $\pi\pi$ Stacking. *The Journal of Physical Chemistry Letters* **1,** 3407–3412 (2010).

110. Lucci, F. R. *et al.* Controlling Hydrogen Activation, Spillover, and Desorption with PdâAu Single-Atom Alloys. *The Journal of Physical Chemistry Letters* **7.** PMID: 26747698, 480–485 (2016).

111. Campbell, C. T., Sprowl, L. H. & Árnadóttir, L. Reply to Comment on Equilibrium Constants and Rate Constants for Adsorbates: Two-Dimensional (2D) Ideal Gas, 2D Ideal Lattice Gas, and Ideal Hindered Translator Models. *The Journal of Physical Chemistry C* **120,** 20481–20482 (2016).

112. Eyring, H. The Activated Complex in Chemical Reactions. *The Journal of Chemical Physics* **3,** 107–115 (1935).

113. Björk, J., Stafström, S. & Hanke, F. Zipping Up: Cooperativity Drives the Synthesis of Graphene Nanoribbons. *Journal of the American Chemical Society* **133.** PMID: 21859135, 14884–14887 (2011).